Abstract

FALLEST, DAVID WILLIAM. Kinetic Nucleation Theory and Thermal Fluctuations in the Formation of Cosmic Dust. (Under the direction of Davide Lazzati.)

Large amounts of dust ($\sim 10^8$ $M_\odot$) have been observed in quasi-stellar objects at high-redshift ($z > 5$), but the origin of such dust is still a mystery. Most dust formation models rely on classical nucleation theory which treats nucleation in conditions of thermodynamic equilibrium. A theory of nucleation based on the kinetic theory is developed here incorporating non-local thermodynamic equilibrium and taking size dependent grain properties into account. The kinetic theory of nucleation, while computationally more expensive than classical nucleation theory, provides an improved methodology for determining nucleation rates of dust grains, and is well suited for predicting dust yields from astronomical sources. In this improved theory, size dependent grain properties, such as grain shape and binding energy, rather than bulk material properties as in classical nucleation theory, are used whenever possible. Additionally, Monte Carlo methods are employed to evolve the size of the grain and to determine its temperature fluctuations due to collisional heating from monomer attachment and carrier gas interactions. The evaporation rate of a grain depends sensitively on its temperature, an effect not considered in classical nucleation theory. An average detachment rate is calculated for each initial grain size, and attachment and detachment rates as a function of grain size are found. Nucleation rates are calculated from the attachment and average detachment rates. Grain sizes and temperatures as a function of time are presented for two sample materials: water and carbon. Nucleation rates for water droplets are found for saturation levels in the range from 6 to 30 and compared to expansion cloud chamber experiment results. Dust mass yields of carbonaceous grains are calculated and compared with previous dust mass predictions for a 20 $M_\odot$ progenitor core-collapse supernova.

Kinetic Nucleation Theory and Thermal Fluctuations in the Formation of Cosmic Dust

by
David William Fallest

A dissertation submitted to the Graduate Faculty of
North Carolina State University
in partial fulfillment of the
requirements for the Degree of
Doctor of Philosophy

Physics

Raleigh, North Carolina

2012

APPROVED BY:

Stephen Reynolds	Lubos Mitas
Tarek Echekki	Davide Lazzati Chair of Advisory Committee

Dedication

To my family and friends, in Illinois, Wisconsin, North Carolina, or wherever you are, for your continued support throughout the whole graduate school process.

And to my dad, I wish you could have been here to see me finish.

Biography

David Fallest was born in Chicago, IL, in 1974 and grew up in Des Plaines, IL. While being considered an intelligent child, David did not enjoy attending school. After graduating from Elk Grove High School in 1992, David spent some time at the University of Illinois at Chicago studying architecture. However, still disillusioned with the educational system, in 1994 he left UIC to pursue life in the "real world" instead. At the time, David was given a choice by his father: go back to school or start paying rent. In order to avoid paying rent, David chose to continue his education, but only taking those classes that interested him, mainly, math and science. This was probably the best decision he ever made.

Throughout the next seven years David slowly worked his way through his associate's degree at William Rainey Harper College. During this time David also worked as an apprentice and journeyman electrician with I.B.E.W. Local 134 in Chicago, IL, and noodled around as a juggler and variety performer. In 2002, David graduated from Harper College, and enrolled at Beloit College in Beloit, WI. In 2006, David graduated from Beloit College with majors in Physics and Russian, and a minor in Russian Studies, and began his graduate studies in Physics at North Carolina State University.

Acknowledgements

Special thanks to Dr. Davide Lazzati for his guidance, wisdom, and never-ending patience.

Thanks also go to Dr. Takaya Nozawa and Dr. Ken'ichi Nomoto for allowing me to conduct part of this research at the Institute for the Physics and Mathematics of the Universe in Kashiwa, Japan.

Finally, I would like to thank Drs. Umeda and Nomoto for allowing me to use their hydrodynamic results for this work.

Table of Contents

List of Tables

List of Figures

List of Symbols

Symbol	Meaning
A	kinetic prefactor of steady nucleation rate
A'	kinetic prefactor of steady nucleation rate
B_n	sublimation energy of n-sized cluster
b	energy quanta necessary to free a monomer from the cluster
$C(n)$	distribution of n-sized clusters
C_{exp}	expansion-cloud chamber droplet concentration
$C_f(m)$	number of ways m quanta can be distributed among f degrees of freedom
C_n	concentration of n-sized clusters
C_0	concentration of nucleation sites
C_1	concentration of monomers
$C_{1,e}$	monomer concentration at the phase-equilibrium pressure
C_{24}	Carbon cluster with $n = 24$
$\tilde{C}_1$	nominal concentration of monomers
c	shape factor
E_n	binding energy of n-sized cluster
f	degrees of freedom
f_n	monomer attachment rate to n-sized cluster
$f_{n,Ar}$	collision rate of argon carrier gas atoms with an n-sized cluster
f_1	attachment rate of monomers onto a monomer cluster
f^*	attachment rate of monomers on to the critical cluster
i	energy quanta contained in a vibrational degree of freedom
G	Gibbs free energy
G_{ref}	reference energy
G_1	Gibbs free energy in old phase
G_2	Gibbs free energy in new phase
G_{ex}	excess Gibbs free energy
g_n	monomer detachment rate from n-sized cluster
$g_{n,unmod}$	unmodified detachment rate
g_n^*	detachment rate including cluster temperatures and rate corrections for small grains

Symbol	Meaning
$\tilde{g_n}$	detachment rate accounting for cluster temperature
$\hbar$	Planck's constant divided by 2π
J	nucleation rate
J_{BD}	Becker & Döring nucleation rate
J_{CL}	nucleation rate found using classical nucleation theory
J_{exp}	expansion-cloud chamber nucleation rate
J_{MD}	nucleation rate found using molecular dynamics methods
J_s	steady nucleation rate
$\tilde{J}$	nucleation rate from the self-consistent model of Girshick and Chiu (1990)
K_{cg}	kinetic energy of a carrier gas monomer
$K_{cg,f}$	final carrier gas monomer kinetic energy
$K_{cg,i}$	initial carrier gas monomer kinetic energy
K_{in}	kinetic energy of impinging monomer
K_{out}	kinetic energy of ejected monomer
k	Boltzmann constant
keV	kiloelectron volt
M	number of particles in the system
$\mathrm{M}_\odot$	solar mass
M_r	enclosed mass
m	energy quanta available in the cluster
m_{Ar}	mass of argon atom
m_0	monomer mass
N	number of particles in the phase
n	number of monomers in the cluster
n_d	number density
n^*	number of monomer in critical cluster
P_{cr}	critical pressure
P'	reduced pressure
P'_e	reduced phase equilibrium pressure
p	vapor pressure
p_{Ar}	argon carrier gas pressure
p_e	phase equilibrium pressure

Symbol	Meaning
$p_f(b)$	probability a degree of freedom contains at least b energy quanta
p_0	standard pressure of 1 bar
R_{class}	critical cluster radius found through classical nucleation theory
R_V	ratio of total to selective extinction
r	cluster radius
r_{eff}	cluster effective radius
r^*	radius of critical cluster
S	supersaturation
S_n	rate correction for small grains
S	entropy
T	temperature
T_{after}	cluster temperature after monomer detachment
T_{before}	cluster temperature before monomer detachment
$T_{cluster}$	cluster temperature
T_{cr}	critical temperature
T_{Debye}	Debye temperature
T_{gas}	vapor temperature
T_s	average temperature of water and carrier gas molecules
T_w	average temperature of water molecules
T'	reduced temperature
t	time of cluster volume measurement
t_e	equilibrium time
t_n	time after explosion
t_0	initial time after explosion
t'	time of cluster formation
U	internal energy
U_n	internal energy of n-sized cluster
$U_{n,f}$	final cluster internal energy
$U_{n,i}$	initial cluster internal energy
U_1	internal energy of monomer
V	volume
V_{cr}	critical volume

Symbol	Meaning
V_{shell}	volume of expanding mass shell
V^*	volume of the critical cluster
V'	reduced volume
v_0	monomer volume
v^*	volume of the critical cluster
$W(n)$	work to form n-sized cluster
W_1	work to form monomer cluster
W^*	work to form critical cluster
X_n	n-sized cluster of nucleating material
X_1	monomer of nucleating material
Y_1	ratio of the monomer concentration to the nominal monomer concentration
Z	metallicity
z	redshift
z_Z	Zeldovich factor
γ	sticking coefficient
γ_f	mean energy quanta per degree of freedom
γ^*	size dependent sticking coefficient
ΔG	change in the Gibbs free energy
ΔG^*	change in Gibbs free energy to form critical cluster
$\Delta\tilde{G}$	work of cluster formation from the self-consistent model of Girshick and Chiu (1990)
$\Delta\tilde{G}^*$	work of critical cluster formation from the self-consistent model of Girshick and Chiu (1990)
ΔK_{cg}	change in kinetic energy of carrier gas monomer
Δt_{exp}	expansion-cloud chamber nucleation time
$\Delta V_{grains,n}$	total change in volume of grains
$\Delta\mu$	change in chemical potential
λ	wavelength
λ_{sub}	bulk sublimation energy
μ	chemical potential
μ_{coex}	chemical potential when vapor and liquid can coexist
μ_{new}	chemical potential of new phase

Symbol	Meaning
μ_{old}	chemical potential of old phase
ρ_i	liquid density when vapor and liquid can coexist
ρ_l	liquid density
Σ	surface area
σ	surface energy/tension
$\Phi(n)$	effective excessive energy of n-sized cluster
ω	water vapor fraction
ω_0	common frequency of cluster harmonic oscillators

List of Abbreviations

Abbreviation	Meaning
AGB	asymptotic giant branch
AGNs	active galactic nuclei
B3LYP	Becke, three-parameter, Lee-Yang-Parr
CAMS	constant angle Mie scattering
Cas A	Cassiopeia A
CCSN	core-collapse supernova
CCSNe	core-collapse supernovae
CNT	classical nucleation theory
DFT	density functional theory
DMC	diffusion Monte Carlo
EAPSI	East Asia and Pacific Summer Institute
He-Ne	Helium-Neon
IPMU	Institute for the Physics and Mathematics of the Universe
ISM	interstellar medium
KNT	kinetic nucleation theory
MC	Monte Carlo
MD	molecular dynamics
MEXT	Ministry of Education, Culture, Sports, Science and Technology in Japan
MKNT	mean-field kinetic nucleation theory
NSF	National Science Foundation
REBO	reactive empirical bond-order
RRK	Rice-Ramsberger-Kassel
SN	supernova
SNe	supernovae
SNR	supernova remnant
SNRs	supernova remnants
UV	ultraviolet

Chapter 1

Introduction

Attitudes towards dust in the cosmos have gone through dramatic changes over the past hundred years. In the first half of the twentieth century, dust was considered to be little more than a nuisance to observations, but by the end of the century it was known to be vitally important to galactic evolution. Currently, cosmic dust is one of the most interesting areas of study in astrophysics. While dust is ubiquitous in the Universe it is still poorly understood. Among the various riddles surrounding cosmic dust are the mechanisms that lead to the formation of dust particles, and the locations where the first grains condensed. This dissertation focuses on improving the theoretical framework describing the dust formation process – nucleation – to include for the first time considerations of cluster microphysical properties and temperature fluctuations. The modified nucleation theory is developed using water droplet formation as a test case, and is then applied to the formation of carbonaceous dust grains in the expanding ejecta of a core-collapse supernova.

1.1 Motivation

Large amounts ($\sim 10^8$ $M_\odot$) of dust have been inferred from observations of high-redshift ($z > 5$) quasars (Bertoldi et al., 2003; Priddey et al., 2003; Beelen et al., 2006; Dwek et al., 2007; Wang et al., 2008). Asymptotic giant branch (AGB) stars (Morgan and Edmunds, 2003; Zhukovska et al., 2008; Valiante et al., 2009) and core-collapse supernovae (CCSNe) (Kozasa et al., 1989, 1991; Todini and Ferrara, 2001; Nozawa et al., 2003; Bianchi and Schneider, 2007; Kozasa et al., 2009; Cherchneff, 2010) are the two sources

thought to produce the largest amounts of dust and scenarios can be constructed where either of these sources produces the observed dust amounts (Dwek and Cherchneff, 2011). Arguments have been made, however, that since the age of the Universe at that redshift was less than one gigayear, AGB stars have not had sufficient time to evolve off the main sequence and to produce much dust (Dwek, 1998). Therefore, supernovae (SNe) of massive, short-lived Population III stars would be the most likely source of the dust (Bromm et al., 2002; Morgan and Edmunds, 2003; Maiolino et al., 2004; Dwek et al., 2007). Unfortunately, such SNe are not observable with current instrumentation. Therefore, we must rely on theoretical predictions of dust yields from these SNe to determine if they could, indeed, be the dominant source of high-redshift dust.

Dust production predictions must then necessarily be compared against observations of recent SNe, such as SN1987A, and supernova remnants (SNRs), such as Kepler and Cassiopeia A (Cas A). Unfortunately, the accuracy of these predictions is suspect. Discrepancies as large as three orders of magnitude occur between total dust masses predicted theoretically and those inferred from far-infrared and submillimeter observations (see Figure 1.1). This implies that the theory used for making dust formation predictions needs to be reconsidered, and alternatives developed, in order to improve or confirm current dust predictions, and ultimately, to determine the origin of dust at high-redshift.

1.2 Dust in the cosmos

We now know that approximately one percent of the interstellar material in our own Milky Way galaxy consists of dust particles (Bussoletti and Colangeli, 1990). Before the early twentieth century, however, astronomers did not know dust existed. In the late eighteenth century, dark patches observed in the Milky Way (see Figure 1.2) led astronomers to believe that these patches were actually areas devoid of any material (Herschel, 1785). Later, observations indicated that the light from a distant object suffers from extinction, which allowed astronomers to figure out that there must be some sort of intervening material blocking part of the light (Hartmann, 1904). Finally, Trumpler (1930) showed that some of this intervening material consisted of small solid particles – dust. Due to its ability to hamper observations, the fog of dust caused accurate calculations to distant objects to be problematic (Dorschner and Henning, 1995; Li and Greenberg, 2003). It was not until almost sixty-five years later that the other roles dust particles play in

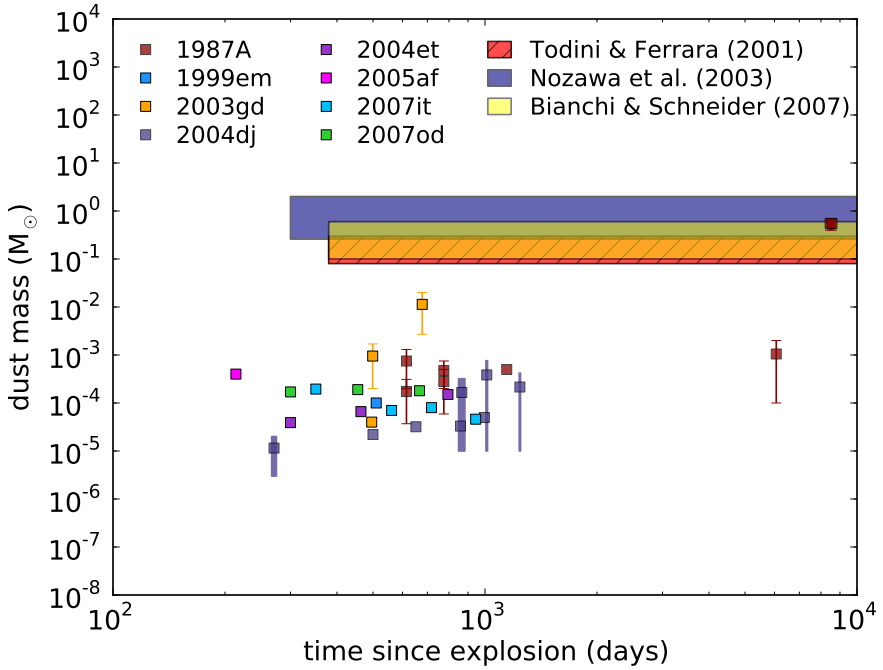

Figure 1.1: Total dust masses inferred from observations of CCSNe (see Gall et al. (2011) and references therein). Filled squares represent inferred total dust masses. Error bars are included for observations that infer a range of total dust mass values and the filled square was placed at the center of the range. Observations that inferred a range of dust mass values over the span of a number of days are shown as filled areas. Also shown are the overlapping ranges of predictions of total dust masses for the models of Todini and Ferrara (2001) for SN1987A with dust formation starting as early as day 380, Nozawa et al. (2003) for 13–40 $M_{\odot}$ progenitor stars with dust forming as early as day 300, and the revised model of SN1987A by Bianchi and Schneider (2007).

the Universe were realized: dust vigorously influences galactic evolution (Dorschner and Henning, 1995) and enriches the metallicities of successive generations of stars (Schneider et al., 2006), is the basis for the formation of rocky planets, is vital to astrochemistry by providing sites for the formation of molecules (Bussoletti and Colangeli, 1990; van Dishoeck et al., 1993; Schneider et al., 2006; Cherchneff and Dwek, 2010), and polarizes starlight (Draine, 2003). Currently, cosmic dust grains are being studied from both observational and theoretical points of view, and dust grain analogs are being studied in laboratory experiments.

Figure 1.2: Milky Way Galaxy (Brunier, 2008). The dark patches running through the middle of the galaxy were once thought to be areas devoid of any material, allowing one to see beyond the galaxy.

Draine (2003) identified nine, and Li and Greenberg (2003) fifteen, problems about cosmic dust that still do not have satisfactory answers. One of the questions raised by Li and Greenberg is "what are the sources and sinks (destruction) of interstellar dust?" Dust sources include molecular clouds, galaxies, active galactic nuclei (AGNs) and quasars (Dwek et al., 2007), colliding wind regions of binary systems including Wolf-Rayet stars (Cherchneff, 2010), mass loss winds of AGB stars (Morgan and Edmunds, 2003; Zhukovska et al., 2008; Valiante et al., 2009), and the ejecta of SNe and SNRs (Kozasa et al., 1989, 1991; Todini and Ferrara, 2001; Nozawa et al., 2003; Bianchi and Schneider, 2007; Kozasa et al., 2009; Cherchneff, 2010; Nozawa et al., 2011). However, how efficient any of these sources are at creating dust is as yet unknown.

1.2.1 Dust at high-redshift

One issue being debated is the source of dust at high-redshift ($z > 5$). As an example, let us consider the case of SDSS J1148 + 5251, a high-redshift quasar ($z = 6.4$) with an estimated dust mass of 2×10^8 $M_\odot$ (Dwek et al., 2007). In order for SNe to account

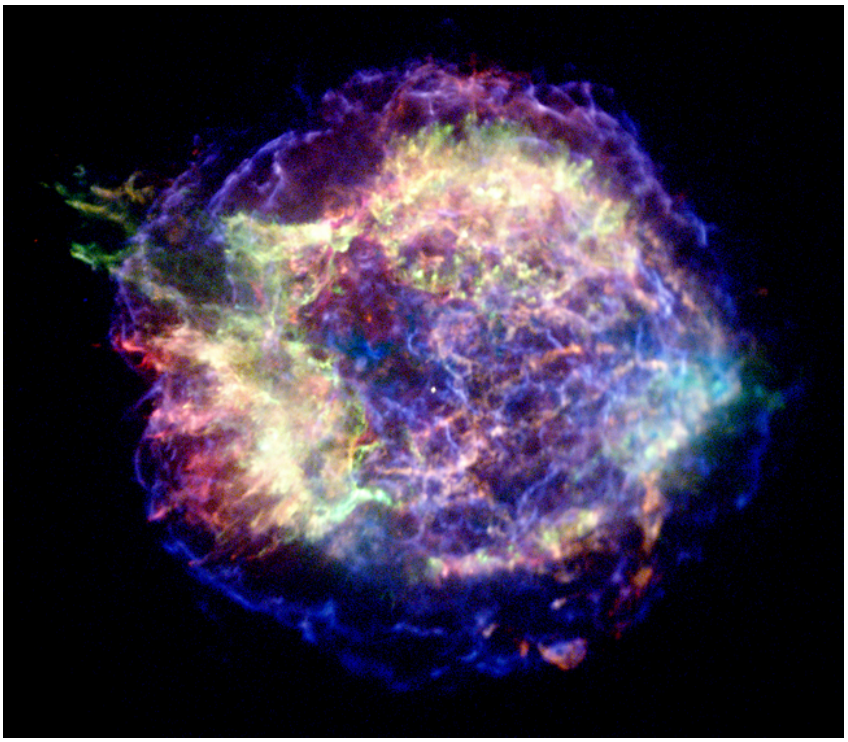

Figure 1.3: Composite x-ray image of SNR Cas A (Stage et al., 2006) taken using NASA's Chandra X-ray Observatory. The red, green and blue colors correspond to 0.5–1.5 keV, 1.5–2.5 keV, and 4.0–6.0 keV X-ray energies, respectively.

for this amount of dust Dwek et al. (2007) show that each SN needs to produce at least 1 $M_\odot$ of dust. The obvious question then being: can a SN produce this much dust?

Since high-redshift SNe are not observable, two of the most popular objects to study have been the Cas A SNR (see Figure 1.3) and SN1987A (Figure 1.4). Dust estimates from infrared observations of Cas A only amount to 0.054 $M_\odot$ using *Spitzer* (Rho et al., 2008), 0.06 $M_\odot$ using *AKARI* (Sibthorpe et al., 2010), and 0.075 $M_\odot$ using *Herschel* (Barlow et al., 2010). Dust masses inferred from infrared observations of SN1987A have been $\sim 10^{-4}$ $M_\odot$ (as a lower limit (Wooden et al., 1993)) and 3×10^{-4} $M_\odot$ (Danziger, 2009). These estimates are much lower than the necessary amount of 1 $M_\odot$ found by Dwek et al. (2007). Dust particles absorb visible light and emit infrared radiation. However, dust at a few tens of Kelvin may not be detected at the mid-infrared wavelengths of many observations. There is, therefore, the possibility that some dust escapes detection because it is too cold. Inhomogeneities, clumps, in the distribution of the dust could also

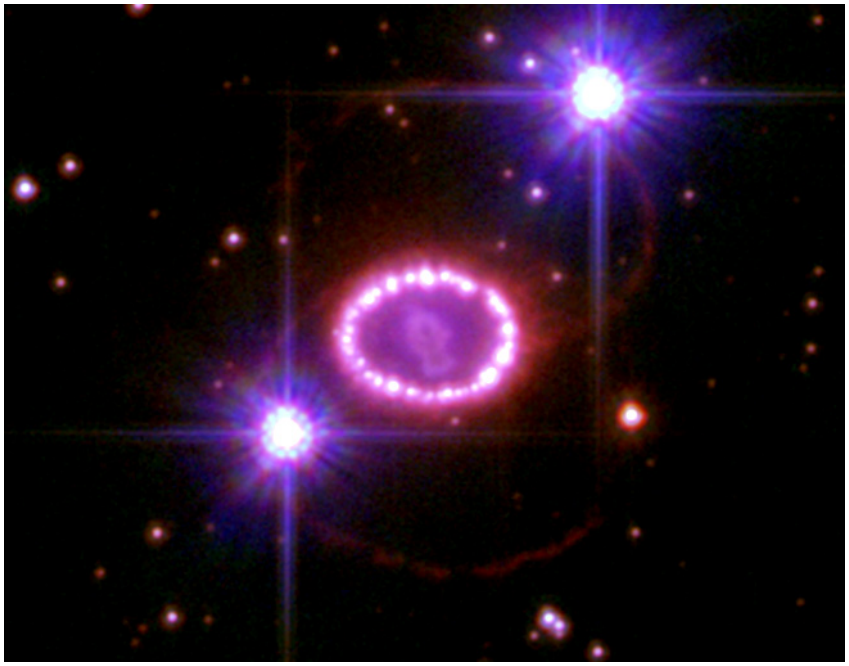

Figure 1.4: Composite image of SN1987A from the Hubble Space Telescope. (NASA et al., 2007)

cause some areas to be optically thick, thereby obscuring some dust detection (Sugerman et al., 2006). More recently, dust estimates, which include colder dust, of 0.4–0.7 $M_\odot$ have been inferred in SN1987A by *Herschel* observations (Matsuura et al., 2011). It is important to note, however, that the highest *Herschel* dust mass estimates require 100% dust condensation from available material (Matsuura et al., 2011), which may not actually be possible.

Detections of cold dust have also been possible in the Kepler and Cas A SNRs. In Kepler, dust mass estimates of 0.2–3 $M_\odot$ have been found (Morgan et al., 2003), and more recently $2.5–3.9 \times 10^{-3}$ $M_\odot$ (Gomez et al., 2012). The estimates of cold dust in Cas A have been as high as 2–4 $M_\odot$ (Dunne et al., 2003), but were refuted by Krause et al. (2004) who said that this dust was actually from a molecular cloud in the line of sight to Cas A. The dust in Cas A was then estimated to be < 0.2 $M_\odot$ (Krause et al., 2004). More recent results by Dunne et al. (2009) estimate the mass of cold dust in Cas A to be ~ 1 $M_\odot$. From observations of SNRs from core-collapse SNe (CCSNe), like Cas A, it seems plausible that SNe could produce the required amount of dust. However, the larger amounts of dust found in Kepler (a Type Ia SN) are likely to be due to swept up

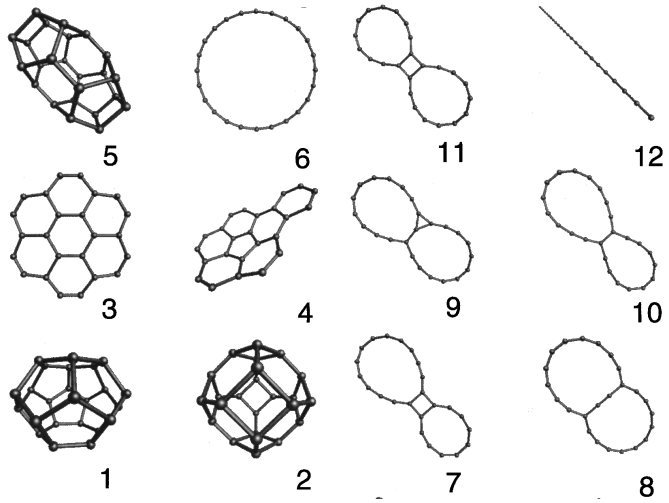

Figure 1.5: Isomers of C_{24} found using density functional theory techniques (Jones, 1999).

interstellar dust (Gomez et al., 2012).

SN1987A is also believed to have been a core-collapse supernova (CCSN). The progenitor of SN1987A was of a blue-supergiant with a mass of 18–20 $M_\odot$ (Matsuura et al., 2011). The progenitor of Cas A remains unknown, but its mass has been constrained to be 15–25 $M_\odot$ (Young et al., 2006). Theoretical calculations of the mass of dust formed from similar progenitor explosions include: 0.23 $M_\odot$ (Kozasa et al., 1991), 0.08–0.3 $M_\odot$ (Todini and Ferrara, 2001), 0.57 $M_\odot$ (Nozawa et al., 2003), and 0.2 $M_\odot$ (Cherchneff, 2010). The predictions are two to three orders of magnitude greater than the observed dust masses in SN1987A (with the exception of the work of Matsuura et al. (2011)). With such discrepancies, we are led to the question: how are dust mass predictions made?

1.2.2 Dust formation predictions

Current dust formation predictions are usually based on classical nucleation theory, which has seen only modest improvements since its initial formulations by Volmer and Weber (1926), Farkas (1927), and Becker and Döring (1935). This thermodynamic theory is quite powerful due to its ability to use broad generalizations about grain properties. It has seen some success by yielding nucleation rates in general agreement with laboratory experiments of some materials, such as water (Wölk and Strey, 2001), but has failed for other materials, such as chloroform (Dawson et al., 1969) and argon (Iland et al.,

2007; Sinha et al., 2010). However, the applicability of classical nucleation theory in astrophysical dust formation is questionable (Donn and Nuth, 1985). Classical nucleation theory employs the capillary approximation which assumes that all clusters, regardless of size, have the same surface tension as a macroscopic surface of the material. This approximation works well for large clusters, but breaks down for smaller clusters, like those formed in astrophysical environments. For small clusters, which can be only a few molecules thick, it is impossible to define what is "surface" and what is "bulk", especially for linear or flat isomers (see Figure 1.5 (Jones, 1999)). A theory which can account for the smallest clusters as well as the larger ones is necessary for describing dust formation in astrophysical settings (Donn and Nuth, 1985; Lazzati, 2008; Cherchneff, 2010).

Improvements need to be made to both the observations and theoretical models of dust formation. In order to correct inferred total dust masses, object such as SN1987A, Cas A, and Kepler are repeatedly observed with more advanced instruments. Instruments like *AKARI*, *Spitzer*, and *Herschel* are better able to detect dust at temperatures not previously observed, and allow astronomers to distinguish between dust formed in the expanding ejecta and preexisting dust that has been swept up. Theoretical models also need testing and reevaluation. This work aims at developing a nucleation theory which includes modifications that have been excluded from previous treatments, in order to refine predictions of dust mass formation.

Chapter 2

Nucleation

Dust formation in molecular clouds, dusty tori around AGNs, quasars, the expanding ejecta of CCSNe, the mass loss winds of Wolf-Rayet and AGB stars, and other astrophysical settings occurs through the process of nucleation. However, nucleation does not only occur in the cosmos, it is also easily seen here on Earth. A few examples of nucleation phenomena are the formation of clouds and atmospheric aerosols or other nanoparticles (Clement and Ford, 1989; Barrett et al., 1993), the freezing or boiling of water, the growth of crystals like rock candy from a supersaturated sugar-water solution, and the formation of bubbles in carbonated drinks like champagne, beer, or soda pop. These examples all involve a first-order phase transition – the formation of clusters of a new phase (solid, liquid, or gas) within the old phase.

This chapter discusses the basics of nucleation. A brief review of the first-order phase transition is given in Section 2.1. Section 2.2 describes the basics of nucleation theory. In Section 2.3 the classical nucleation theory and its strengths and weaknesses are presented. Section 2.4 describes some of the alternative nucleation theories that have been employed by other researchers. These theories focus on molecular interactions based on density functional theory, Monte Carlo and molecular dynamics methods, as well as the kinetic theory of nucleation and corrections to it.

2.1 First-order phase transition

The first-order phase transition is characterized by an abrupt change in one or more of the state variables of the system (Huang, 1987; Bowley and Sanchez, 1999). These

phase transitions can be caused through changes in pressure or volume, but the most intuitive cause is a change in temperature. Water is the substance we most often witness experiencing a phase transition. If liquid water is heated above 100° C ($\sim$ 373 K), it boils and forms steam, transitioning from liquid to vapor. Allow the steam to cool down below 100° C, and it will revert from its vapor phase back to its liquid phase. When the liquid water is cooled further, below 0° C ($\sim$ 273 K), it will freeze, becoming ice, transitioning from liquid to solid. It is possible, however, to supercool water below its freezing point, or to superheat it above the boiling point, and still have it remain liquid (Oxtoby, 1998; Bowley and Sanchez, 1999). In these cases, it takes a perturbation to the liquid to cause the phase transition. It should be noted that when the phase transition occurs, the temperature and pressure remain constant (Huang, 1987; Bowley and Sanchez, 1999). Why does the change in temperature cause the phase transition, and why does supercooled/superheated water require a perturbation to cause the transition?

The phase transition is the result of a decrease in the free energy of the system – the collection of water molecules. A system will settle into the phase that minimizes its free energy (Bowley and Sanchez, 1999). A phase can be considered to be stable when it has reached a minimum free energy state. When a system is supercooled or superheated, it can become trapped in a local energy minimum, rather than the global minimum. In this case the phase is only *metastable*. In the metastable state, a system will need to first increase its free energy, enough to overcome an energy barrier, in order to then settle into the even lower free energy state of the new phase (see Figure 2.1). The small perturbation to the supercooled/superheated water provides the extra free energy necessary to overcome the energy barrier and allow the water to freeze/boil.

For a phase transition at constant pressure and temperature, we are interested in the Gibbs free energy of the system G (Huang, 1987). To find the Gibbs free energy we follow the derivation of Stowe (1984). The differential form of the first law of thermodynamics can be written as

$$\mathrm{d}U = T\mathrm{d}\mathsf{S} - p\mathrm{d}V\,, \tag{2.1}$$

where U is the internal energy, T is the temperature, S is the entropy, p is the pressure, and V is the volume. We can rewrite the two terms on the right-hand side as

$$T\mathrm{d}\mathsf{S} = \mathrm{d}(T\mathsf{S}) - \mathsf{S}\mathrm{d}T \qquad \text{and} \qquad p\mathrm{d}V = \mathrm{d}(pV) - V\mathrm{d}p\,, \tag{2.2}$$

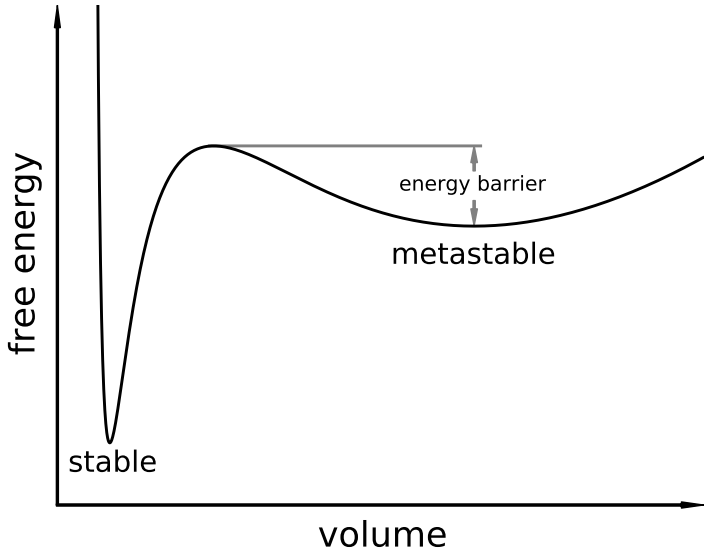

Figure 2.1: Free energy of a system in relation to its volume. For the system to transition from the metastable state to the stable state, it must overcome an energy barrier.

and rearrange Eq. (2.1) to obtain:

$$\mathrm{d}(U - T\mathsf{S} + pV) = -\mathsf{S}\mathrm{d}T + V\mathrm{d}p\,. \tag{2.3}$$

We can then define the Gibbs free energy as

$$G \equiv U - T\mathsf{S} + pV\,, \tag{2.4}$$

and

$$\mathrm{d}G = \mathrm{d}(U + pV - T\mathsf{S}) = V\mathrm{d}p - \mathsf{S}\mathrm{d}T\,, \tag{2.5}$$

as the variation in the Gibbs free energy. Minimization of the Gibbs free energy G is when $\mathrm{d}G = 0$, which occurs at constant pressure ($\mathrm{d}p = 0$) and temperature ($\mathrm{d}T = 0$). The internal energy U is given by

$$U = T\mathsf{S} - pV + \mu N\,, \tag{2.6}$$

where μN is the total chemical potential of the N particles in the phase. G can then be

found to be

$$G = \mu N \,. \tag{2.7}$$

The Gibbs free energy of the system of N particles is equivalent to the chemical potential of the phase μ times the number of particles in that phase.

Following Kashchiev (2000), we can write the Gibbs free energy for a van der Waals fluid in terms of the reduced volume $V' = V/V_{cr}$, pressure $P' = p/P_{cr}$, and temperature $T' = T/T_{cr}$, using the van der Waals equation of state

$$\left(P' + 3/V'^2\right)(3V' - 1) = 8T' \,, \tag{2.8}$$

as:

$$G(V', T') = G_{ref}(T') + NkT_{cr}[3P'V'/8 - 9/8V' - T' \ln(3V' - 1)] \,, \tag{2.9}$$

where V_{cr}, P_{cr}, and T_{cr} are the critical volume, pressure, and temperature, respectively. G_{ref} is a reference energy that we will arbitrarily set to $G_{ref} = 2NkT_{cr}$ (Kashchiev, 2000). We can then find the volume of the system when the Gibbs free energy is a minimum.

Figure 2.2 shows the nondimensionalized Gibbs free energy as a function of V' at $T' = 0.8$ and $P' = 0.420, 0.383$, and 0.350. We note that for each reduced pressure shown, the Gibbs free energy exhibits two minima (indicated by filled circles). The free energy values of these minima, however, are different for each reduced pressure. At $P' = 0.350$ (the blue curve) the minimum of the free energy at the smaller reduced volume is higher than at the larger volume. This indicates that the lower energy state for the system is at the larger volume, making the smaller volume state only metastable. For a system consisting of water molecules at $T' = 0.8$ ($T = 517$ K), the smaller volume state corresponds to the liquid phase, while the larger volume state corresponds to the vapor phase. Water already in the liquid phase would be trapped unless it could overcome the barrier between the two minima – the local maximum. When the reduced pressure is elevated to $P' = 0.420$ (the red curve), we find the liquid phase would be more stable because its free energy is now lower than the free energy of the vapor phase. Water in the vapor phase would need to overcome the energy barrier in order to condense into a liquid.

For this T' there exists a reduced pressure $P'_e = 0.383$ where the two minima are at equal free energies, and neither phase is more stable than the other. At this pressure, the so-called phase-equilibrium pressure $p_e = P'_e P_{cr}$, both phases can coexist. We can

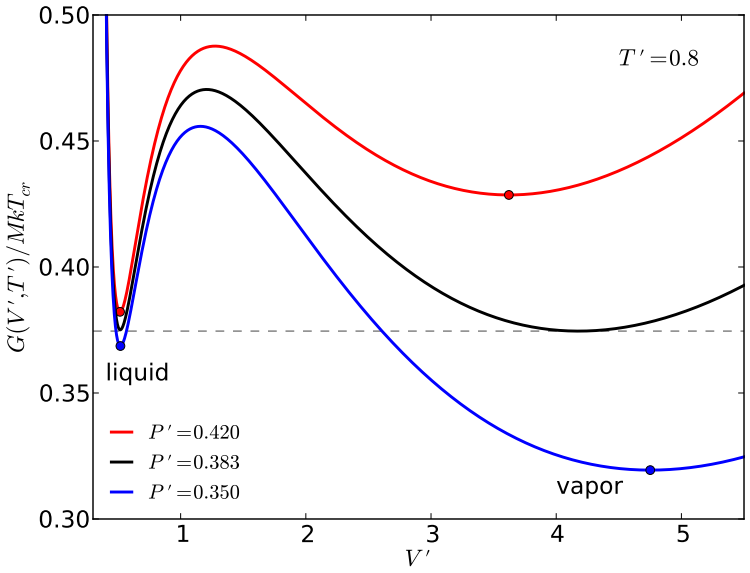

Figure 2.2: Nondimensional Gibbs free energy as a function of the reduced volume V' at reduced pressures $P' = 0.420$, 0.383, and 0.350. The horizontal, dashed line indicates the free energy at the phase-equilibrium pressure.

relate the reduced pressures, P', to the reduced equilibrium pressure P'_e to obtain a ratio of vapor pressures p to the phase-equilibrium pressure p_e:

$$\frac{P'}{P'_e} = \frac{p/P_{cr}}{p_e/P_{cr}} = \frac{p}{p_e}\,.$$

This ratio can be thought of as a measure of how much material is actually in the vapor phase versus how much could normally be held in the vapor phase at the given temperature, and is defined as the supersaturation

$$S \equiv \frac{p}{p_e}\,. \tag{2.10}$$

Figure 2.3 shows a plot of the locations of the liquid and vapor free energy minima for a series of reduced pressures as a function of the supersaturation S. For subsaturated vapors (supersaturation levels $S < 1$) the vapor phase minima (green curve) are lower than the liquid phase minima (blue curve) and the phase transition will proceed from liquid to vapor. Conversely, for supersaturated vapors ($S > 1$), the phase transition will

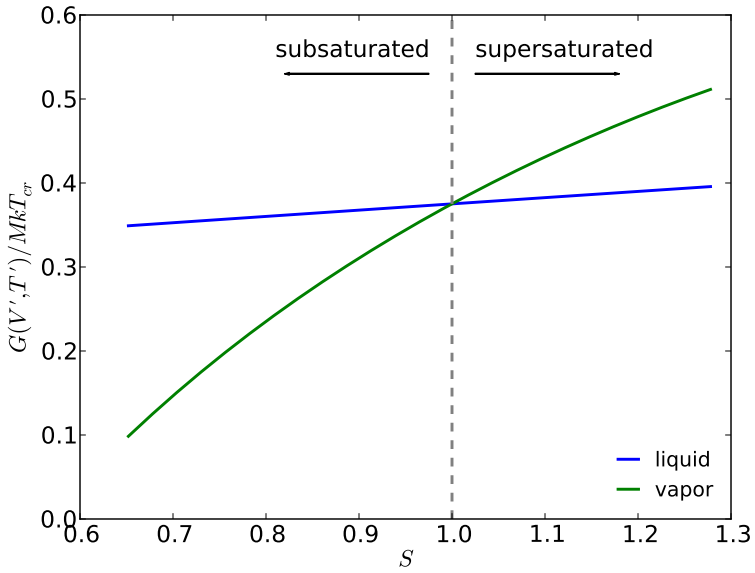

Figure 2.3: Gibbs free energy minima for liquid blue and vapor green phases as a function of supersaturation S. The free energy minima coincide at $S = 1$, as shown by the vertical, dashed line.

proceed from vapor to liquid. In general, phase transitions will move toward diluted phases in subsaturated vapors and toward condensed phases in supersaturated vapors.

2.2 Nucleation theory

It is unlikely that the whole system will undergo the first-order phase transition at once due to the large energy barrier that must be overcome (Kashchiev, 2000). It is more likely that portions of the system will change phases instead, because the energy barrier will be smaller. This is evident in the formation of the small water droplets that make up clouds (Kashchiev, 2000). Phase transitions can be separated into three stages: nucleation, coalescence, and aging (Kashchiev, 2000). During the nucleation stage, small nuclei form due to the random collisions of monomers (Farkas, 1927; Feder et al., 1966; Kashchiev, 2000; Merikanto et al., 2004; Vehkamäki, 2006). In the coalescence stage, nuclei grow due to collisions with additional monomers or other nuclei. Finally, in the aging stage, small-sized, unstable nuclei (clusters) tend to lose monomers and evaporate, while the

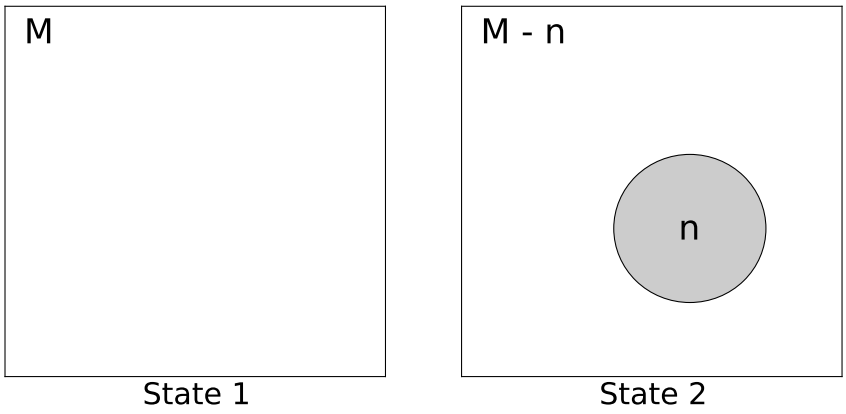

Figure 2.4: A system of M monomers before and after cluster formation (replica of Fig. 3.2 from Kashchiev (2000)).

larger, stable nuclei (grains) tend to gain the released monomers and grow even larger. Nucleation theory is concerned with describing the formation of the smallest grains.

2.2.1 Critical cluster

Since the energy barrier is smaller for the condensation of clusters rather than the whole system, it is necessary to consider the change in the Gibbs free energy $\Delta G(n)$, which is equivalent to the work of cluster formation W, based on the size of the cluster n.

In the following, we rederive the work to form an n-sized cluster as done in Kashchiev (2000). Consider a system of M monomers in the vapor phase, *State 1*, from which is formed a cluster of n monomers in *State 2*, as shown in Figure 2.4. The change in the Gibbs free energy of the system due to the cluster formation is

$$\Delta G(n) = G_2(n) - G_1\,, \tag{2.11}$$

where G_1 is the Gibbs free energy before cluster formation from Eq. (2.7):

$$G_1 = M\mu_{old}\,, \tag{2.12}$$

with μ_{old} being the chemical potential of the old vapor phase, and $G_2(n)$ is the Gibbs free energy of the system after cluster formation. $G_2(n)$ consists of two parts. The first

part is the the Gibbs free energy of the monomers that are still in the old phase, and the second part is the Gibbs free energy of the n-sized cluster in the new condensed phase $G(n)$ so that

$$G_2(n) = (M - n)\mu_{old} + G(n)\,. \tag{2.13}$$

The Gibbs free energy of the cluster also consists of two parts

$$G(n) = n\mu_{new} + G_{ex}(n)\,, \tag{2.14}$$

where μ_{new} is the chemical potential of the new phase and $n\mu_{new}$ is then the Gibbs free energy of a collection of n monomers in the new phase. $G_{ex}(n)$ is the *excess* free energy associated with the interface between the old and new phases. This excess free energy of the cluster surface is

$$G_{ex} = \Sigma\sigma\,, \tag{2.15}$$

where Σ is the surface area of the cluster and σ is the bulk surface energy per unit area specific to the nucleating material. Substitution of Eqs. (2.12)–(2.15) into Eq. (2.11) yields,

$$\Delta G(n) = -n(\mu_{old} - \mu_{new}) + \Sigma\sigma\,. \tag{2.16}$$

Using the definitions $\Delta\mu \equiv \mu_{old} - \mu_{new}$ and $c \equiv \Sigma/V^{2/3}$, where c is the dimensionless shape factor and V is the cluster volume equal to nv_0 with v_0 being the monomer volume, we obtain

$$\Delta G(n) = -n\Delta\mu + c\sigma(v_0 n)^{2/3}\,. \tag{2.17}$$

The difference in the chemical potentials of the two phases can also be written as $\Delta\mu = kT\ln(S)$ (Wölk and Strey, 2001). The first term in Eq. (2.17) is the reduction in the free energy due to the reduction in volume of the n monomers and the second term is the additional necessary energy associated with the formation of the cluster surface.

The dimensionless change in the Gibbs free energy is shown in Figure 2.5 for the formation of spherical ($c = (36\pi)^{1/3}$) water droplets at $T = 240$ K and supersaturation $S = 10$. The cluster size at which the change in the Gibbs free energy is a maximum is the smallest stable cluster size and is the so-called *critical cluster* (Wölk and Strey, 2001). In order to minimize the free energy of the system, clusters that are smaller than the critical cluster will evaporate since growing larger would require an increase in the free energy (Kashchiev, 2000). The opposite is true for the larger clusters, which will

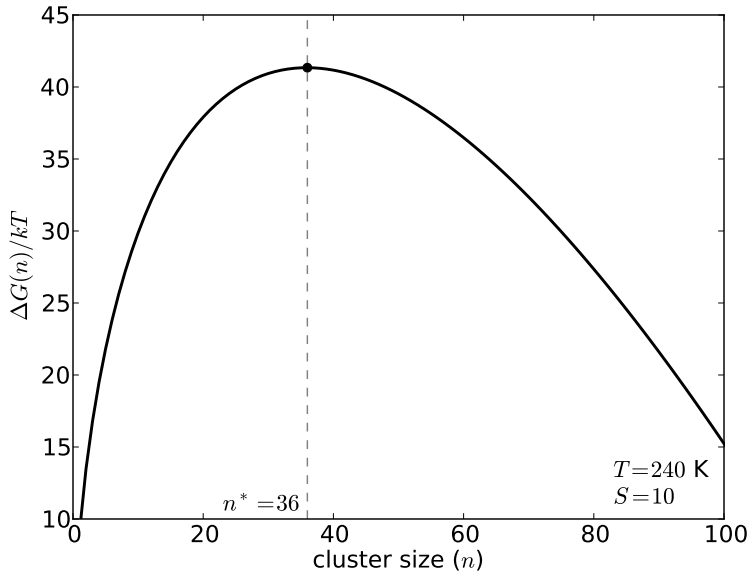

Figure 2.5: The change in the Gibbs free energy as a function of cluster size from Eq. (2.17) for spherical water droplets at $T = 240$ K and supersaturation $S = 10$. The cluster size at which the change in the Gibbs free is a maximum is the critical cluster size n^*.

reduce the free energy of the system by growing even larger.

2.2.2 Nucleation rate

The number of critical clusters that form per unit volume and time is the nucleation rate J. Most nucleation rate calculations are made through an equation of the form

$$J = A \exp\left(-\Delta G^*/kT\right), \tag{2.18}$$

first developed by Volmer and Weber (1926), where A is a kinetic prefactor and ΔG^* is the work to form the critical cluster. Both A and the work to form the critical cluster are specific to the nucleation theory being used (Wölk and Strey, 2001) and therefore we will substitute W^* for ΔG^*. Nucleation is usually considered to occur under the steady state conditions of constant temperature and supersaturation, so that in general the steady

state nucleation rate is found through

$$J_s = A \exp\left(-W^*/kT\right). \tag{2.19}$$

2.3 Classical nucleation theory (CNT)

The classical nucleation theory (CNT) is considered to come from the combined works of Volmer and Weber (1926), Farkas (1927), Becker and Döring (1935), Frenkel (1939), and Zeldovich (1943). Particular note is given to Becker and Döring (1935) who improved upon the work of Volmer and Weber (1926) by being the first to determine an expression for the kinetic prefactor A (Wölk and Strey, 2001). In light of these works,

$$A = z_Z f^* C_0 \,, \tag{2.20}$$

where z_Z is the Zeldovich non-equilibrium factor, with a value $0.01 < z_Z < 1.0$, which accounts for the probability that clusters slightly smaller than the critical cluster will grow large enough to become stable, and clusters that are slightly larger than the critical cluster will evaporate, f^* is the impingement rate of monomers onto the critical cluster, and C_0 is the concentration of nucleation sites (Kashchiev, 2000).

Becker and Döring (1935) also found an expression for the number of monomers contained in the critical cluster. The number of monomers in the critical cluster n^* is found with the help of the Gibbs-Thomson equation,

$$\ln S = \frac{2\sigma v_0}{r^* kT} \,, \tag{2.21}$$

and the volume of the critical cluster V^*,

$$V^* = n^* v_0 = \frac{4\pi {r^*}^3}{3} \,,$$

so that

$$n^* = \frac{32\pi v_0^2 \sigma^3}{3(kT \ln S)^3} \,, \tag{2.22}$$

(Wölk and Strey, 2001). Putting Eq. (2.22) into Eq. (2.17) to find the work necessary to form the critical cluster, the Becker and Döring nucleation rate can be found to be

$$J_{BD} = \sqrt{\frac{2\sigma}{\pi m_0}} v_0 \left(\frac{p}{kT}\right)^2 \exp\left(\frac{-16\pi v_0^2 \sigma^3}{3(kT)^3(\ln S)^2}\right), \tag{2.23}$$

where m_0 is the monomer mass (Wölk and Strey, 2001).

For the nucleation of water droplets, CNT (Eq. (2.23)) yields nucleation rates that are in general agreement with the expansion cloud chamber experiment results of Wölk and Strey (2001). In a typical expansion cloud chamber experimental run a vapor mixture containing the nucleation material and a carrier gas fills the expansion chamber. The chamber is expanded to reduce the pressure/temperature which raises the supersaturation level. The expansion is done quickly so that nucleation occurs at basically one supersaturation and temperature. Nucleation is allowed to continue for a short time ($\Delta t_{exp} \sim 1$ ms in Wölk and Strey (2001)), then the chamber is recompressed to shut off the nucleation process and the supersaturation decreases again (see Figure 1 of Strey et al. (1994)). Droplets that had nucleated are still able to grow, and the concentration of droplets in the resulting cloud is measured a few milliseconds after nucleation (Strey et al., 1994) through constant-angle Mie scattering (CAMS) methods (Wagner, 1985). The droplet concentration C_{exp} is then divided by the nucleation time Δt_{exp} in order to find the nucleation rate, $J_{exp} = C_{exp}/\Delta t_{exp}$ (Wölk and Strey, 2001).

The agreement between Eq. (2.23) and the experimental results of Wölk and Strey (2001) in Figure 2.6 is strongest for the data at $T = 240$ K. For the data at $T = 220$ and 230 K, CNT tends to under-predict the nucleation rate, while for $T = 250$, and 260 K, it over-predicts the rates. It can be seen that for water droplet nucleation CNT does not accurately reflect the temperature dependence seen in the experimental results (Wölk and Strey, 2001), by finding rates that too low at low temperatures and too high at high temperatures (Merikanto et al., 2004).

It should be pointed out that comparison of theoretical nucleation rates with experimental results is problematic. Expansion cloud chamber experiments observe only droplets that have grown to visible size, and not the flux of critical clusters as theory calculates (Feder et al., 1966). CAMS is applicable to situations measuring number concentrations of droplets with radii that are equal to and larger than the wavelength of the light used (Wagner, 1985). In earlier expansion cloud chamber experiments, a He-Ne

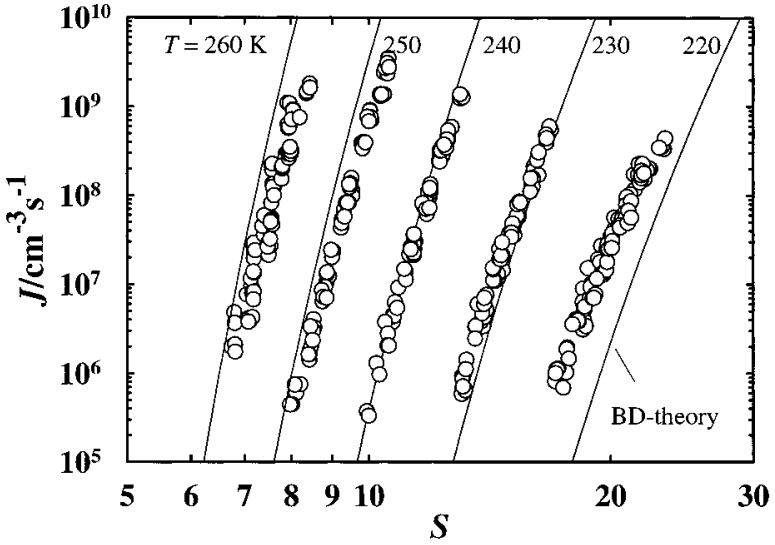

Figure 2.6: Figure 7 from Wölk and Strey (2001). Nucleation rates as a function of supersaturation S for water droplets at five temperatures between 220 and 260 K. Open circles are data points from expansion chamber experiments of Wölk and Strey (2001) and solid curves are rates calculated from Becker and Döring's stationary nucleation rate of Eq. (2.23).

laser was used to observe C_{exp} (Strey et al., 1994). The lowest wavelength for a readily available He-Ne laser is 543 nm (Thorlabs.com). A water droplet with a radius of 543 nm contains on the order of 10^{10} water monomers, however, critical clusters contain only 17–37 monomers for the experiments of Wölk and Strey (2001). After nucleation is shut off the supersaturation in the expansion chamber decreases, and the critical cluster size increases (see Eq. (2.22)). We expect clusters smaller than the critical cluster to evaporate. By waiting a few milliseconds after nucleation to measure the droplet concentration, there could be a number of droplets that are not counted because they have evaporated completely, or are too small to be observed. Therefore, the nucleation rates quoted in experiments may be too low due to these missing clusters. The warnings of Feder et al. (1966) are largely ignored, and comparisons between theory and experiment do not account for the difference between what is calculated and what is observed.

Comparing theoretical and experimental nucleation results, it has been noted that classical theory does well predicting the nucleation rates when monomers are rod-shaped, or the clusters are held together by hydrogen bonding (as in water clusters), but it is less successful when the monomers are regular-shaped or nonpolar, like chloroform

(Dawson et al., 1969). Further, CNT "fails dramatically" for the nucleation of liquid argon by estimating nucleation rates 16–26 orders of magnitude too small when compared to experimental values (Iland et al., 2007; Sinha et al., 2010). The reasons why CNT performs well for some substances and fails for others is not fully understood (Merikanto et al., 2007).

2.3.1 Corrections to CNT

The inadequacies of CNT have been considered to be mainly due to two causes (Merikanto et al., 2007): CNT miscalculates the cluster degrees of freedom and CNT applies macroscopic thermodynamic properties to microscopic clusters of only a few monomers (Lothe and Pound, 1962; Dillmann and Meier, 1991). Both of these causes can be traced back to CNT's reliance on the capillarity approximation in the calculation of the work of cluster formation $\Delta G(n)$. The use of the capillarity approximation in CNT treats the cluster, regardless of size, as having the bulk properties of the nucleated phase (Zeng and Oxtoby, 1991; McGraw and LaViolette, 1995; Oxtoby, 1998). Burton (1973) states that "the capillarity approximation fails for small cluster because it miscalculates the degrees of freedom", due to overestimating the number of surface monomers. Other bulk properties assumed to be the same are the surface tension, σ, and the chemical potential μ_{new}, as used in determining the work of cluster formation in Eq. (2.17). CNT also assumes that all clusters are the same shape, usually spheres.

While ultimately incorrect, these assumptions are not completely unfounded. Minimizing the free energy of the cluster requires minimizing the cluster's surface energy, and thus the cluster surface area. A sphere has the lowest surface area for a given volume, therefore the critical cluster will usually assume a spherical shape (Oxtoby, 1998). Also, as spherical clusters increase in size, the number of monomers contained within the sphere becomes much greater than the number of monomers that make up the surface. Therefore, it could be reasonable to assume that bulk properties will apply to these clusters. These assumptions work well for large clusters but fail for small ones. Small clusters have a large number of surface monomers compared to interior monomers. The surfaces of the small clusters are also sharply curved, which affects the surface tension (Moody and Attard, 2003). With these erroneous assumptions in mind, corrections to CNT have concentrated on corrections to the work of cluster formation.

Among the corrections to the work of cluster formation is the inclusion of translational

and rotational free energies in the cluster free energy $G(n)$ in Eq. (2.14) (Lothe and Pound, 1962; Feder et al., 1966; Burton, 1973). These additional energies have met with some controversy (Oxtoby and Evans, 1988). On the one hand, they represent a "more complete derivation of the free energy of formation," but on the other hand, they cause a loss of agreement between theory and experiment rather than an improvement (Feder et al., 1966). The Lothe-Pound correction results in nucleation rates that are too high by a factor of 10^{17} for water droplets at 300 K (Lothe and Pound, 1962). Nucleation rates for $CHCl_3$ (chloroform), C_6H_6, CCl_3F, C_6H_5Cl, and NH_3, however, are described much better by the Lothe-Pound theory than by CNT (Dawson et al., 1969).

Another correction to the work of cluster formation comes from an inconsistency in $\Delta G(n)$; Eq. (2.17) incorrectly calculates the work to form a monomer cluster because $\Delta G(1) \neq 0$ (Kashchiev, 2000; Wölk and Strey, 2001; Vehkamäki, 2006). A monomer in the vapor phase should be indistinguishable from a cluster consisting of just one monomer. Self-consistent models have been developed to account for this miscalculation (Girshick and Chiu, 1990; Kashchiev, 2000; Wölk and Strey, 2001). The simplest solution is to subtract the work to form a monomer from the work to form a cluster as in Girshick and Chiu (1990). This gives the work to form a cluster to be

$$\Delta\tilde{G}(n) = \Delta G(n) + \Delta\mu - c\sigma v_0^{2/3}\,, \tag{2.24}$$

and the nucleation rate is then given as:

$$\tilde{J} = A\exp\left(-\Delta\tilde{G}^*/kT\right) = J_{BD}\frac{\exp\left(c\sigma v_0^{2/3}/kT\right)}{S}\,, \tag{2.25}$$

where $\Delta\tilde{G}^*$ is the work to form the critical cluster and J_{BD} is same as in Eq. (2.23). For the nucleation of water droplets at 240 K and $S = 10$, this correction increases the nucleation rate by a factor of ~ 9000. In the case of toluene, this correction brings theoretical rates to only a factor of ~ 10 larger than experiment (Girshick and Chiu, 1990).

Inaccuracies in the surface tension σ of small clusters is a consequence of CNT's reliance on the capillarity approximation. The use of constant σ for small clusters ($\lesssim 50$ monomers) may be questionable (Feder et al., 1966; Dillmann and Meier, 1991; Oxtoby, 1998; Kashchiev, 2000). Corrections to the surface tension for small clusters has been a long standing problem in thermodynamics and statistical physics (Zhukhovitskii, 2001).

A 15% increase in σ results in a 10^{15} reduction in the nucleation rate while using the Lothe-Pound theory (Feder et al., 1966).

2.3.2 Additional assumptions of CNT

Aside from the use of the capillarity approximation, CNT makes additional assumptions about small clusters that may not be physically appropriate, especially when considering the formation of cosmic dust. The work of cluster formation in Eq. (2.17) allows for the formation of clusters of any regular shape, e. g. spheres and polyhedrons, through the shape factor c. However, theoretical works of dust formation in SNe consider only the formation of spherical grains. As seen in Figure 1.5, the isomers of $n = 24$ carbon clusters can assume various shapes, some of which are far from spherical. Increases in the shape factor from spherical $c \approx 4.84$ up to $c = 12.0$ can reduce the maximum nucleation rate by $\sim 10^3$ (Fallest et al., 2011).

Nearly all nucleation theory works also include the assumption that any monomer contacting the cluster will stick to it. This assumes a sticking probability of unity. The sticking coefficient $\gamma = 1.0$ can be explicitly written as an additional factor of the nucleation rate so that

$$J_s = \gamma A \exp\left(-W^*/kT\right). \tag{2.26}$$

Bianchi and Schneider (2007) and Fallest et al. (2011) investigated the effects of reduced sticking coefficients on the masses of dust formed from a CCSN. Bianchi and Schneider (2007) found that using a sticking coefficient of $\gamma = 0.1$ reduces the total mass formed from a 20 $M_\odot$ progenitor CCSN to 0.001–0.1 $M_\odot$, which is comparable to the inferred dust mass of SN1987A at 400–700 days after explosion. Fallest et al. (2011) found that the mass of carbonaceous grains was not significantly reduced for a sticking coefficient $\gamma = 0.1$, however, other dust species were not considered and the total dust masses for a 20 $M_\odot$ progenitor CCSN were not calculated (the entirety of Fallest et al. (2011) is presented as Chapter 3).

Finally, CNT considers nucleation to occur under conditions of thermodynamic equilibrium. However, each impinging monomer will increase the temperature of a cluster due to the release of latent heat (Feder et al., 1966). CNT does not take this effect into account. Alternative approaches have been employed to accommodate the temperature fluctuations, but have not treated the problem completely (Feder et al., 1966).

2.4 Alternate nucleation approaches

While CNT is the most widely used approach to nucleation (Schenter et al., 1999a; Merikanto et al., 2004; Kalikmanov, 2006; Matsubara et al., 2007), the fact that CNT rates agree with experiment as well as they do is "largely fortuitous" (Oxtoby, 1998). As seen in experiments of water and n-nonane, for a narrow range of supersaturation levels and temperatures, CNT is correct (Oxtoby, 1998; Schenter et al., 1999a), but in general CNT does not accurately predict the temperature dependence (Zeng and Oxtoby, 1991; Oxtoby, 1998; Wölk and Strey, 2001; Merikanto et al., 2004). The deficiencies of CNT have motivated the use of molecular approaches that can accurately describe the properties and behavior of small clusters through density functional theory methods (Oxtoby and Evans, 1988; Zeng and Oxtoby, 1991; Oxtoby, 1998), molecular dynamics (Senger et al., 1999; Merikanto et al., 2004, 2007; Matsubara et al., 2007), and kinetic approaches largely based on the earlier kinetic theory of Becker and Döring (1935). Molecular approaches are also based on the assumption that clusters grow and evaporate by the addition and loss of monomers (Schenter et al., 1999a). The problem then becomes determining which monomers belong to the cluster (Zeng and Oxtoby, 1991). Thus, much of the work in these approaches focuses on the definition of a cluster and how to distinguish between monomers that are part of the cluster and those which are not.

2.4.1 Density functional theory

The density functional theory (DFT) work of Oxtoby and Evans (1988), Zeng and Oxtoby (1991), and Oxtoby (1998) seeks to develop a theory that is not reliant upon the capillarity approximation and includes realistic molecular interactions. DFT formulates the work of cluster formation through functionals of the inhomogeneous density of a cluster, rather than its radius as in CNT (Oxtoby and Evans, 1988; Oxtoby, 1998). Figure 2.7 shows the density profile for water critical cluster at $T' = 0.6$ of Oxtoby and Evans (1988), where $T' = T/T_{cr}$. Also shown are the values for the liquid density $\rho_l(\mu)$, the liquid density when the liquid and vapor coexist $\rho_l(\mu_{coex})$, and the radius of the classical critical cluster R_{class}. Oxtoby and Evans (1988) finds that the density at the center of the critical cluster is lower than the density of the liquid phase, which is the density normally used in CNT calculations.

CNT assumes the existence of a phase boundary at the cluster surface to clearly

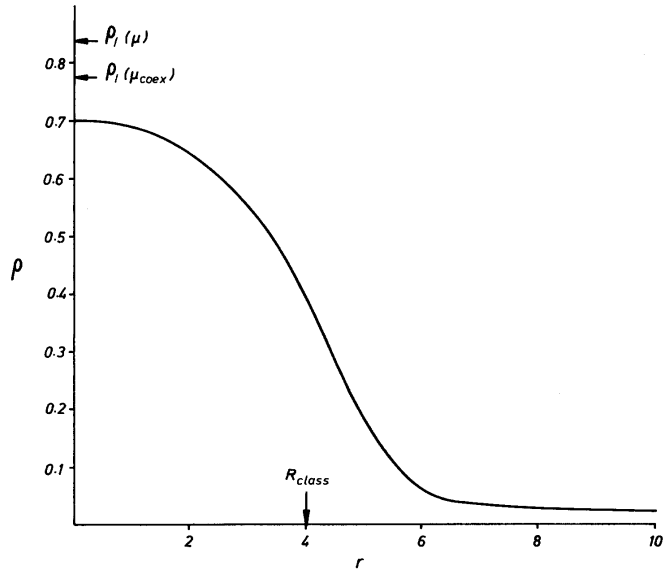

Figure 2.7: Fig. 1 from Oxtoby and Evans (1988). Density profile for a critical cluster at $T' = 0.6$. $\rho_l(\mu)$ is the liquid density at this T', $\rho_i(\mu_{coex})$ is the liquid density when the liquid and vapor can coexist, and R_{class} is the radius of the classical critical cluster.

differentiate cluster monomers from vapor monomers (Senger et al., 1999; Kashchiev, 2000). DFT, on the other hand, assumes the interface has some finite width over which the density changes, and only areas with high enough density are part of the cluster (Zeng and Oxtoby, 1991; Kashchiev, 2000). DFT has the advantage that the bulk macroscopic values of the density and surface tension are not used and the capillarity approximation has been removed (Zeng and Oxtoby, 1991; Oxtoby, 1998). Additionally, the curvature dependence of the surface tension naturally appears for small clusters, and at the limit of large clusters this method "goes over naturally to the classical theory" (Zeng and Oxtoby, 1991). The results of DFT calculations of the nucleation rate are promising, being in better agreement with some expansion cloud chamber experiments for water (Sharaf and Dobbins, 1982; Oxtoby and Evans, 1988). Moreover, DFT correctly predicts the temperature dependence of nucleation where CNT fails to do so (Oxtoby, 1998).

2.4.2 Molecular dynamics methods

Another approach to nucleation employs computer simulations to find the cluster free energy through Monte Carlo (MC) or molecular dynamics (MD) methods (Zeng and

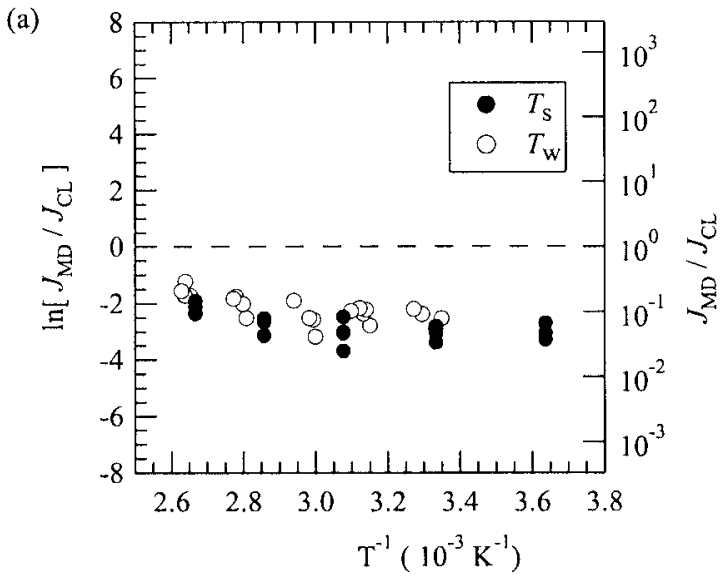

Figure 2.8: Fig. 6 from (Matsubara et al., 2007). Nucleation rates are compared for MD simulations and CNT. The nucleation temperature is found two ways, T_s and T_w.

Oxtoby, 1991; Merikanto et al., 2004; Matsubara et al., 2007; Merikanto et al., 2007). Correcting for the failures of CNT requires knowledge of small cluster behavior at the molecular level (Matsubara et al., 2007). Unfortunately, there are no experiments that directly observe the microscopic processes and computer simulations are needed instead (Merikanto et al., 2004). A typical MD simulation of Matsubara et al. (2007) considers a box containing 10000 water molecules and 10000 argon carrier gas molecules, and through interaction potentials between the molecules obtains rates of critical cluster formation. The definition of a cluster in these simulations is vitally important (Merikanto et al., 2004). In this case, a cluster is defined by the interaction energy between molecules. When the interaction energy is large enough, the molecule is considered bonded to the cluster (Matsubara et al., 2007). A network of connected molecules then forms a cluster (Merikanto et al., 2004). MC simulations of Merikanto et al. (2004) and Merikanto et al. (2007) obtain the correct temperature dependences, however, overall nucleation rates are not better than CNT. According to Matsubara et al. (2007), MD simulations predict nucleation rates that are not in agreement with CNT (see Figure 2.8) due to differences in the cluster structure and the kinetic prefactor A. Figure 2.8 shows the results from Matsubara et al. (2007) for the nucleation of water droplets. The J_{MD}/J_{CL}

ratios are shown for two methods of calculating the nucleation temperature T_s and T_w. T_s is the average temperature of all water and carrier gas molecules and the preset simulation temperature, and T_w is the average temperature of only the water molecules (Matsubara et al., 2007). The "lack" of agreement between CNT and MD simulations is a bit subjective considering the largest difference between them is less than two orders of magnitude.

2.4.3 Kinetic theory approaches

The kinetic theory of nucleation was also developed by Becker and Döring (1935). The kinetic theory describes nucleation by finding the rates of attachment and detachment of monomers to and from a cluster (Becker and Döring, 1935; Kashchiev, 2000). These rates need to be found for every n-sized cluster from $n = 2$ up to twice the critical cluster $n = 2n^*$ (Kashchiev, 2000). In its basic form this theory suffers from the same weaknesses as CNT, due to also relying on the capillarity approximation, spherical clusters, and bulk surface tension. In contrast to CNT, the kinetic theory implicitly takes the cluster shape into account, however, it assumes that each cluster size has just one shape.

Since cluster sizes as small as the dimer ($n = 2$) need to be considered, the kinetic theory of nucleation allows for corrections to the size dependent cluster properties such as the surface tension. The mean-field kinetic nucleation theory (MKNT) corrects the surface tension of a cluster based on its size and structure (Kalikmanov, 2006). MKNT assumes that clusters consist of interior monomers and surface monomers, but that the number of monomers in each fluctuates about some mean value (Kalikmanov, 2006). The changes in the number of surface monomers is accompanied by corresponding surface tension changes. For large clusters, MKNT recovers the behavior described by CNT, but differs widely for small clusters (Kalikmanov, 2006). Remarkably, MKNT results have been in good agreement with experimental nucleation rates for some substances for which CNT fails, as well as for some substances that are described well by CNT (Kalikmanov, 2006). The MKNT results are shown for argon in Figure 2.9a and for water in Figure 2.9b (nucleation rates are compared to both CNT and experimental results). For both argon and water, MKNT results agree better with experiment than the CNT results. The experimental rates for water in Figure 2.9b are taken from Wölk and Strey (2001) (circles) and Labetski et al. (2004) (squares). The experimental data from Wölk and Strey (2001) in this figure are the same data shown earlier in Figure 2.6.

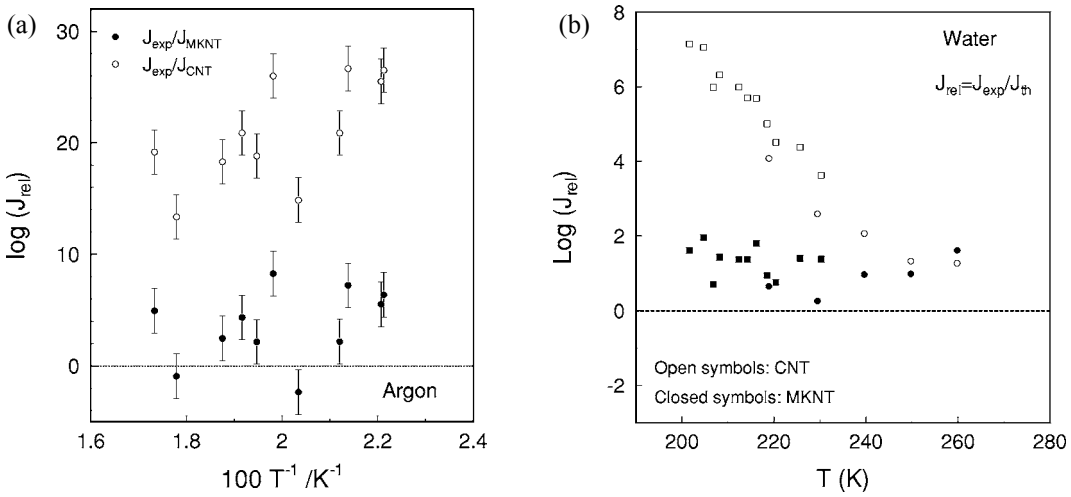

Figure 2.9: (a) Fig. 3 from (Kalikmanov, 2006) comparing nucleation rate found using CNT (open circles) and MKNT (filled circles) for argon. (b) Fig. 7 from (Kalikmanov, 2006) comparing nucleation rates found using CNT (open circles and squares) and MKNT (filled circles and squares) for water. The open circles correspond to the work of Wölk and Strey (2001).

Interestingly, the results of Wölk and Strey (2001) in Figure 2.6 show that CNT over-predicts nucleation rates compared to experimental results at $T = 250$ K and 260 K, however the results shown in Figure 2.9b suggest that CNT always under-predicts the nucleation rates for water.

The correction for the microscopic surface tension is just one of the corrections that can be made to the kinetic theory of nucleation. Another correction can be made to the work of cluster formation by using size dependent cluster sublimation energies that are derived empirically when possible, or through additional DFT, MC, and MD methods. Since the addition and loss of monomers cause temperature changes within the cluster, corrections based on temperature fluctuations also need to be taken into account (Feder et al., 1966; McGraw and LaViolette, 1995). The attachment rate depends sensitively on the temperature of the surrounding medium, while the detachment rate depends on the cluster temperature (Kashchiev, 2000). The cluster's internal energy is distributed throughout the cluster's vibrational degrees of freedom, and to eject a monomer enough of the energy needs to be concentrated into a single degree of freedom (Guhathakurta and Draine, 1989). The probability that this occurs can be made through an application of Rice-Ramsberger-Kassel (RRK) theory for an Einstein model cluster and a correction

to cluster's detachment rate found (Robinson and Holbrook, 1972; Guhathakurta and Draine, 1989). The kinetic theory of nucleation and modifications to the cluster sublimation energy, and temperature fluctuations, and corrections to the detachment rate for small clusters are discussed in greater detail in Chapter 4.

2.4.4 Approach of this project

This dissertation is concerned with the nucleation of dust grains in the expanding gases of supernova ejecta. As the gases expand and cool, they become supersaturated, and the phase transition is expected to occur from vapor to solid. We assume that the gas particles behave as ideal gases and we adopt the following standard equation of state when necessary throughout the remainder of this work:

$$pV = NkT\,, \tag{2.27}$$

where N is the number of monomers (atoms or molecules) and k is the Boltzmann constant. Pressures p, number densities $n_d = N/V$, and gas temperatures T, are the quantities to be used for finding the Gibbs free energies and the supersaturations S.

In light of the variety of previous works to improve nucleation theory discussed here, and with consideration to the environments in which cosmic dust forms, this dissertation work seeks to include modifications to nucleation theory to address the following concerns:

cluster shape –

As shown in Figure 1.5, small clusters can assume many shapes, some of which are clearly not spherical as assumed in previous nucleation treatments. Larger clusters are also expected to take on aspherical shapes as dust grains polarize starlight (Draine, 2003), indicating that grains have some measure of being aspheric. The vast majority of nucleation work considers only the formation of spherical clusters and grains. The shape factor c appears in both the kinetic prefactor A and the work of cluster formation W^* in CNT. Likewise, in the kinetic theory of nucleation, the shape factor appears in calculations of the attachment and detachment rates of a monomer to and from the cluster. The kinetic theory of nucleation has the advantage that a different shape factor for each cluster size can be naturally accommodated.

sticking coefficient –

One of the basic assumptions of nucleation theory is that during the nucleation stage, nuclei form through random collisions with monomers. Furthermore, it is assumed that any monomer that contacts a cluster will adhere to it. However, this may not always be the case. When considering the different shapes and structures a cluster of monomers can assume, some structures may be better able to accept an additional monomer. For example, a monomer might easily be added to the end of a linear chain of monomers, but a monomer might not so easily join an existing ring structure, since each monomer is already connected to its neighbors. Also, the monomers in a cluster may become ionized through interactions with electrons, atoms, or other ions, causing the cluster to become electrically charged. Charged monomers will be less likely to attach to similarly charged clusters. This barrier to attachment reduces the number of critical clusters being formed, thus reducing the nucleation rate. We can account for this reduction through the sticking coefficient γ as an additional factor in each f_n and g_n.

capillarity approximation –

As stated earlier, the reliance on the capillarity approximation results in incorrect descriptions of the properties of small clusters through the surface tension σ, and in the work of cluster formation. The reliance on the capillarity approximation can be addressed by considering the surface tension dependence on the size and curvature of the clusters as done in MKNT. This may not completely address the surface tension problem. In the case of water, the surface tension is also dependent on the temperature. Therefore, the temperature dependence of the surface tension needs to be considered as well. Another method for disposing of the capillarity approximation is to find $W(n)$ through size dependent sublimation energies B_n. When empirical data is available to find the sublimation energy, the surface tension can be eliminated from the kinetic theory of nucleation. However, in the absence of empirical data, sublimation energy calculations will still rely on surface tension values.

temperature fluctuations –

The temperature of a cluster is influenced by various means. The addition of a monomer results in the release of latent heat and a corresponding increase in the temperature of the cluster. Analogously, the loss of a monomer reduces the cluster temperature. Collisions with other atoms and molecules, which do not adhere to the clusters, also influence the cluster temperature. These collisions tend to regulate the cluster temperature by giving energy to cold clusters, and carrying away excess energy from hot ones. Much of the dust formation in astrophysical settings occurs in radiation rich environments. Dust clusters and grains absorb radiation in the visible range, obscuring observations as discussed in Chapter 1. The absorption of this radiation also increases the cluster temperature. The radiation is then reradiated, often in the infrared range, reducing the cluster temperature. Temperature fluctuations are greater in smaller clusters because the energy change due to a single event represents a larger fraction of the total energy of the cluster. These temperature fluctuations cannot be addressed by CNT. MD simulations are particularly well suited to including these effects, but are computationally expensive. The kinetic theory of nucleation can also be adopted to accommodate temperature fluctuations, since the detachment rates g_n are sensitive to the cluster temperature, while the attachment rates f_n are dependent only on the temperature of the surrounding environment.

detachment rate corrections for small clusters –

To minimize free energy, a cluster will either evaporate or grow depending on if it is smaller or larger than the critical cluster (see Figure 2.5). For a cluster to evaporate a monomer must detach from the cluster, reducing the cluster temperature. To evaporate further, more monomers must also detach, causing further temperature reductions. How much the temperature is reduced depends on how much energy a detached monomer carries away – the kinetic energy. The rate of monomer detachment is sensitive to the temperature of the cluster, becoming smaller as the temperature is reduced. Thus, after detachment the lower cluster temperature im-

pedes the detachment of subsequent monomers. It becomes likely that a monomer will attach to the cluster before another monomer will detach. Stable clusters, that are smaller than the critical cluster, may therefore exist because they are too cold to evaporate. This effect is in direct competition with the minimization of the cluster free energy, which expects the detachment rate to increase as a cluster get smaller. To account for this behavior, a correction can be applied to reduce the detachment rate g_n. Using an "Einstein model" to treat the cluster as a collection of harmonic oscillators, and applying Rice-Ramsberger-Kessel (RRK) theory, we can determine (i) the probability that sufficient energy will be concentrated into a single vibrational degree of freedom in order to break a monomer free and (ii) how much kinetic energy is carried away by the monomer.

Due to the importance of the behavior of small clusters in nucleation phenomena, to account for the concerns above, molecular scale approaches are appropriate. Effects due to an increased shape factor c and a reduced sticking coefficient γ can be applied to CNT, as presented in Chapter 3, however, the size dependent nature of them cannot be taken into account. Also, attempts to correct the work of cluster formation to negate the reliance on the capillarity approximation in CNT have resulted in destroying agreement between theory and experiment. Temperature fluctuations and the possibility of cold, stable clusters smaller than the critical cluster cannot be accounted for using CNT. The inadequacies of CNT in accurately describing the nucleation of a variety of substances, the criticism of CNT's applicability in astrophysical environments, and the promising results of theories concentrating on cluster microscopic properties and molecular interactions have motivated the decision to approach the problem of dust formation through the kinetic theory of nucleation. We will adopt the basic kinetic nucleation rate equation of Becker and Döring (1935),

$$J_s = f_1 C_1 \left[1 + \sum_{n=2}^{M-1} \frac{g_2 g_3 \ldots g_n}{f_2 f_3 \ldots f_n} \right]^{-1} , \tag{2.28}$$

where the attachment and detachment of monomers to and from the n-sized cluster are described by f_n and g_n, respectively, C_1 is the concentration of monomers and M is

the total number of monomers in the system, but it is sufficient to consider it as the maximum cluster size necessary to assure convergence of the summation. A thorough discussion of Eq. (2.28) is presented in Chapter 4.

The formation of cosmic dust occurs as a first-order phase transition through the process of nucleation. While a common phenomenon, nucleation is still poorly understood (Vehkamäki, 2006). Usually, classical nucleation theory has been employed to describe the dust formation process. However, inadequacies in the theory have been revealed through comparison with experimental results of the nucleation rates and temperature dependencies. These inadequacies are likely due to incorrect treatments of small clusters. Corrections to CNT have not succeeded in improving agreement between theory and experiment, and often just make matters worse. Microscopic approaches through molecular interaction theories seem to be promising alternatives (Schenter et al., 1999b). But, density functional theory methods are limited to simple types of interactions (Kalikmanov, 2006) and comparisons of molecular dynamics results with experiment is still impractical (Matsubara et al., 2007). The use of the kinetic theory of nucleation including a correction for the microscopic surface tension yields good agreement between theory and experiment. However, theories incorporating other size and temperature dependent properties of small clusters are necessary for developing a complete nucleation theory.

Chapter 3

On the effects of microphysical grain properties on the yields of carbonaceous dust from type II SNe

David W. Fallest, Takaya Nozawa, Ken'ichi Nomoto, Hideyuki Umeda,
Keiichi Maeda, Takashi Kozasa, and Davide Lazzati

This chapter was published in its entirety in:
Monthly Notices of the Royal Astronomical Society,
Volume 418, Issue 1, pp. 571–582

Abstract

We study the role of the unknown microphysical properties of carbonaceous dust particles in determining the amount and size distribution of carbonaceous dust condensed in type II supernova explosions. We parametrize the microphysical properties in terms of the shape factor of the grain and the sticking coefficient of gas-phase carbon atoms onto the grain surfaces. We find that the amount of dust formed is fairly independent of these properties, within the parameter range considered, though limited by the available amount of carbon atoms not locked in CO molecules. However, we find that the condensation times and size distributions of dust grains depend sensitively on the microphysical parameters, with the mass distributions being

weighted toward larger effective radii for conditions considering grains with higher sticking coefficients and/or more aspherical shapes. We discuss that this leads to important consequences on the predicted extinction law of SN dust and on the survival rate of the formed grains as they pass through the reverse shock of the SN. We conclude that a more detailed understanding of the dust formation process and of the microphysical properties of each dust species needs to be achieved before robust prediction on the SN dust yields can be performed.

3.1 Introduction

Interstellar dust, once considered to be little more than a nuisance to astronomical observations, is one of the most interesting areas of astrophysical research today (Li and Greenberg, 2003). One aspect of particular interest is the origin of dust at high redshift ($z > 5$). Possible sources of interstellar dust that have been considered include outflows from asymptotic giant branch (AGB) stars (Morgan and Edmunds, 2003; Zhukovska et al., 2008; Valiante et al., 2009), Wolf-Rayet systems (Cherchneff, 2010), quasars (Elvis et al., 2002), and supernova explosions (Kozasa et al., 1989, 1991; Todini and Ferrara, 2001; Nozawa et al., 2003; Bianchi and Schneider, 2007; Kozasa et al., 2009; Cherchneff, 2010). How much dust can be attributed to each of these possible sources at such high redshift remains unclear. Supernovae (SNe) are considered by some to be likely contributors of much of the dust in the early Universe because their progenitors are quite massive and consequently have short lifetimes (Bromm et al., 2002; Morgan and Edmunds, 2003; Maiolino et al., 2004; Dwek et al., 2007). However, such early SNe have not been observed, making determinations of their dust contributions difficult. Instead we need to consider dust yield predictions of more recent SNe, which have been observed, and then extrapolate the dust yields to earlier SNe. The theoretical predictions of dust yields for recent supernovae (Kozasa et al., 1991; Todini and Ferrara, 2001; Nozawa et al., 2008), however, are too large compared to observations, with discrepancies that can be as high as 3 to 4 orders of magnitude in some cases (Hoyle and Wickramasinghe, 1970; Lucy et al., 1989; Wooden et al., 1993; Elmhamdi et al., 2003; Meikle et al., 2007; Kotak et al., 2009). Observations of young supernova remnants (SNR), however, have confirmed dust masses one to two orders of magnitude greater than SNe. Some of these SNR have ob-

served dust masses of 0.02–0.054 $M_\odot$ by *Spitzer* (Rho et al., 2008), 0.06 $M_\odot$ by *AKARI* (Sibthorpe et al., 2010), and 0.075 $M_\odot$ by *Hershel* (Barlow et al., 2010), in Cassiopeia A, and 0.04–0.1 $M_\odot$ by *Spitzer* in the pulsar wind nebula G54.1+0.3 (Temim et al., 2010). Additionally, Nozawa et al. (2010) have demonstrated that the observed spectral energy distribution of Cassiopeia A can be well reproduced by the calculations of dust formation in Type IIb SNR and the mass in the SNR is 0.07 $M_\odot$.

Reconciling the dust yield prediction for local SNe can be done via one of two channels: improving our understanding of the dust formation process, leading to a substantially decreased prediction, or revising the observational constraints to account for a higher dust yield than so far implied. It is possible that some amount of dust has avoided observation. Dust particles absorb light and re-emit the energy at infrared wavelengths. However, cold dust at temperatures of a few tens of Kelvin could escape detection at mid-infrared wavelengths. Additionally, areas where the dust is optically thick could obscure some amount of dust, again allowing some dust to not be detected. Dust clumping may also affect the estimates of dust mass from absorption (Bianchi and Schneider, 2007), since it is usually assumed that the surface filling factor of dust is close to unity, while substantial clumping could be present due to the intrinsic inhomogeneity of the ejecta and Rayleigh-Taylor instabilities in the expanding ejecta (Wooden, 1997; Douvion et al., 1999).

On the theoretical side, all the estimates for dust production in SNe are based on the so-called classical theory of nucleation (e.g., Becker and Döring (1935)). It has been argued, however, that the use of classical nucleation theory in astrophysical environments is questionable (Donn and Nuth, 1985; Lazzati, 2008). In addition, almost all SN dust nucleation models thus far have considered the formation of spherical grains, and assumed any atoms/molecules that contact the grain will adhere to the grain; conditions that reflect maximally efficient nucleation. It is therefore not entirely surprising that the theoretical estimates of SN dust yields, based on upper limit of nucleation efficiency, are in excess of those from observations. It should be noted that Bianchi and Schneider (2007) have considered less than maximally efficient nucleation by assuming the probability of atoms/molecules adhering to the grain is less than unity, resulting in smaller dust yields.

Since dust formation is a highly non-linear phenomenon, understanding the effects of different nucleation rates on the final dust yields is difficult. To check the effects of different nucleation conditions we have performed a parametric study, in which we consider

carbonaceous dust production in a SN explosion by varying the shape of the forming grains as well as the sticking coefficient, i.e., the probability that an incoming monomer will stick to the grain rather than bounce off and remain in the gas phase. Our study is phenomenological and aims at understanding which conclusions of previous nucleation studies are robust to changing the parameters, and which may need to be investigated more thoroughly. A self-consistent nucleation model in astrophysical conditions will be achieved by involving a kinetic approach (Donn and Nuth, 1985; Lazzati, 2008; Keith and Lazzati, 2011) and detailed chemistry of precursor molecules (Cherchneff and Dwek, 2009, 2010). Such a detailed approach, however, is still under development and is not yet applicable to large scale simulations like the one that we use here, and that have been used in previous investigations of e.g., Todini and Ferrara (2001); Nozawa et al. (2003, 2010).

This paper is organized as follows: in Section 3.2 we detail the nucleation theory that we adopted; in Section 3.3 we describe the numerical code used for the computations; and in Section 3.4 we describe our results. In Section 3.5 we finally discuss the implication and limitations of our results and lay out future perspectives for SN dust studies.

3.2 Nucleation

Nucleation is the first step of a first-order phase transition. In the case we consider here, the phase transition is from a gas of carbon atoms to solid clusters of amorphous carbon dust. There is a phase equilibrium pressure where both the gas and solid phases are stable within a given volume. The phase equilibrium pressure depends on the temperature of the materials in the gas phase within the volume. Nucleation of clusters of atoms/molecules of the new phase is favoured when the gas phase is supersaturated (i.e., the pressure of the gas is higher than the phase equilibrium pressure). The higher the supersaturation (i.e., the ratio of the pressure to the phase equilibrium pressure), the smaller the size of the stable clusters that are able to form. The size of the smallest stable cluster able to form at a given temperature and density is called the critical cluster size. Clusters that are smaller than the critical size will tend to evaporate, while larger clusters will tend to continue to grow. The goal of any nucleation theory is to calculate how many critical clusters form per unit volume per unit time.

The classical theory of nucleation considers nucleation as a thermodynamical process

in quasi-equilibrium (Becker and Döring, 1935; Feder et al., 1966; Kashchiev, 2000). Besides the supersaturation level, the physical properties of the nucleating material affect the size of a critical cluster. The classical nucleation theory assumes that all clusters share the same properties, such as surface tension and shape, independent of their size. The theory also assumes that those properties are equal to those of a macroscopic sample. Moreover, the clusters are assumed to have a uniform equilibrium temperature that is equal to the temperature of the surrounding gas. These basic assumptions are problematic because macroscopic thermodynamic properties are not expected to be applicable to clusters of only a few atoms.

A different approach is provided by the kinetic theory of nucleation, which is applicable to very small cluster sizes. The kinetic theory relies on calculating the attachment and detachment frequencies of monomers to a cluster (Kashchiev, 2000). Furthermore, in contrast to the classical nucleation theory, the kinetic theory follows the formation of clusters smaller than the critical cluster size. In the framework of the kinetic theory the critical cluster is the cluster whose attachment and detachment frequencies are equal, and thus it is stable. The downside of the kinetic theory is that attachment and detachment frequencies for all cluster sizes need to be calculated in order to determine the overall nucleation rate. The main aim of this paper is to reveal the dependence of dust formation processes on the microphysical properties of grains. In order to achieve this, we adopt the simpler classical nucleation theory, rather than using the kinetic theory that demands a more complicated treatment.

When the supersaturation level is $S > 1$, nucleation can take place because the free energy of the new phase is lower than that of the old phase (Kashchiev, 2000). The change in the free energy is due to the work necessary to form the critical size clusters. Energy is released in the formation of the volume of the cluster, but energy is required in order to form the surface of the cluster (Kashchiev, 2000). The nucleation rate (Eq. (3.1)) is given basically by two factors: the number density of critical clusters and a kinetic factor that describes the rate at which clusters become large enough to be stable (i.e., critical size or larger).

The general equation of stationary nucleation is given by (Kashchiev (2000), their equation 13.39):

$$J_s = A \exp\left(-W^*/kT\right), \tag{3.1}$$

where A is the kinetic factor, W^* is the work needed to form the critical size cluster

from the gaseous state, k is the Boltzmann constant, and T is the gas temperature. The kinetic factor, A, is given by $A = A' \exp(\Delta\mu/kT)$, and A' is:

$$A' = \gamma^* \left(\frac{c^3 \sigma}{18\pi^2 m_0} \right)^{\frac{1}{2}} \left(\frac{p_e v_0}{kT} \right) C_0,$$

where γ^* is the size dependent sticking coefficient, c is the shape factor of the cluster, σ is the surface tension, m_0 and v_0 are, respectively, the mass and volume of the monomer of nucleating material, p_e is the phase-equilibrium pressure, and C_0 is the concentration of sites where nucleation can occur (equations 13.41 and 13.44, respectively in Kashchiev (2000)). The concentration of gaseous monomers, C_1 is related to the concentration of nucleation sites by $C_1 = C_0 \exp(-W_1/kT)$, where W_1 is the work needed to form a cluster consisting of one monomer (equation 7.5 in Kashchiev (2000)). We consider the monomer in the gaseous state to be indistinguishable from the monomer in the condensed state, so that $W_1 = 0$ and $C_1 = C_0$. Using the supersaturation ratio, $S = C_1/C_{1,e} = p/p_e$ and $\Delta\mu = kT \ln S$, where $C_{1,e} = p_e/kT$ is the gaseous monomer concentration at the phase-equilibrium pressure and p is the partial pressure of gaseous monomers, we obtain

$$A = \gamma^* \left(\frac{c^3 v_0^2 \sigma}{18\pi^2 m_0} \right)^{\frac{1}{2}} C_1^2.$$

While the sticking coefficient may depend on the size of the cluster, we consider it to be constant, so that $\gamma^* = \gamma =$ constant. Finally, using the work to form a critical sized cluster $W^* = 4c^3 v_0^2 \sigma^3 / 27\Delta\mu^2$ (Kashchiev (2000), equation 4.8), we find our stationary nucleation rate equation to be:

$$J_s = \gamma \left(\frac{c^3 v_0^2 \sigma}{18\pi^2 m_0} \right)^{\frac{1}{2}} C_1^2 \exp\left(\frac{-4c^3 v_0^2 \sigma^3}{27(kT)^3 (\ln S)^2} \right). \tag{3.2}$$

After nucleation the clusters grow through impingement of monomers upon the cluster. To find how much the clusters grow we begin by finding the volume of the newly nucleated cluster. The clusters nucleate with some critical number of monomers, n^* (equation 4.7 in Kashchiev (2000)):

$$n^* = \frac{8c^3 v_0^2 \sigma^3}{27\Delta\mu^3}. \tag{3.3}$$

The volume of the critical cluster is then, $v^* = n^* v_0$. The change in the cluster's volume over time depends on the sticking coefficient γ, the surface area of the cluster Σ, the concentration of monomers C_1, the volume of the monomer v_0, and the average relative speed of the monomers with respect to the cluster. In this paper we consider clusters that can nucleate with aspherical shapes through the use of the shape factor c. The shape factor is a dimensionless quantity that relates the surface area Σ of an object to its volume V by: $c = \Sigma/V^{2/3}$ (Kashchiev, 2000). Thus we find the change in volume over time to be:

$$\frac{dV}{dt} = \gamma c V^{\frac{2}{3}} C_1 v_0 \left(\frac{kT}{2\pi m_0}\right)^{\frac{1}{2}}. \tag{3.4}$$

In the same manner as Nozawa et al. (2003) we compute the depletion of the available nucleation material through mass conservation:

$$1 - \frac{C_1(t)}{\tilde{C}_1(t)} = 1 - Y_1 = \int_{t_e}^{t} \frac{J(t')}{\tilde{C}_1(t')} \frac{V(t,t')}{v_0} dt', \tag{3.5}$$

where $\tilde{C}_1$ is the nominal concentration of monomers – the concentration expected should nucleation not occur, which in an expanding shell of volume V_{shell} can be found using

$$\tilde{C}_1(t = t_n) V_{shell}(t = t_n) = \tilde{C}_1(t = t_0) V_{shell}(t = t_0),$$

so that the total number of gas-phase atoms remains constant, and $V(t, t')$ is the volume of a cluster formed at time t' and measured at time t. Rather than computing the integral on the right-hand side, we instead calculate $C_1(t)$ as described in step (iii) in the next section. From Eqs. (3.2) and (3.4), we see that J_s and dV/dt are simply proportional to the sticking coefficient γ. Thus, we expect that reduced sticking coefficients will suppress both nucleation and grain growth. The dependence of J_s on the shape factor c is more complicated, since it appears in both the kinetic factor and the exponential term. The shape factor in the exponential term, however, will dominate the nucleation rate equation and we expect that increased shape factors will suppress nucleation. On the other hand, grain growth (dV/dt) is simply proportional to c, and thus an increase in the shape factor will increase the cluster growth rate.

Table 3.1: Carbon properties

$A/10^4$ (K)	B	σ (erg·cm^{-2})	v_0 (10^{-24} cm^{-3})	m_0 (10^{-23} g)
8.64726	19.0422	1400	8.805	1.995

3.3 Simulations

We concentrate on the formation of carbonaceous grains (clusters) from carbon atoms in the expanding material of a core-collapse supernova. Our simulations are based on the hydrodynamic results and elemental composition for the unmixed ejecta of a core-collapse supernova of a 20 $M_\odot$ progenitor star with metallicity $Z = 0$ and an explosion energy of 10^{51} ergs by Umeda and Nomoto (2002) (see also Nomoto et al. (2006)).

Table 3.1 describes the data necessary for the calculation of carbon grain formation. To compute the supersaturation of the expanding gas, we find the phase equilibrium pressure by: $p_e = p_0 e^{-A/T+B}$, where p_0 is the standard pressure, T is the temperature, and the values of A and B, listed here in Table 3.1, are taken from Table 2 of Nozawa et al. (2003). As the material ejected by the core-collapse supernova expands it also cools. Figures 3.1 and 3.2 show the evolution of the density and temperature, respectively, of the expanding and cooling material for two of the enclosed mass subshells that we refer to in the rest of this work.

We study four different values of the unknown sticking coefficient, $\gamma = 1.0$, 0.1, 0.01, and 0.001, neglecting any dependence of γ on the temperature of the gas and the size of the cluster. For each value of the sticking coefficient, we study six different values for the shape factor, $c = (36\pi)^{1/3}$, 5.4, 6.0, 7.0, 9.0, and 12.0, corresponding to shapes ranging from a sphere to a flattened cylinder similar to a coin. We therefore performed 24 simulations in total. A sticking coefficient of $\gamma = 1.0$, and a shape factor for a sphere of $c = (36\pi)^{1/3}$ are the usual parameters used in previous nucleation works.

As in Nozawa et al. (2003), we assume that the stable formation of CO molecules occurs prior to grain nucleation and that carbon grains will form only where the initial number fraction of carbon is higher than that of oxygen. Under this assumption, the number fraction of free carbon atoms available for dust formation is obtained simply from the initial number fraction of carbon minus the number fraction oxygen. We divide the expanding gases into a series of enclosed mass shells beginning at ~ 4.93 $M_\odot$ and ending

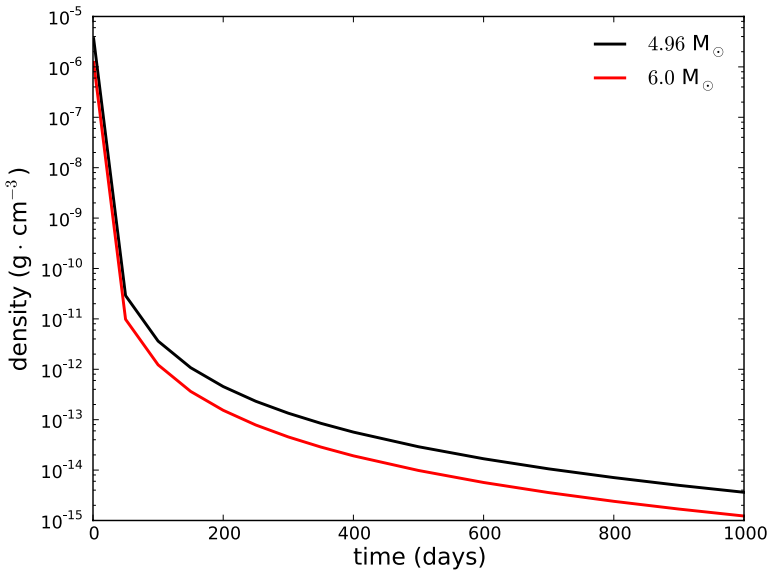

Figure 3.1: Density evolution for 4.96 (black) and 6.0 (red) $M_\odot$ enclosed mass subshells up to 1000 days after the SN explosion.

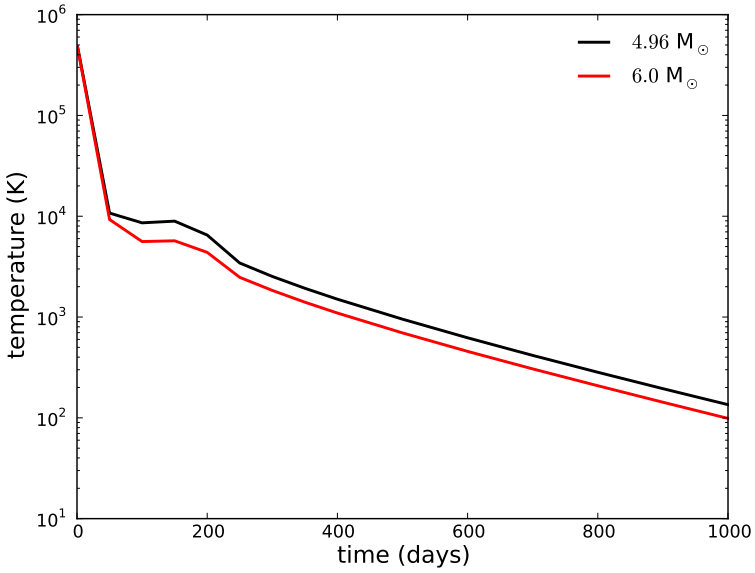

Figure 3.2: Temperature evolution for 4.96 (black) and 6.0 (red) $M_\odot$ enclosed mass subshells up to 1000 days after the SN explosion.

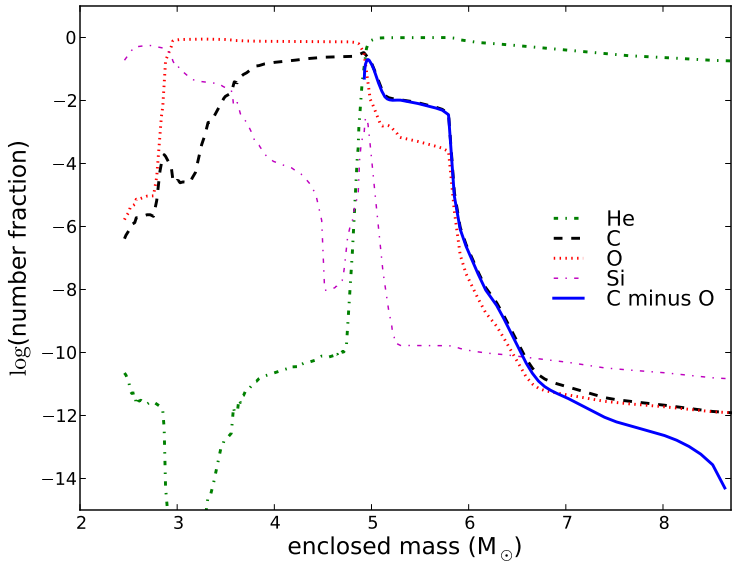

Figure 3.3: Number fraction of helium (green dash-dot), carbon (black dashed), oxygen (red dotted), and silicon (magenta dash-dot) atoms for enclosed masses from 2.45 to 8.7 $M_\odot$. The solid (blue) line is the carbon number fraction after the formation of CO molecules.

at ~ 6.21 $M_\odot$. In this range of enclosed masses the number fraction of carbon atoms, after the formation of CO, is highest; ranging between 2×10^{-1} and 8×10^{-9}. Figure 3.3 shows the number fraction of carbon and oxygen atoms in the expanding ejecta from the hydrodynamic results of Umeda and Nomoto (2002). The solid (blue) line indicates the number fraction of carbon left over after the formation of CO molecules. It should be noted for completeness that grain nucleation can occur at enclosed masses larger than we consider here, but is extremely inefficient due to low carbon number fractions, $\sim 10^{-14}$ and below.

For each mass subshell, our code starts by following the evolution of the density and temperature (see Figures 3.1 and 3.2, respectively, for examples) of the gas until the condition of supersaturation is satisfied. From that point on, at each time step the code performs three operations.

1. First, the code computes the number of critical clusters that are formed given the saturation, temperature, and partial pressure of the carbon atoms (according to

Eq. (3.2)).

2. Second, the code grows any pre-existing grain formed at earlier times according Eq. (3.4).

3. Finally, the code subtracts from the carbon in the gas phase the amount of carbon that has been locked in the solid phase by the processes in steps (1) and (2). The concentration of gas-phase carbon is evolved according to:

$$C_1(t_n) = C_1(t_{n-1}) - \frac{\Delta V_{grains,n}}{v_0 V_{shell,n}} - \frac{C_1(t_{n-1})}{\tilde{C}_1(t_n)} \left(\tilde{C}_1(t_{n-1}) - \tilde{C}_1(t_n) \right),$$

where $\Delta V_{grains,n}$ is the total change in volume of grains from the previous time step to the current time step. Then, the first term on the right-hand side is the concentration of gas-phase carbon from the previous time step, the second term is the change in the concentration of solid-phase carbon (it is a summation of all grain changes, including formation of new critical clusters and the growth of existing grains), and the final term accounts for the decrease in concentration of gas-phase carbon due to the expansion of the shell.

This process is repeated for each mass shell until the concentration of gas-phase carbon is reduced to 1 per cent of its original value. The dust distributions from all shells are then summed together to produce the final dust yield of each particular set (γ, c).

3.4 Results

3.4.1 Spherical Grains

After the supernova explosion, the hot gases expand and cool. The cooling allows the gases to reach supersaturation conditions. Once the supersaturation level becomes greater than unity, nucleation can occur. The supersaturation level continues to rise and the nucleation rate increases over time until depletion of available material becomes significant and the supersaturation level begins to drop, after which the nucleation rate falls off quickly. Eventually the gas is no longer supersaturated and nucleation ceases. However, grain growth is still possible.

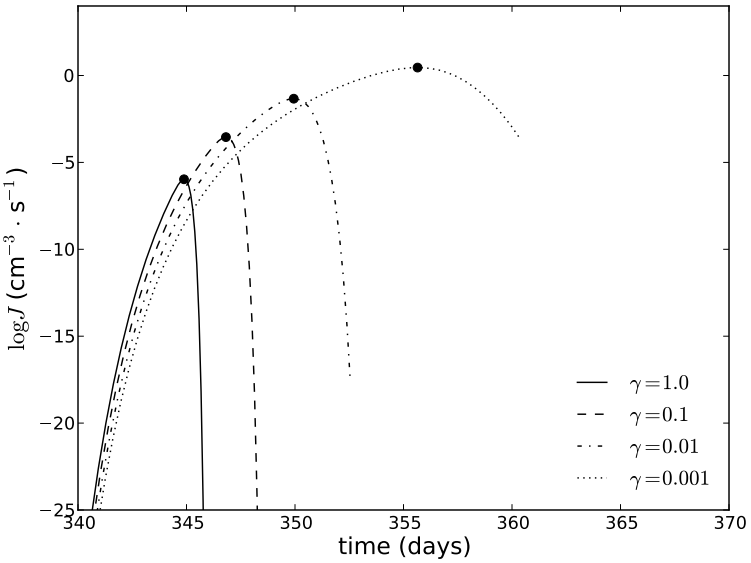

Figure 3.4: Nucleation rates for spherical grains ($c = (36\pi)^{1/3}$), for the four considered sticking coefficients of γ = 1.0, 0.1, 0.01, and 0.001. Filled circles indicate the time and rate of maximum nucleation. Rates are calculated at an enclosed mass coordinate $4.96 M_{\odot}$.

Figure 3.4 shows the nucleation rate for spherically shaped grains at enclosed mass coordinate 4.96 $M_{\odot}$ for the four sticking coefficients. We chose this particular enclosed mass shell because it contains the highest abundance of carbon atoms, after CO formation, of all our mass shells. The solid curve corresponds to $c = (36\pi)^{1/3}$ and γ = 1.0, the parameters generally used for nucleation studies. The dashed, dash-dot, and dotted curves correspond to γ = 0.1, 0.01, and 0.001, respectively. To be consistent with the works of Kozasa and Hasegawa (1987); Kozasa et al. (1989, 1991); Nozawa et al. (2003), we consider the time at which the nucleation rate is at its maximum to be the condensation time of the grains. We show these condensation times as filled circles at the maxima of the nucleation rates in the figure.

At early times, the reduced sticking coefficient makes the formation of critically sized grains more difficult and results in a suppressed nucleation rate. In the absence of strong nucleation, carbon atoms are not depleted from the gas and the saturation continues to increase. The reduced sticking coefficient thus causes the time at which nucleation is at its maximum to be delayed, and the nucleation to take place at higher saturation levels.

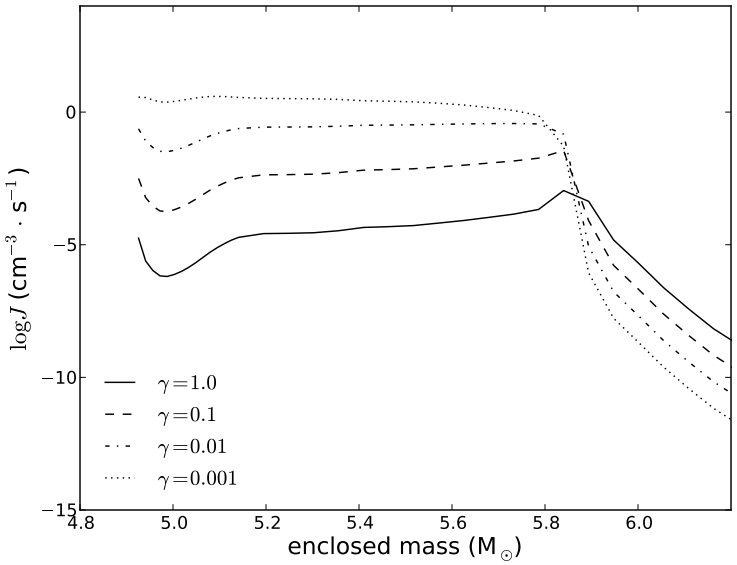

Figure 3.5: Maximum nucleation rates for spherical carbon grains at enclosed masses < 6.2 M$_\odot$ for four sticking coefficients.

As a consequence, a larger number of critical clusters can form with much smaller size (Eq. 3.3).

Figure 3.5 shows the maximum nucleation rates for spherical grains as a function of enclosed mass for our four sticking coefficients. For enclosed masses up to M$_r \sim 5.87$ M$_\odot$, the nucleation rate maxima for reduced sticking coefficients exhibit similar behaviour as in Figure 3.4. At greater enclosed masses, however, the behaviour is inverted and a reduced sticking coefficient results in depressed maximum nucleation rates. This difference in behaviour is due to the reduction in the number fraction of carbon available, from $\sim 10^{-2.5}$ to $\sim 10^{-5}$ (see Figure 3.3), which corresponds to a reduction in the concentration of carbon monomers. Since the nucleation rate (Eq. (3.2)) is proportional to the concentration of monomers squared, the drop in the carbon concentration consequently drops the nucleation rate. Thus, the nucleation rates do not peak as strongly (Figure 3.6), drawing out nucleation to later times for all sticking coefficients, so that a catastrophic reduction in the available material does not occur. Thus, the nucleation rates for reduced sticking coefficients remain depressed throughout the simulation time for higher enclosed mass shells.

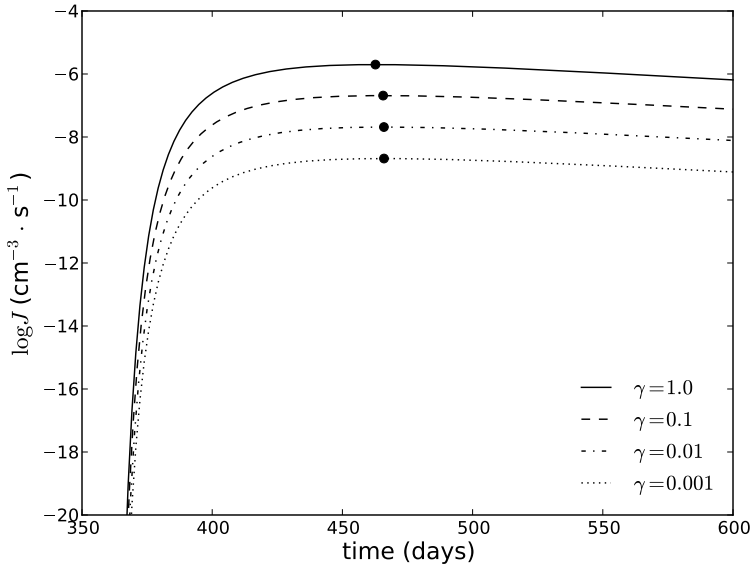

Figure 3.6: Nucleation rates for spherical carbon grains at an enclosed coordinate of 6.00 $M_\odot$ for four sticking coefficients. Condensation times are indicated by filled circles.

Figure 3.7 shows the condensation times corresponding to the maximum nucleation rates shown in Figure 3.5. The condensation times of the solid curve ($c = (36\pi)^{1/3}$, $\gamma = 1.0$) are in good agreement with the condensation times for carbon grains reported in Nozawa et al. (2003). Here the lower sticking coefficients result in delayed condensation times up to $M_r \sim 5.87\ M_\odot$, outside which the condensation time is only slightly delayed, or no longer delayed, when compared to the case of $\gamma = 1.0$. The more noticeably delayed condensation times, as well as the similarity of condensation times for all our sticking coefficients, at higher enclosed mass shells are also due to the drawn out nucleation process already discussed above.

Reducing the sticking coefficient makes both nucleation and grain growth more difficult. A reduced sticking coefficient results in a larger number of smaller grains, fewer larger grains, and a smaller maximum grain radius. In Figures 3.8 and 3.9, respectively, we show the size and mass distributions for spherical grains. For the case of $\gamma = 1.0$, the maximum grain size achieved is between 2 and 3 μm. When the sticking coefficient is reduced to 0.001, the maximum grain size is decreased to less than 0.01 μm.

Since the reduced sticking coefficient causes larger numbers of small grains to form,

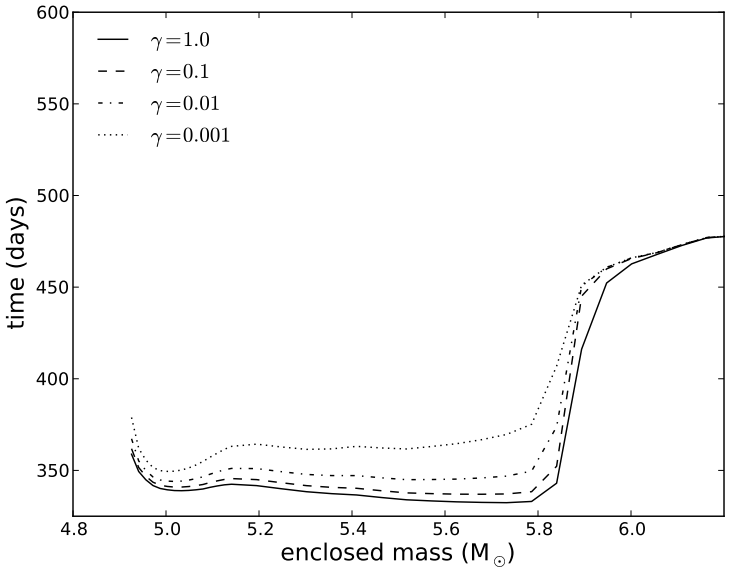

Figure 3.7: Condensation times of spherical carbon grain as a function of enclosed mass for four sticking coefficients.

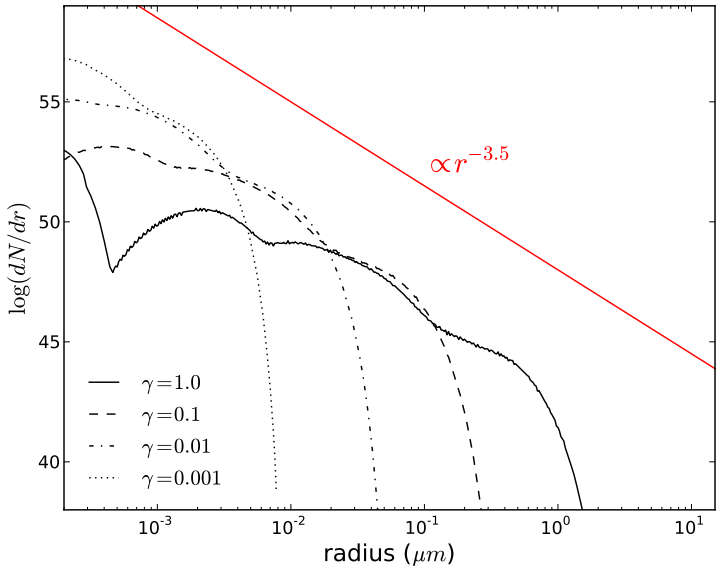

Figure 3.8: Size distribution of carbon grains for γ = 1.0, 0.1, 0.01, 0.001, with $c = (36\pi)^{1/3}$. For reference, the solid (red) line represents the power-law distribution with the form of $N_r \propto r^{-3.5}$, which has been suggested as that of interstellar grains (e.g., Mathis et al. (1977)).

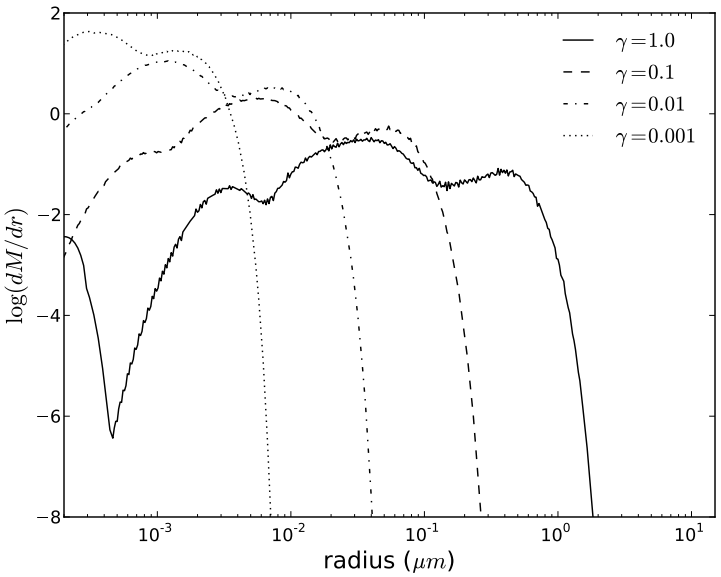

Figure 3.9: Mass distribution of carbon grains for γ = 1.0, 0.1, 0.01, 0.001, with $c = (36\pi)^{1/3}$.

the small grains contain more relative mass than the larger grains, as can be seein in Figure 3.9. However, the total mass of the grains is relatively robust. The total masses of dust grains for the spherical case are shown in Table 3.2, along with the aspherical cases which are discussed in the next section. Even though the onset of nucleation is delayed due to the reduced sticking coefficient at enclosed masses less than 5.87 $M_\odot$, where the majority of available carbon is contained, the subsequent grain growth consumes almost all of the carbon atoms for $\gamma > 0.001$. Thus, the total mass of carbon dust is principally determined by the mass of pre-existing carbon atoms.

3.4.2 Non-spherical Grains

We also calculated nucleation rates for aspherical grains. We choose a range of shape factors from $c = 5.4$ to $c = 12.0$. While $c = 6.0$ is the shape factor of a cube, each shape factor can correspond to a number of different grain shapes. The shape factor can be thought of as a deviation from the spherical case, the bigger the shape factor, the larger the deviation from a sphere and the larger the surface for a given volume.

In Figure 3.10 we show the nucleation rates for the same enclosed mass shell as shown

Table 3.2: Total mass of carbon grains formed

Mass (10^{-2} $M_\odot$)				
c	$\gamma = 1.0$	$\gamma = 0.1$	$\gamma = 0.01$	$\gamma = 0.001$
$(36\pi)^{1/3}$	4.95	4.93	4.89	4.79
5.4	4.94	4.91	4.87	4.75
6.0	4.92	4.89	4.84	4.70
7.0	4.89	4.86	4.79	4.62
9.0	4.82	4.76	4.65	4.34
12.0	4.64	4.52	4.27	3.32

in Figure 3.4, for increasing shape factors with $\gamma = 1.0$. Since the shape factor appears in the exponential term of the nucleation rate equation as $J_s \propto \exp(-c^3)$ (Eq. (3.2)), the higher shape factors reduce the nucleation rate. Therefore, the higher supersaturation levels at later times need to be attained so that the nucleation rate becomes high enough for significant depletion of the gas due to the growth of newly formed grains. However, the maximum nucleation rates for increasing shape factors are decreased. This is due to the fact that with a larger surface to volume ratio aspherical grains tend to grow faster, producing a sizeable depletion of the gas-phase carbon even for moderate nucleation rates. For all mass coordinates, increasing the shape factor leads to lower nucleation rates and delayed condensation times (Figures 3.11a and 3.12a, respectively).

In Figure 3.11b–d we show the nucleation rate maxima for all shape factors for each of the other three sticking coefficients. For any sticking coefficient, increasing the shape factor has the same effect of suppressing the nucleation rate. All condensation times, shown in Figure 3.12b–d, increase with the increased shape factor. Furthermore, for reduced sticking coefficients, greater shape factors lead to greater delays in the condensation time.

The shape factor $c = (36\pi)^{1/3}$ is the only shape factor that has just one associated shape, the sphere. The other shape factors we consider do not necessarily have a unique grain shape. To find a size distribution that is easily comparable to the spherical case, we define a *volume equivalent radius* for the aspherical grains as:

$$r_{\rm eff} = \left(\frac{3V}{4\pi}\right)^{1/3}, \tag{3.6}$$

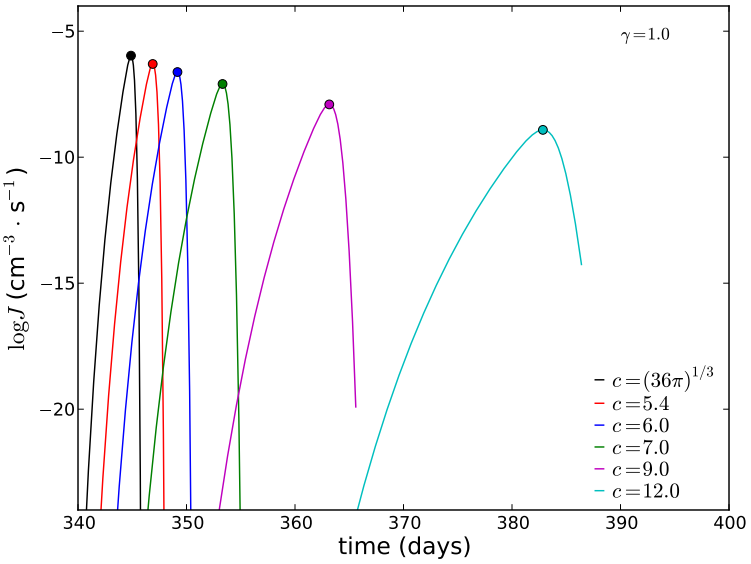

Figure 3.10: Nucleation rates as a function of time for six shape factors with $\gamma = 1.0$. Filled circles indicate maximum nucleation rate. Rates shown are for nucleation within a shell of enclosed mass of ~ 4.96 to ~ 4.97 $M_{\odot}$.

where V is the grain volume.

Figures 3.13a–d show the size distributions for all shape factors and sticking coefficients. As the shape factor is increased, the size and number of larger grains also increases. We find that the largest maximum grain radii are formed with $c = 12.0$ and $\gamma = 1.0$, and have a volume equivalent radius of almost 18 μm. On the other hand, the smallest maximum grain radii (~ 0.008 μm) are formed with $c = (36\pi)^{1/3}$ and $\gamma = 0.001$. As the sticking coefficient is reduced, the maximum grain radii for each shape factor are also reduced, and the number of smaller grains is increased. Even though there is a much larger number of small grains than large grains, the majority of the dust mass is contained within intermediate sized grains. In Figure 3.14a ($\gamma = 1.0$), most of the dust mass is contained in grains with volume equivalent radii between 0.01 and 0.5 μm.

The masses of carbon grains formed (Figures 3.14a–d) are dominated by the relatively small numbers of larger sized grains as the shape factor is increased. However, as the sticking coefficient is reduced (Figures 3.14b–d), even the masses of the grains formed with the largest shape factor become dominated by the smaller sized grains. The total mass of carbon grains formed for increased shape factors is given in Table 3.2 and shown

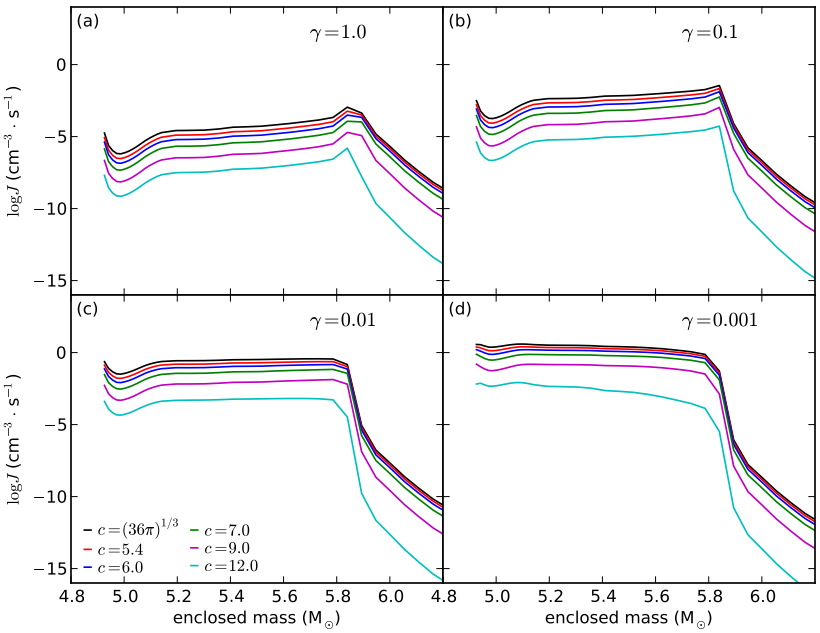

Figure 3.11: Maximum nucleation rates for all six shape factors and four sticking coefficients.

in Figure 3.15. Again, we notice that despite the difference in the size distribution due to different microphysical parameters, the total mass of dust that condenses is fairly robust (within a factor of 1.5) and constitutes almost the total amount of carbon that was left in the gas phase after the creation of CO molecules.

3.5 Discussion

We have shown that varying the microphysical properties of dust grains has important effects on the condensation times, nucleation rates, and size distributions of carbon dust grains from type II supernova explosions. However, the total mass of dust is only modestly affected by the changes in the grain properties. An inadequate choice of the shape or sticking coefficient is not therefore a viable explanation for the discrepancy between the mass of dust grains predicted in SN explosions and the observed dust mass in local type II SNe (see Section 3.1 for a more thorough discussion and references).

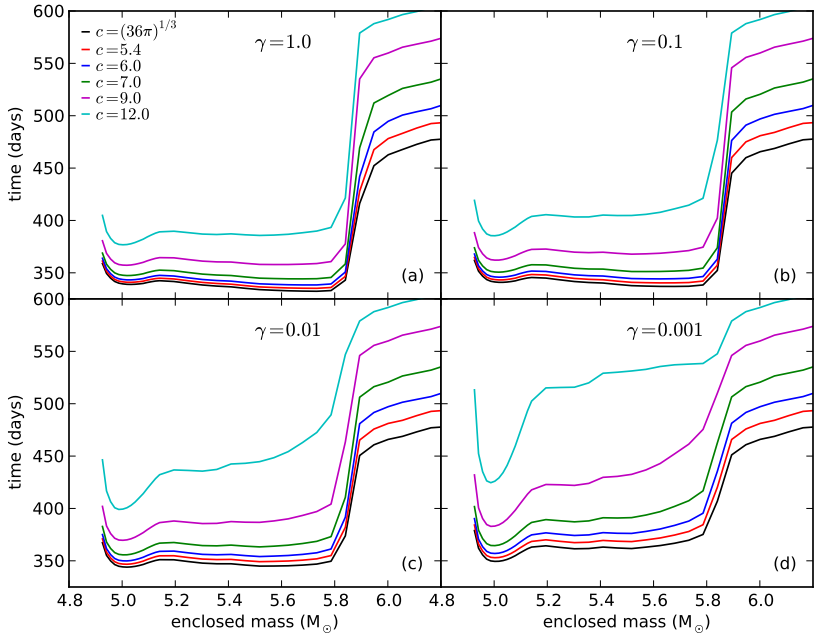

Figure 3.12: Dust condensation times for six shape factors and four sticking coefficients.

We find that a larger saturation is necessary to achieve efficient nucleation with either a small sticking coefficient ($\gamma < 1$) or for aspherical grains ($c > (36\pi)^{1/3}$). For that reason, all our simulations show that the condensation time grows when sticking coefficients less than unity or grain shapes that are different from spherical are adopted. However, differences can be found in the nucleation rates and final size distribution of the grains. Simulations with a low value of the sticking coefficient show a delayed nucleation but very high nucleation rates, thereby producing large quantities of small grains. This is due to the fact that low sticking coefficients inhibit both nucleation and grain growth and, therefore, all the carbon remains in the gas phase until a high saturation level is reached. At that point, many small grains are nucleated and the atomic carbon is quickly depleted. Bianchi and Schneider (2007) found similar effects when calculating dust nucleation with a sticking coefficient of $\gamma = 0.1$. Asphericity of the grains, on the other hand, inhibits nucleation but enhances grain growth. As a consequence, even if fewer grains are nucleated, they grow fast and the result is a grain size distribution characterized by less numerous, larger grains.

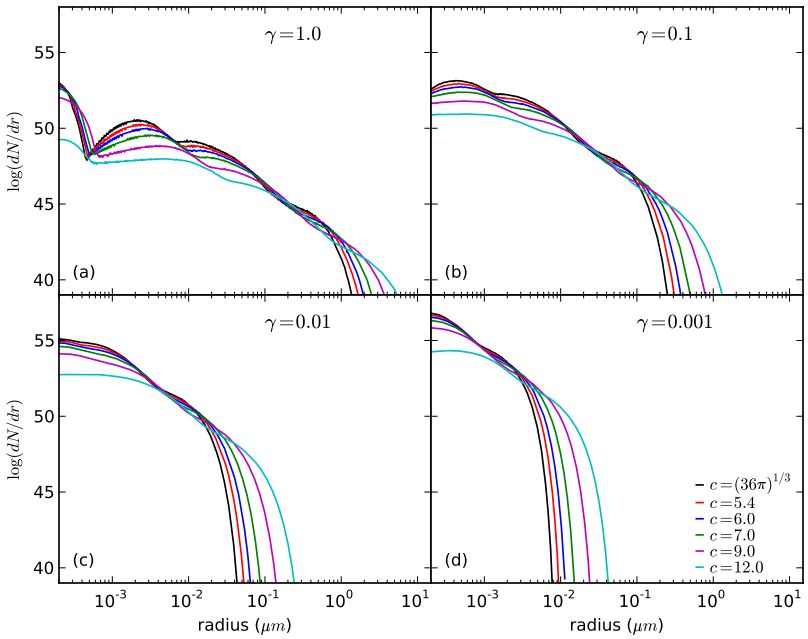

Figure 3.13: Size distribution of carbon grains for six shape factors and four sticking coefficients.

We find that the total mass of carbonaceous dust formed remains relatively stable even with sticking coefficients as low as 0.001. For the spherical case only, we explored the possibility of even smaller sticking coefficients, down to $\gamma = 10^{-9}$. We find that the mass of carbon dust formed becomes significantly reduced for sticking coefficients of $\gamma = 10^{-7}$ and below (see Figure 3.16). With sufficiently low values of sticking coefficient (below 10^{-8}) there is virtually no dust formation, but the required sticking coefficients seem unphysically low.

In terms of the observable properties of the SN-condensed dust, we find that the quantity that is most affected is the extinction curve (see Figure 3.17). Not surprisingly, simulations with small sticking coefficients (which, as explained above, produce large amounts of small grains), result in a very steep extinction curve at far-UV wavelengths, with R_V values between 3 and 3.5, shown in Figure 3.18. We make special note that the R_V values for $\gamma = 1.0$ are relatively high, even though the size distribution of the grains is consistent with that of interstellar grains (see Figure 3.8), because we account

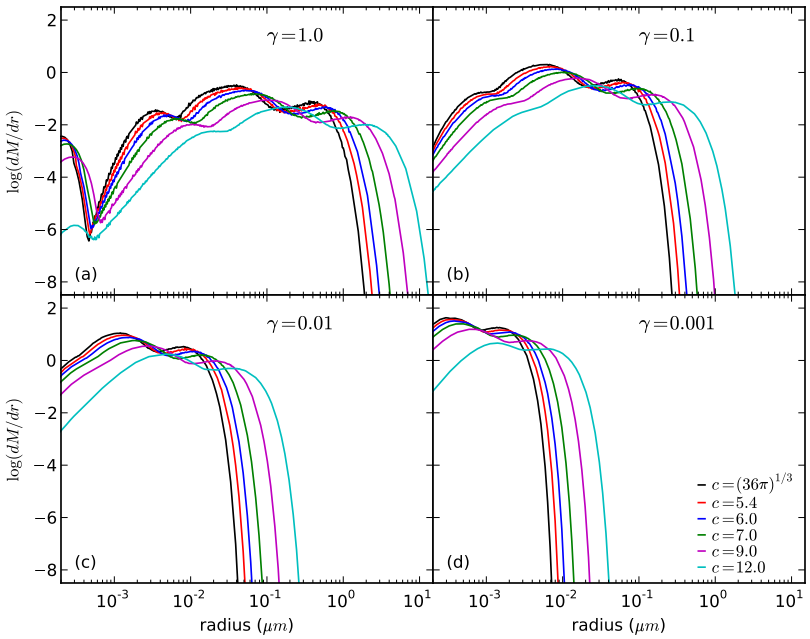

Figure 3.14: Mass distribution of carbon grain for six shape factors and four sticking coefficients.

for only carbon grains and that including other grains, such as silicates, could decrease the R_V values. On the other hand, simulations with very aspherical grains and relatively high sticking coefficients produce larger grains and, consequently, grey extinction curves. Without the knowledge of the values of the sticking coefficient and of the shape factor it is therefore impossible to predict the extinction curve of SN-condensed dust. This is a particularly worrying conclusion since the extinction curve is relatively easy to measure, even at high redshift, and could be used as an observational constraint for the origin of dust in the various environments. For example, Maiolino et al. (2004) compared the extinction curve measured in a quasar at $z = 6.2$ to the extinction curve calculated using the dust model by Todini and Ferrara (2001). They find that the data and the theoretical prediction are in good agreement and conclude that the dust observed in SDSSJ104845.05+463718.3 is indeed condensed in SN explosions (see also Stratta et al. (2007)). In light of our results, such conclusions need confirmation once a complete theory of SN dust nucleation is obtained.

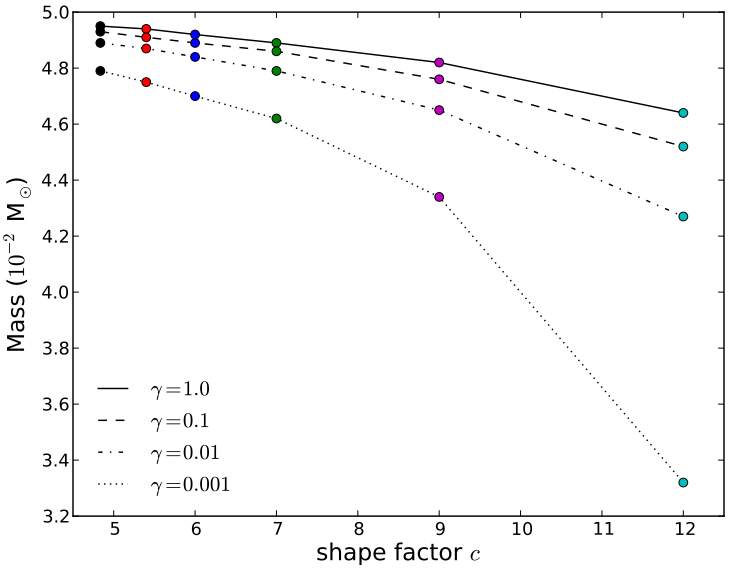

Figure 3.15: Total mass of carbon dust formed for all simulations.

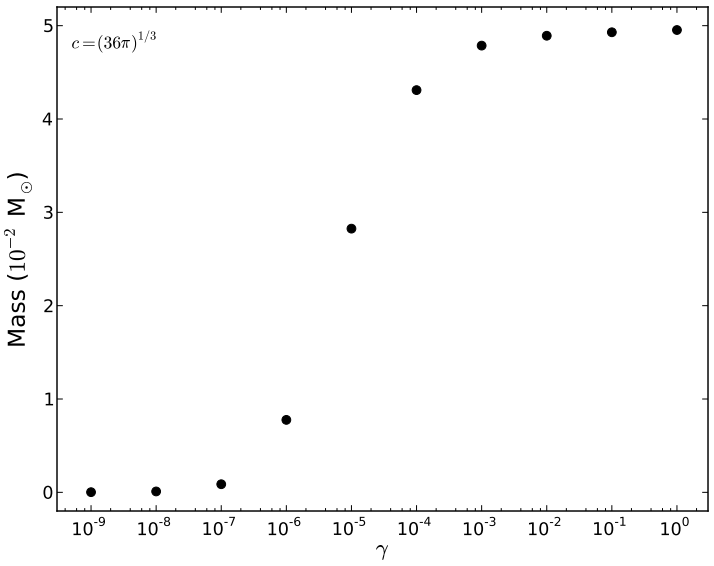

Figure 3.16: Total mass of dust formed for spherical carbonaceous grains with sticking coefficients down to $\gamma = 10^{-9}$.

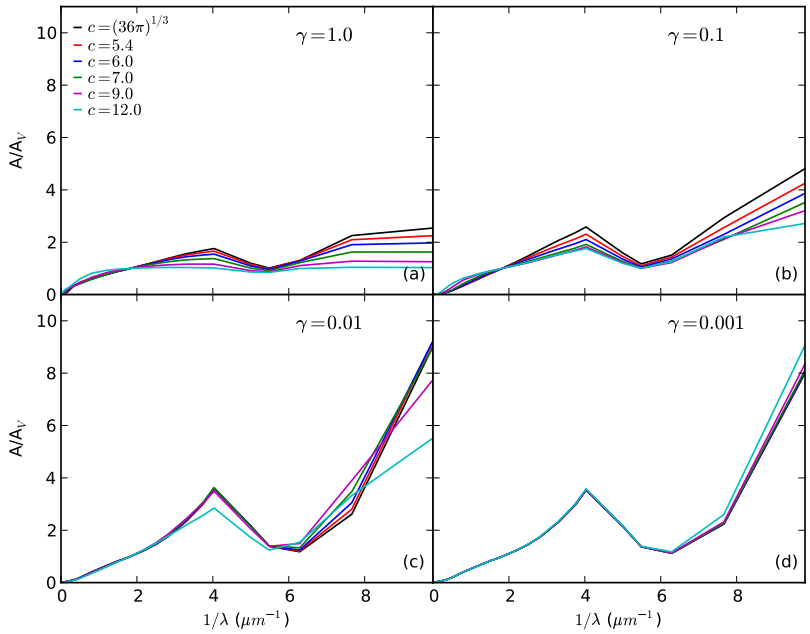

Figure 3.17: Extinction curves for each sticking coefficient and shape factor.

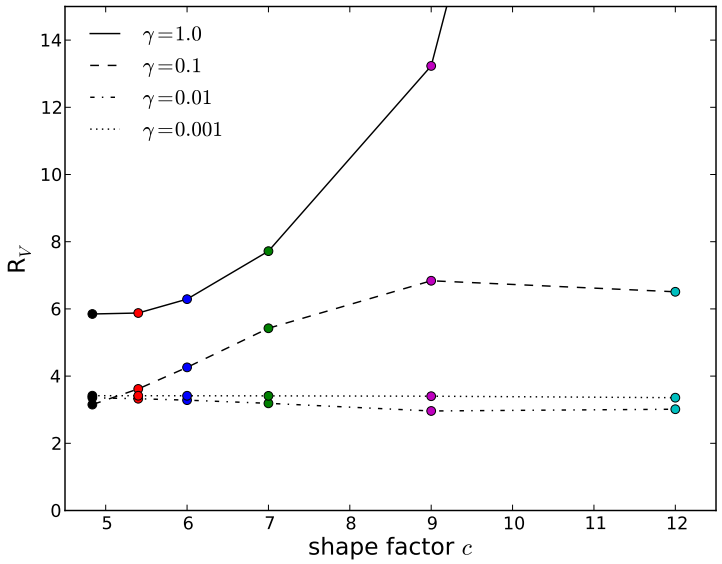

Figure 3.18: R_V values for 23 simulations. Not shown is $R_V = 41$ for $c = 12.0$ and $\gamma = 1.0$.

The dust that condenses, however, is not the dust that is ejected into the ISM. Dust produced in a CCSN has to travel through the reverse shock before being released into the ISM. The reverse shock can destroy most of the dust, in particular the smaller dust grains (Draine and Salpeter, 1979; Nozawa et al., 2007; Nath et al., 2008; Silvia et al., 2010). If astrophysical dust formation is indeed characterized by small values of the sticking coefficient, it is likely that the amount of dust formed is reduced significantly by the reverse shock. Conversely, increased shape factors allow for the formation of larger grains which would survive shock processing. The microphysical properties of dust grains can therefore affect the mass of dust that is injected in the interstellar medium, even though they affect only marginally the dust that is condensed during the early stages of the explosion.

Grain nucleation with non-spherical shapes may be more complicated than we considered here. We have assumed that the shape factors of the grains do not change as the grains grow. Since we assume here that grains grow by the addition of monomers, the shape of small clusters can change as monomers attach, in turn altering the shape factor. Another route to take could be to nucleate grains at an arbitrary shape factor and then allow the grains to grow into spheres. For example, one may turn grains into spheres when the number of monomers is larger than a given value. In this case, increased shape factors may not lead to such large grains as we show in our size distributions (Figure 3.13).

This work is purely a parametric study that aims to show that the microphysical properties of the grains are important, but not to point to any specific values of γ and c to be used in nucleation calculations. Therefore, we have chosen to neglect important factors that need be considered in a complete SN dust nucleation model. These include the choice of progenitor model, the presence of other dust species (see Nozawa et al. (2003)) as well as charged molecules that may interfere with carbonaceous dust condensation, and the destruction of CO molecules, due to photodissociation or collisons with fast electrons and charged particles (Petuchowski et al., 1989; Lepp et al., 1990; Liu et al., 1992; Clayton et al., 2001), that can inject additional carbon atoms into the available monomer concentration (see Todini and Ferrara (2001); Bianchi and Schneider (2007)).

A zero-metallicity 20 $M_{\odot}$ CCSN progenitor model was chosen because SNe at high redshift are expected to have zero metallicity. In general, the relative abundances of major elements in the He core are not significantly different among the SN models with different

metallicities. Thus, the species of dust formed do not depend on the metallicity of the SN progenitor star (Nozawa et al., 2010). Additionally, the gas density and temperature in the He core are almost independent of the progenitor mass and metallicity as long as the kinetic energy of the explosion is the same (Nozawa et al., 2003). Therefore, SN models with non-zero metallicities, or with different progenitor masses, are expected to show similar effects on carbon grains formation as we see here. This means that the mass of carbon dust formed in the SN ejecta is rather insensitive to changes in the sticking coefficient and shape factor and is purely determined by the mass of carbon atoms available for dust formation in the He layer. However, to confirm such expectations, additional progenitor models would need to be investigated.

Perhaps more important than the choice in progenitor model is the dissociation process of CO molecules. In this paper we assumed the formation of CO molecules to be complete and considered only the condensation process of C grains in the He layer where C/O $>$ 1. In the expanding ejecta, CO molecules could be destroyed through interactions with fast electrons from radioactively decaying ^{56}Co and charged particles such as He^+ and Ne^+ (Petuchowski et al., 1989; Lepp et al., 1990; Liu et al., 1992; Clayton et al., 1999; Kwong et al., 2000; Clayton et al., 2001; Deneault et al., 2006), allowing for more free carbon (and oxygen) atoms to be available for grain formation than we consider here. However, the number abundance of silicon atoms is too small for most of the enclosed mass regions (M= 4.93–6.21 $M_\odot$) in this work (see Figure 3.3), so that the formation of SiC and silicate gains cannot be expected. Therefore, the dissociation of CO molecules due to interactions with He^+ only results in a slight enhancement of the final mass of carbon grains and never changes our conclusion on the dependence of formation process of C grains on the microphysical properties.

On the other hand, Clayton et al. (1999) and Deneault et al. (2006) show that CO dissociation enables carbon dust grains to form even in O-rich layer where C/O $<$ 1. Given that the abundance of silicon atoms in the O-rich layer is higher than in the He layer, the formation of SiC grains could be expected there. However, as discussed in Nozawa et al. (2003), even if free carbon and silicon atoms coexist abundantly, the nucleation theory does not predict the formation of SiC grains. The formation process of large SiC grains as appeared in presolar grains, as well as formation efficiency of molecules is to be pursued in more sophisticated studies of dust formation. Furthermore, in the O-rich layer, the formation of silicate grains is also feasible. Bianchi and Schneider

(2007) show that the formation of silicate grains is more sensitive to changes in sticking coefficient than carbon grains, and the mass of silicate grains formed can be reduced for even $\gamma = 0.1$. The inclusion of silicate grains could affect the resulting extinction curves.

We have adopted the thermodynamic approach for this study because it involves the simplest nucleation equations, however, use of the kinetic theory of nucleation should be considered in the future. The kinetic theory still needs to take the sticking coefficient into account, but makes consideration of an evolving shape factor unnecessary, because the shape of the grain from a complex solid (for a few molecules) to a sphere (for $\sim$ 100 molecules) is intrinsically taken into account.

3.6 Acknowledgements

We would like to thank the reviewer for their insightful comments and suggestions for the improvement of this work. We would also like to thank Raffaella Schneider and Andrea Ferrara for their comments. Thanks go to the Institute for the Physics and Mathematics of the Universe (IPMU), University of Tokyo, Kashiwa, Japan, for their generous hospitality, and to the NSF East Asia and Pacific Summer Institute (EAPSI) Japan 2010 program (award #1015575) and the Japanese Society for Promotion of Science for their generous support. This work has also been supported in part by World Premier International Research Center Initiative, MEXT, Japan.

Chapter 4

Kinetic Nucleation of First Order Phase Transitions: Thermal Fluctuations and Small Grain Corrections

We consider the microphysical effect of the fluctuations of the cluster temperature during the nucleation of homogeneous first order phase transitions. We relax the assumption of thermal equilibrium and focus on the fluctuations of the internal energy of the clusters as a result of monomer attachments (heating), detachment (cooling), and collisions with an inert carrier gas. In addition, we consider the reduction of the monomer ejection rate from small clusters when the total internal energy is comparable to the detachment energy. We find that thermal fluctuations increase the ejection rates, decreasing the nucleation rate. On the other hand, small-grain corrections decrease the ejection rates, augmenting nucleation. The combined effect is that of increasing the nucleation rate, yielding water nucleation rates largely in excess of observations, especially at small saturation. We find, however, that our results are very sensitive to poorly known quantities such as the detachment energy of the smallest clusters.

4.1 Introduction

Nucleation is the first stage of a first-order phase transition, followed by growth and coagulation, and is characterized by the formation of stable nuclei due to size fluctuations from the attachment and detachment of monomers (Kashchiev, 2000; Vehkamäki, 2006). The size of the smallest stable nucleus is the so-called critical cluster size. Clusters smaller than the critical size tend to evaporate, while larger clusters tend to grow. The nucleation rate is then the number of these critical sized clusters that form in a unit volume in a unit time (Kashchiev, 2000)

The process of homogeneous nucleation is important in the formation of water droplets (Kashchiev, 2000), atmospheric aerosols (Kulmala, 2003), and cosmic dust (Kozasa and Hasegawa, 1987). Much of the previous theoretical work describing the nucleation process in general, and nearly all the work in astrophysical dust formation, focuses on the use of the classical nucleation theory (CNT) developed by Volmer and Weber (1926); Farkas (1927); Becker and Döring (1935); Frenkel (1939); Zeldovich (1943). CNT has seen some success in predicting nucleation rates in expansion chamber experiments (Wagner and Strey, 1981; Miller et al., 1983; Wölk and Strey, 2001; Manka et al., 2007), however, it has been noted that CNT does not accurately describe the temperature dependence of the nucleation rate tending to under-predict rates at lower temperatures and over-predict at higher temperatures (Adams et al., 1984; Wagner and R. Strey, 1984; Hung et al., 1989; Merikanto et al., 2004). Furthermore, CNT has been criticized for its inability to accurately predict nucleation rates for regularly shaped or nonpolar monomers (Dawson et al., 1969). This latter problem seems particularly telling of an underlying issue, since a spherical shape is assumed in CNT.

CNT describes nucleation through thermodynamic processes. Generally, CNT assumes that nucleation takes place under conditions of local thermodynamic equilibrium and employs the capillarity approximation, which amounts to assuming that all clusters, regardless of size, share the same surface tension value as the bulk material (Zeng and Oxtoby, 1991; McGraw and LaViolette, 1995; Oxtoby, 1998). The use of the capillarity approximation for large clusters works well, but is questionable for clusters containing fewer than $\sim$ 100 monomers (Burton, 1973). In the nucleation of a condensed phase from a vapor phase, CNT also assumes that critical nuclei are spherical, which again works well for large nuclei. However, in the formation of polycyclic aromatic hydrocarbons (PAHs) found in the atmosphere and in astrophysical environments clusters do not

form spherically (Tielens, 2005), suggesting that in this case at least, CNT is unable to accurately predict nucleation rates and critical cluster sizes.

The kinetic theory of nucleation developed by Becker and Döring (1935) is, however, applicable down to the smallest cluster sizes ($n \geq 2$) (Kashchiev, 2000). Furthermore, the kinetic theory allows for relaxing some of the assumptions used in CNT. Size dependent physical properties such as the cluster shape and sticking coefficient can be accounted for because attachment and detachment rates of monomers need to be calculated for each cluster size. Data of the dissociation energy of the cluster, when available, can also be included into the detachment rate calculations to reduce dependence on the capillarity approximation. Most importantly, the changes in cluster temperature due to attachment and detachment of monomers can be included into the detachment rate calculations.

We develop here a kinetic theory of nucleation employing cluster sublimation energies, temperature fluctuations of the cluster, and corrections to the cluster detachment rate based on an Einstein model of the cluster. This work is organized as follows. In Section 4.2 we present the modifications that we applied to the kinetic nucleation theory. Section 4.3 describes our Monte Carlo simulation procedure. Our results for the nucleation of water droplets are given for water droplets in Section 4.4 and for carbonaceous grains in Section 4.5. We discuss our results in Section 4.6 and our conclusions in Section 4.7.

4.2 Kinetic Nucleation Theory

The steady state nucleation rate in purely kinetic terms can be found as:

$$J_s = f_1 C_1 \left[1 + \sum_{n=2}^{M-1} \frac{g_2 g_3 \ldots g_n}{f_2 f_3 \ldots f_n} \right]^{-1} , \tag{4.1}$$

where f_n and g_n are the attachment and detachment rates, respectively, of a monomer to and from an n-sized cluster, C_1 is the concentration of monomers, and M is the maximum cluster size that needs to be considered (Kashchiev, 2000; Becker and Döring, 1935). For supersaturated conditions there exists a cluster size, n^*, where the attachment and detachment rates are equal. This so-called "*critical cluster*" is the n-sized cluster that satifies $f_n = g_n$. The terms in the summation of Eq. (4.1) quickly become negligible for clusters larger than the critical size, and it is sufficient to use $M \approx 2n^*$ (Kashchiev,

2000). We follow the work of Kashchiev (2000) for the development of expressions for f_n and g_n in purely kinetic terms.

4.2.1 Attachment and Detachment Rates

The rate of monomer attachment to an n-sized cluster f_n depends on the size and shape of the cluster, the density of monomers in the vapor, and the velocity of the monomers, and is given by:

$$f_n = \gamma c v_0^{2/3} \frac{S p_e}{(2\pi m_0 k T_{gas})^{1/2}} n^{2/3}\,, \tag{4.2}$$

where γ is the sticking coefficient of the cluster, $c \equiv \Sigma/V^{2/3}$ is the cluster's dimensionless shape factor with Σ and V being the cluster surface area and volume, respectively. v_0 and m_0 are the monomer volume and mass, S is the supersaturation level, p_e is the equilibrium vapor pressure, k is the Boltzmann constant, and T_{gas} is the temperature of the vapor (Kashchiev, 2000). The sticking coefficient γ is a size- and temperature-dependent quantity representing the probability that a monomer attaches to the cluster upon contact. Electric charging of the cluster, or the monomer, and the particular arrangement of bonds between monomers in the cluster can alter γ. In this work, however, we keep γ constant for all cluster sizes. Generally, γ is set to unity, but reducing γ has been shown to affect nucleation rates and the resulting cluster size distributions (Bianchi and Schneider, 2007; Fallest et al., 2011).

The rate of monomer detachment g_n depends on the properties of the cluster, rather than the surrounding vapor, and is more difficult to obtain. We invoke the principle of detailed balance and assume that the process of detachment is simply the reverse of the process of attachment to find an expression for the detachment rate. For an n-sized cluster,

$$g_n = f_{n-1} \frac{C(n-1)}{C(n)}\,, \tag{4.3}$$

where $C(n)$ is the distribution of n-sized clusters (Kashchiev, 2000). We can relate the distribution of n-sized clusters to the monomer concentration through

$$C(n) = C_1 \exp\left(\frac{-(W(n) - W_1)}{kT}\right), \tag{4.4}$$

where $W(n)$ is the work to form the n-sized cluster and W_1 is the work to form a monomer

(Kashchiev, 2000). The work to form an n-sized cluster can be found by:

$$W(n) = -n\Delta\mu + \Phi(n)\,, \tag{4.5}$$

where $\Delta\mu = kT \ln S$ is the difference in chemical potential between monomers in the vapor and in the cluster, $\Phi(n)$ is the effective excess cluster energy:

$$\Phi(n) = \lambda n - E_n\,, \tag{4.6}$$

and λ is the sublimation energy per molecule and E_n is the cluster binding energy (Kashchiev, 2000) Substituting Eqs. (4.2) and (4.4)–(4.6) into Eq. (4.3) we obtain:

$$\begin{aligned} g_n \quad &= \gamma c v_0^{2/3} \tfrac{p_e}{(2\pi m_0 k T_{gas})^{1/2}} (n-1)^{2/3} \\ &\quad \times \exp\left\{ \tfrac{\lambda - E_n + E_{n-1}}{k T_{gas}} \right\}. \end{aligned} \tag{4.7}$$

The basic detachment rate in Eq. (4.7) can be used to find the detachment rate through quantities that can be either found experimentally or set in simulations, without relying on thermodynamics processes. For comparison, the unmodified detachment rate found using the capillary approximation is:

$$\begin{aligned} g_{n,\mathrm{unmod}} \quad &= \gamma c v_0^{2/3} \tfrac{p_e}{(2\pi m_0 k T_{gas})^{1/2}} (n-1)^{2/3} \\ &\quad \times \exp\left\{ \tfrac{2\sigma v_m}{r k T_{gas}} \right\}, \end{aligned} \tag{4.8}$$

where r is the radius of the n-sized cluster.

4.2.2 Temperature Fluctuations

When considering nucleation of clusters that are in local thermodynamic equilibrium, Eqs. (4.2) and (4.7) may be used as written. However, clusters are rarely in thermodynamic equilibrium with the surrounding vapor due to attachment and detachment of monomers, as well as interactions with other particles such as carrier gas atoms or molecules and radiative heating and cooling. In this work, we consider only changes to the cluster internal energy due to the attachment and detachment of monomers and collisions with carrier gas atoms. The attachment of a monomer adds energy to the cluster,

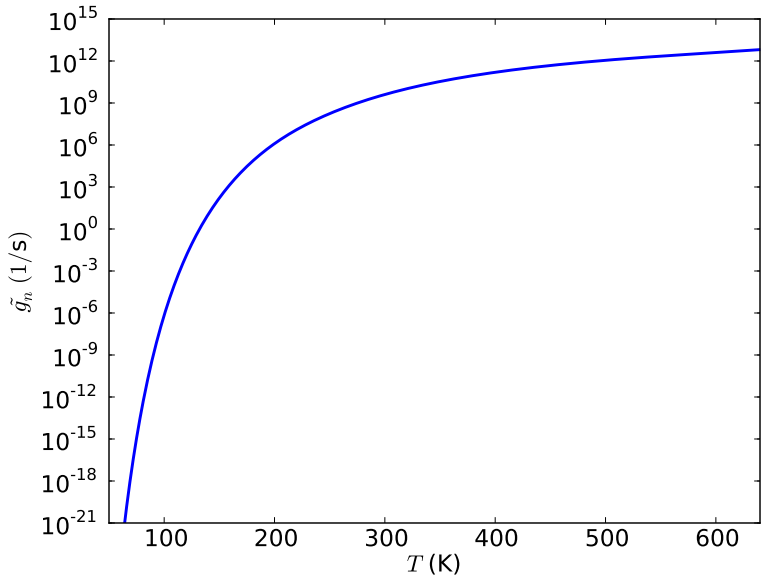

Figure 4.1: Detachment rate $\tilde{g_n}$ (Eq. (4.9) vs. cluster temperature for an $n = 100$ water cluster.

whereas the detachment of a monomer removes energy. Carrier gas atoms or molecules bounce off the cluster causing either energy gains or losses depending on the relative energies of the carrier gas particles and the cluster. Changes in the cluster internal energy appear as fluctuations in the cluster temperature (McGraw and LaViolette, 1995; Keith and Lazzati, 2011).

Since the attachment rate depends on the cluster size and the conditions in the surrounding vapor, changes in the cluster temperature do not affect the rate of monomer attachment. Conversely, the detachment rate depends sensitively on the cluster temperature. So, we modify Eq. (4.7) slightly:

$$\begin{aligned} \tilde{g_n} &= \gamma c v_0^{2/3} \frac{p_e(T_{cluster})}{(2\pi m_0 k T_{cluster})^{1/2}} (n-1)^{2/3} \\ &\quad \times \exp\left\{ \frac{\lambda - E_n + E_{n-1}}{k T_{cluster}} \right\}, \end{aligned} \tag{4.9}$$

to account for the cluster temperatures, $T_{cluster}$, and the corresponding vapor equilibrium pressure. Figure 4.1 shows example detachment rates calculated from Eq. (4.9) for an $n = 100$ water cluster for the temperature range investigated in this work. A reduction

in the cluster temperature results in a reduction in the detachment rate.

For small clusters, the change in internal energy due to the attachment or detachment of a monomer represents a large fraction of the internal energy of the cluster, and thus small clusters experience large temperature fluctuations. These temperature fluctuations can be extreme enough that a drop in temperature can result in a cluster being too cold to detach a monomer. In this way, clusters that are smaller than the critical size can grow though subsequent monomer attachments rather than evaporate as would be expected. Large clusters, conversely, experience smaller temperature fluctuations as the internal energy changes are less dramatic. An interaction of a carrier gas atom with the cluster can be thought of as the attachment and immediate detachment of the carrier gas atom. In this way, a carrier gas atom that is more energetic than the cluster gives energy to the cluster, while a carrier gas atom that is less energetic removes energy from the cluster. These interactions tend to stabilize the cluster temperature at the temperature of the surrounding vapor (McGraw and LaViolette, 1995).

4.2.3 Cluster Temperature

To find the cluster temperature we use available empirical data of the specific heat for the nucleation material to determine the internal energy of a monomer as a function of temperature, $U_1(T)$. Following Guhathakurta and Draine (1989), we assume that the internal energy of the cluster is distributed among its vibrational degrees of freedom. An n-sized cluster has $3n$ degrees of freedom and $f = 3n - 6$ vibrational degrees of freedom ($f = 3n - 5$, for $n = 2$). We then find the internal energy of the n-sized cluster:

$$U_n(T_{cluster}) = \frac{3n-6}{3n} n U_1(T_{cluster}) = (n-2) U_1(T_{cluster}) \,, \tag{4.10}$$

or, for the dimer ($n = 2$):

$$U_2(T_{cluster}) = \frac{1}{3} U_1(T_{cluster}) \,. \tag{4.11}$$

The cluster temperature after monomer attachment or detachment, and after a collision with a carrier gas atom can be found using Eqs. (4.10) and (4.11) and conservation of energy considerations.

Monomer Attachment

To determine the cluster temperature after a monomer attachment we consider the interaction:

$$X_n + X_1 = X_{n+1}\,, \tag{4.12}$$

where X_n is an n-sized cluster of material X and X_1 is the monomer. The conservation of energy equation for this reaction is then:

$$U_n - E_n + K_{in}(T_{gas}) = U_{n+1} - E_{n+1}\,, \tag{4.13}$$

where U_n and U_{n+1} are the cluster energies before and after the attachment, respectively, given by Eq. (4.10), E_n and E_{n+1} are the clusters' binding energies, and $K_{in}(T_{gas})$ is the kinetic energy of the attaching monomer. The kinetic energy of the attaching monomer is determined by a Boltzmann distribution at the temperature of the surrounding vapor. We can then find the energy per monomer in the $(n+1)$-cluster after the attachment through:

$$U_1(T_{after}) = \frac{U_n(T_{before}) - E_n + E_{n+1} + K_{in}(T_{gas})}{n-1}\,. \tag{4.14}$$

Monomer Detachment

The interaction for the detachment of a monomer is:

$$X_n = X_{n-1} + X_1\,, \tag{4.15}$$

with conversation of energy equation:

$$U_n - E_n = U_{n-1} - E_{n-1} + K_{out}\,. \tag{4.16}$$

From this conservation of energy equation, the energy per monomer in the $(n-1)$-cluster is then found by

$$U_1(T_{after}) = \frac{U_n(T_{before}) - E_n + E_{n-1} - K_{out}}{n-3}\,, \tag{4.17}$$

or for a trimer becoming a dimer:

$$U_1(T_{after}) = 3(U_3(T_{before}) - E_3 + E_2 - K_{out})\,. \tag{4.18}$$

To find the cluster temperature after a monomer detachment the kinetic energy given to the detached monomer, K_{out}, needs to be determined. Following Guhathakurta and Draine (1989) again, we apply Rice-Ramsperger-Kassel (RRK) theory for an "Einstein model" of the cluster (Robinson and Holbrook, 1972). RRK theory assumes that the energy in the cluster is distributed throughout the cluster's vibrational degrees of freedom. From the Einstein model, we assume that these degrees of freedom act as harmonic oscillators with a common frequency ω_0, and energy $\hbar\omega_0 = 0.75kT_{Debye}$, where T_{Debye} is the Debye temperature of the material. As in Guhathakurta and Draine (1989), we use the definitions $m \equiv U_n/\hbar\omega_0$ as the total number of energy quanta available in the cluster, and $b \equiv B_n/\hbar\omega_0$ as the number of energy quanta needed to free a monomer from the cluster, where B_n is the sublimation energy per particle of an n-sized cluster, that we take to be the difference in binding energies between n-sized and $(n-1)$-sized clusters:

$$B_n = E_n - E_{n-1}\,. \tag{4.19}$$

For a monomer to detach from the cluster, enough energy must be concentrated into one particular degree of freedom to overcome the sublimation energy for the monomer. We assume that any energy in excess of B_n becomes the monomer's kinetic energy.

To find the kinetic energy we consider the probability that i energy quanta are contained in a particular degree of freedom (Guhathakurta and Draine, 1989):

$$p_f(i) = \frac{C_{f-1}(m-i)}{C_f(m)}\,, \tag{4.20}$$

where $C_f(m)$ is the number of ways the m energy quanta can be distributed among all vibrational degrees of freedom (Guhathakurta and Draine, 1989):

$$C_f(m) = \frac{(m+f-1)!}{m!(f-1)!}\,. \tag{4.21}$$

Substitution of Eq. (4.21) into Eq. (4.20) yields:

$$p_f(i) = \frac{(m-i+f-2)!m!(f-1)!}{(m-i)!(f-2)!(m+f-1)!}\,. \tag{4.22}$$

From Eq. (4.22) we calculate each probability that a particular degree of freedom contains from $i = b$ to $i = m$ energy quanta. During our simulations (discussed in section 4.3)

when a monomer detaches from the cluster we choose the energy quanta i used to break the monomer free and set

$$K_{out} = (i - b)\hbar\omega_0 \,, \tag{4.23}$$

to determine the kinetic energy of the ejected monomer. The energy carried away by the monomer can be a substantial fraction of the available energy, especially for small clusters where there are relatively few degrees of freedom into which the energy quanta are distributed. In this event, the energy remaining in the $(n-1)$-sized cluster could be too little to allow for another monomer detachment, causing g_{n-1} to be considerably smaller than otherwise expected by Eq. (4.7). Thus, the thermal history of the clusters is important to know because clusters of the same size have different temperatures and, consequently, different detachment rates.

Carrier Gas Collision

To find the cluster temperature after a collision with a carrier atom, we simply consider the kinetic energy of the carrier gas atom, K_{cg} before and after the collision as in the interaction:

$$X_n + K_{cg,i} = X_n + K_{cg,f} \,. \tag{4.24}$$

We assume this collision occurs so that the atom's kinetic energy before the collision is determined by the temperature of the surrounding vapor, $K_{cg,i} = K_{cg}(T_{gas})$, and its kinetic energy after the collision is determined by the temperature of the cluster before the collision, $K_{cg,f} = K_{cg}(T_{cluster})$. The kinetic energies of the carrier gas atom are determined through a Boltzmann distribution of energies at the temperatures of the surrounding vapor and of the cluster. From conservation of energy for this interaction we have:

$$U_{n,i} - E_n + K_{cg}(T_{gas}) = U_{n,f} - E_n + K_{cg}(T_{cluster}) \,. \tag{4.25}$$

Clearly, the change in the cluster's internal energy is then equal to the change in the carrier gas atom's kinetic energy ΔK_{cg}, but opposite in sign, where

$$\Delta K_{cg} = K_{cg}(T_{cluster}) - K_{cg}(T_{gas}) \,. \tag{4.26}$$

We find the energy per monomer in the cluster after this collision from Eqs. (4.25) and (4.26):

$$U_1(T_{after}) = \frac{(n-2)U_1(T_{before}) - \Delta K_{cg}}{n-2}\,, \tag{4.27}$$

and in the case of a collision with a dimer:

$$U_1(T_{after}) = U_1(T_{before}) - 3(\Delta K_{cg})\,. \tag{4.28}$$

Determining the cluster temperature $T_{cluster}$ from the energy per monomer $U_1(T_{after})$ is accomplished through the data of the material's specific heat as a function of temperature used previously, and the detachment rates in Eq. (4.9) can be calculated.

4.2.4 Detachment Rate Corrections for Small Clusters

As shown above, for a monomer to detach from the cluster, enough energy needs to be concentrated in a particular degree of freedom. However, it is possible that even when the total internal energy within the cluster is sufficient to overcome the sublimation energy, a monomer does not detach. Therefore, the detachment rate needs to be reduced accordingly. Following Guhathakurta and Draine (1989), the probability that a particular degree of freedom contains at least b energy quanta is given by:

$$p_f(b) = \sum_{i=b}^{m} p_f(i)\,, \tag{4.29}$$

where $p_f(i)$ is given in Eq. (4.22). When surrounded by a heat bath, the detachment rate of the n-sized cluster is reduced by a factor:

$$S_n(T_{cluster}) = \left(\frac{1+\gamma_f}{\gamma_f}\right)^b \frac{(\gamma_f f)!(\gamma_f f - b + f - 1)!}{(\gamma_f f + f - 1)!(\gamma_f f - b)!}\,, \tag{4.30}$$

where $\gamma_f = m/f$ is the mean energy quanta per degree of freedom. We then modify the detachment rate by this probability so that

$$g_n^* = S_n(T_{cluster})\tilde{g_n}\,. \tag{4.31}$$

Table 4.1: Physical properties of H_2O water.

molecule mass (g)	critical temperature (K)	Debye temperature (K)
2.99×10^{-23}	647.15	192.0

4.2.5 Nucleation Rate

To account for the different detachment rates due to the thermal histories of the clusters, we calculate an average detachment rate $\bar{g_n^*}$. The average detachment rate is calculated by following an n-sized cluster through a series of temperature fluctuations due to monomer attachment and detachment, and carrier gas collision events, all the while maintaining the cluster at size n. We then calculate the steady nucleation rate through

$$J_s = f_1 C_1 \left[1 + \sum_{n=2}^{M-1} \frac{\bar{g_2^*}\bar{g_3^*}...\bar{g_n^*}}{f_2 f_3 ... f_n} \right]^{-1} . \tag{4.32}$$

4.3 Simulations

We concentrate on the nucleation of water droplets in the presence of an argon carrier gas. During each simulation we assume that the water vapor and carrier gas are in thermal equilibrium. Following the work of Wölk and Strey (2001), we consider nucleation at five different temperatures: $T = 220, 230, 240, 250$, and 260 K, and at supersaturation levels, S, ranging from 6 to 30. We also consider only the formation of spherical droplets with complete adhesion of monomers, so that the shape factor and sticking coefficient are $c = (36\pi)^{1/3}$ and $\gamma = 1.0$, respectively. Table 4.1 lists the relevant physical properties of water used in this work.

For each cluster size we begin by calculating the monomer attachment rate (Eq. (4.2)), finding the vapor equilibrium pressure through:

$$\begin{aligned} p_e \quad &= \exp\left(77.34491 - 7235.42465/T \right. \\ &\quad \left. -8.2 \ln T + 0.0057113T\right) \end{aligned} \tag{4.33}$$

(see Wölk and Strey (2001) and references therein). To calculate the carrier gas interaction rate, we assume that collisions occur in an analogous manner to monomer

Table 4.2: Temperature T and corresponding water vapor fractions ω.

T(K)	260.0	250.0	240.0	230.0	220.0
ω	0.02633	0.01669	0.00681	0.00338	0.00162

attachment:

$$f_{n,\mathrm{Ar}} = \gamma c v_0^{2/3} \frac{p_{\mathrm{Ar}}}{(2\pi m_{\mathrm{Ar}} k T_{gas})^{1/2}} n^{2/3}\,, \tag{4.34}$$

where m_{Ar} is the mass of an argon atom and p_{Ar} is the argon carrier gas partial pressure found through

$$p_{\mathrm{Ar}} = S p_e \left(\frac{1}{\omega} - 1\right)\,, \tag{4.35}$$

ω is the vapor fraction (Wölk and Strey, 2001). We hold ω constant for all simulations of a given temperature. Table 4.2 lists the water vapor and argon carrier gas temperatures and vapor fractions we consider in this work.

4.3.1 Monomer Sublimation Energies

The detachment rate depends sensitively on the difference in binding energies of the n-sized and $(n-1)$-sized clusters, or equivalently on the sublimation energy B_n. Available experimental data of the binding or sublimation energies of small water clusters is rather sparse and theoretically calculated values are only found for clusters $n \lesssim 60$. Due to the paucity of data available, in this work we find the sublimation energy through Eq. (4.19) with

$$E_n = \lambda n - c v_0^{2/3} \sigma n^{2/3}\,, \tag{4.36}$$

where σ is the surface tension (Kashchiev, 2000). We take $E_1 = 0$. Since the surface tension is dependent on temperature, for each cluster size a range of binding energies is found. We also use the binding energies per monomer calculated and estimated through B3LYP methods by Lenz and Ojamäe (2009) for clusters up to $n = 60$ as an illustration of the sensitivity of the nucleation rates on these energies. Figure 4.2 shows the sublimation energies calculated from Eq. (4.19) (shaded grey region) and the data of Shank et al. (2009) (red filled square), Wang and Bowman (2011) (black filled square) and Lenz and Ojamäe (2009) (blue filled circles) and the horizontal, dashed line indicates the bulk sublimation energy for water of 7.76×10^{-13} ergs. Calculations using the data of Lenz

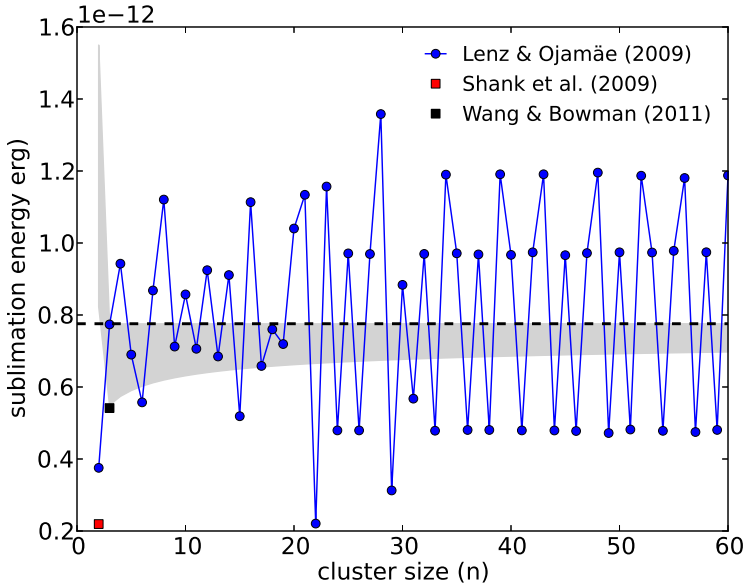

Figure 4.2: Sublimation energies for water clusters calculated from Eq. (4.19) (shaded grey region), the data of Lenz and Ojamäe (2009) (blue, filled circles), Shank et al. (2009) (red, filled square), and Wang and Bowman (2011) (black, filled square). The blue connecting lines between the Lenz & Ojamäe data points are a guide for the eye. The horizontal, dashed line indicates the bulk sublimation energy of water of 7.76×10^{-13} ergs.

and Ojamäe (2009) result in sublimation energies that are often higher than the bulk sublimation value. The simulations in this work generally use binding energies found through Eq. (4.36), but we include an example simulations using the data of Shank et al. (2009) and Wang and Bowman (2011), as well as Lenz and Ojamäe (2009).

4.3.2 Breaking Dimers and Trimers

Using our model as described above, a monomer cannot detach from the dimer or trimer clusters. Figure 4.3 shows calculations for the energy quanta available in the cluster m and the energy necessary for monomer detachment (sublimation quanta) b, as calculated using the data of Lenz and Ojamäe (2009), in the temperature range from 0 to 645 K for both the dimer and the trimer clusters. In calculating m we use the specific heats from Fukusako (1990) (and references therein) and internal energies for liquid water tabulated in Lemmon et al. (2005). When b is calculated from Eq. (4.19) using either the binding

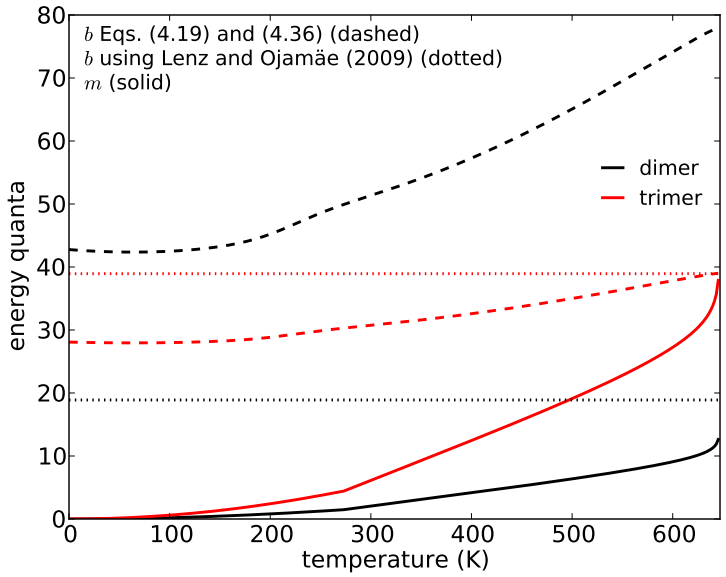

Figure 4.3: Curves of $b = B_n/\hbar\omega_0$ and $m = U_n/\hbar\omega_0$ for the dimer ($n = 2$) and trimer ($n = 3$) clusters. Sublimation curves are found using Eqs. (4.19) and (4.36) (dashed) and from the data of Lenz and Ojamäe (2009) (dotted).

energies of Lenz and Ojamäe (2009) or from Eq. (4.36), the available energy does not surpass the sublimation energy, causing our dimer and trimer to be unbreakable.

The water-dimer mole fraction is estimated to be < 0.007 (Eisenberg and Kauzmann, 1969; Lenz and Ojamäe, 2009; Slanina et al., 1992) suggesting that dimers should readily dissociate into monomers. Additionally, the trimer, tetramer, and pentamer mole fractions are also expected to be < 0.001 (Lenz and Ojamäe, 2009) This indicates that monomers are the dominant cluster size and that dimers and trimers should break apart. Therefore, in our model we assume a detachment event occurs if the cluster temperature reaches the critical temperature of water (645.23 K (Kulmala, 2003)). We note that if the sublimation energies of Shank et al. (2009) and Wang and Bowman (2011) are used instead, m crosses b at 637.7 K and 600.1 K for the dimer and trimer, respectively, and the cluster will have sufficient energy to eject a monomer. However, the temperatures at which m crosses b are high enough that the cluster temperature increases due to collisions cause the cluster to break because it has reached the critical temperature, rather than because m has increased over b.

4.3.3 Simulation Procedure

Keeping the vapor temperature constant, the monomer attachment rate and carrier gas collision rate also remain constant for a given cluster size throughout a given simulation. However, for each code cycle we need to calculate the detachment rate due to the temperature fluctuations of the cluster. We set the initial cluster temperature equal to the vapor temperature. Then for each code cycle we:

i) calculate the cluster sublimation energy B_n using Eqs. (4.19) and (4.36), based on the cluster temperature. Alternatively, we can use the sublimation energies calculated from available binding energy data.

ii) calculate m and b and the small grain correction as in Eq. (4.30)

iii) calculate the detachment rate (Eq. (4.31))

iv) use Monte Carlo techniques to determine the interaction which occurs

v) find the new energy per monomer from the corresponding conservation of energy equation

vi) find the new cluster temperature

The procedure is repeated until the cluster has undergone 2000 detachment events. We use the time taken for the cluster to undergo the last 1000 detachment events to calculate the average detachment rate $\bar{g_n^*}$.

We repeat the process for each cluster size. For cluster sizes from $n = 2$ to $n = 70$, we calculate the attachment and detachment for each size. For clusters larger than $n = 70$, we use the radius of the 70-mer cluster, increment it by the effective radius of a water molecule, find the volume of the new cluster, and calculate the number of monomers required to fill the volume. We determine the critical cluster size by comparing the attachment rate to the average detachment rate for each cluster size. The cluster for which these rates are equal we define as our critical cluster. We then find the nucleation rate from Eq. (4.32).

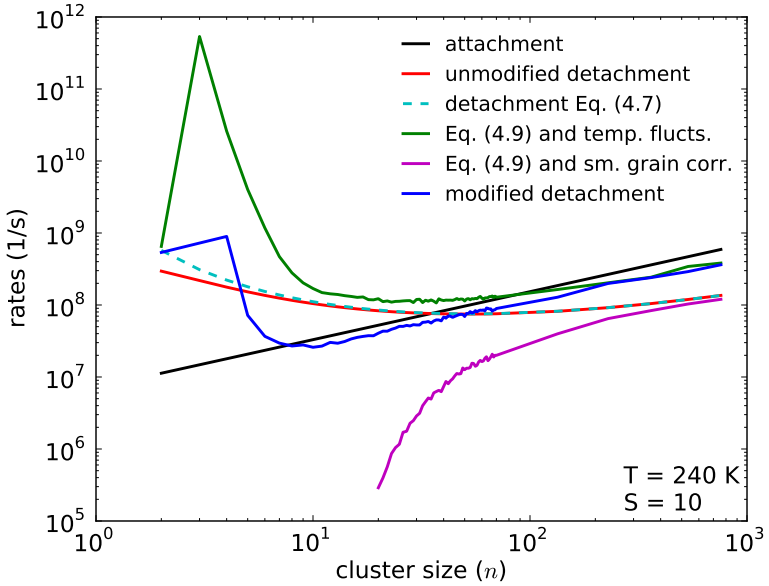

Figure 4.4: Attachment, unmodified detachment and the basic detachment rates from Eq. (4.7) (dashed cyan), with temperature fluctuations (Eq. (4.9) in green), Eq. (4.7) with corrections for small grain sizes (magenta), and all modifications included, Eq. (4.31) (blue), for water droplets in a surrounding vapor at $T = 240$ K and $S = 10$.

4.4 Water droplets

4.4.1 Attachment and detachment rates

In Figure 4.4 we show the attachment rate (Eq. (4.2), shown in black), the unmodified detachment rate (Eq. (4.8), shown in red), the basic detachment rate from Eq. (4.7) (dashed cyan) with temperature fluctuations from Eq. (4.9) (green), Eq. (4.7) with the rate correction for small clusters (magenta), and the modified detachment rate with all modifications included (Eq. (4.9) shown in blue). The temperature fluctuations increase the rate of monomer detachment for all cluster sizes when compared to the unmodified detachment rate. This also causes the critical cluster to be bigger than expected by the unmodified theory. The rate correction for small clusters, on the other hand, helps stabilize all clusters shown. These two effects compete with each other and result in the modified detachment rate shown in blue. For the smallest cluster sizes ($n \lesssim 7$), the temperature fluctuations dominate and the clusters are unstable. For larger clusters, the

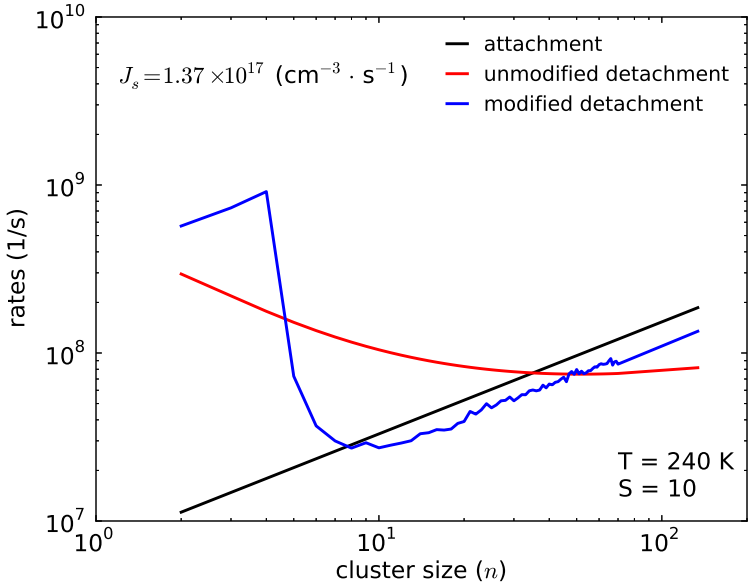

Figure 4.5: Same as Figure 4.4 except the only detachment rate shown is the modified detachment rate found using Eq. (4.31).

rate correction for small clusters has a larger influence on the detachment rate, and cause the critical cluster size to be smaller than expected by the unmodified theory.

Figure 4.5 shows the attachment rate and the detachment rates for both our modified kinetic theory (Eq. (4.31)) and the unmodified kinetic theory (Eq. (4.8)) for water droplets in a 240 K vapor at a supersaturation $S = 10$ for cluster sizes up to $n = 134$. The general shapes of the curves are representative of the results for all simulations. The modified dimer, trimer, and tetramer ($n = 2$–4) detachment rates are higher than the unmodified rates due to the large temperature fluctuations experienced by the clusters. Collisions with the argon carrier gas atoms heats the small clusters to the critical temperature and triggers a detachment event, causing these clusters to be unstable. The sharp decline in the detachment rate at $n > 4$ is due to the correction for small clusters (Eq. (4.30)), which makes clusters more stable. As the cluster size increases the detachment rate found using our modified theory does not rise monotonically. This is due to the relatively low number of detachment events (1000) used to calculate the detachment rate at each cluster size. In this simulation our modified theory detachment rate crosses under the attachment rate at $n = 7.92$, and we consider the critical cluster size then to

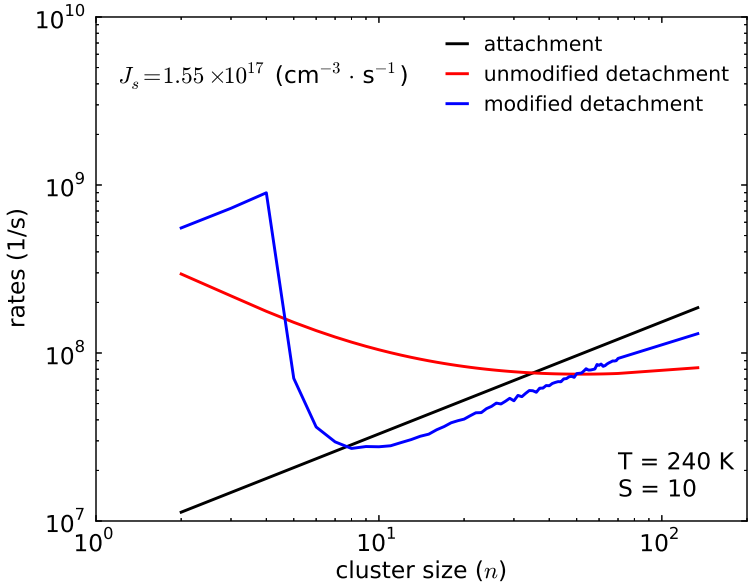

Figure 4.6: Same as Figure 4.5 except the simulations are allowed to run until clusters have undergone 10000 detachments. The nucleation rate J_s is found using the last 5000 detachment events

be $n^* = 8$. We calculate the nucleation rate using cluster sizes up to $2n^* = 16$ to obtain $J_s = 1.37 \times 10^{17}$ cm$^{-3}\cdot$ s^{-1}.

The jaggedness of the modified detachment rate from $n \approx 8$ to $n = 70$ in our simulations is reduced by increasing the required detachments to 10000, as shown in Fig 4.6, but still does not exhibit a monotonic rise. We again find $n^* = 8$ and calculate the nucleation rate to be $J_s = 1.55 \times 10^{17}$ cm$^{-3}\cdot$ s^{-1}.

We expect that for larger cluster sizes the temperature fluctuations and detachment correction for small clusters to be less severe, and the modified detachment rate to approach the unmodified rate. However, in Figure 4.5, for cluster sizes above n^* our detachment rate does not diverge significantly from the attachment rate. Figure 4.7 shows a simulation, also with a vapor temperature of 240 K and supersaturation $S = 10$ but, with clusters sizes up to $\approx 200n^*$. The difference in the nucleation rate J_s from that in Figure 4.5 is due the Monte Carlo techniques and is an indication of the sensitivity of the nucleation rate to the thermal history of the clusters. In this case, the modified detachment rate begins to diverge, but does not yet come close to the unmodified detachment rate as expected. To find where the two rates meet is currently beyond the ability of the

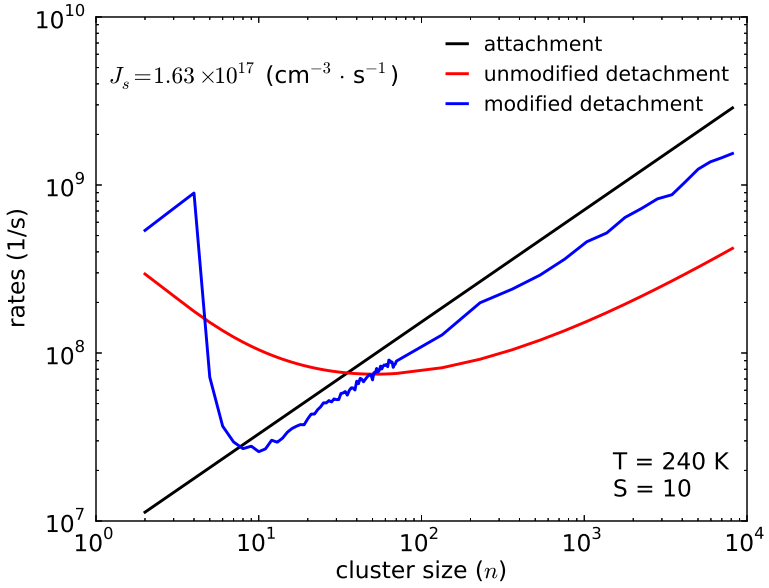

Figure 4.7: Same as Figure 4.5 except rates are calculated for clusters sizes up to ~ 200 times the critical cluster size found using the unmodified kinetic nucleation theory.

computer used to conduct the simulations in this work.

4.4.2 Critical cluster sizes

For all simulations with $S \geq 6$ the critical cluster size found by our modified theory is lower than the sizes found using the unmodified theory or CNT. Table 4.3 lists the critical sizes found in all simulations performed. Figure 4.8 shows the critical cluster sizes found using the modified and unmodified kinetic theories as well as critical cluster sizes expected from CNT. Sizes found using the unmodified theory are in good agreement with those found using CNT and clearly show the trend of a reduction in critical cluster size for higher temperatures and higher supersaturations. Sizes found using the modified theory are consistently low, but still exhibit the same temperature and supersaturation trend. These low critical cluster sizes are due to the stability enhancement granted by the rate correction for small clusters.

Table 4.3: Critical cluster sizes for all simulations using the modified kinetic nucleation theory with 2000 detachments (except where noted otherwise).

	Temperature (K)				
S	220	230	240	250	260
6			10[a]	7	7[a]
8		13	9	7	7
10		10	8	7	6
12	12	9	8	7	6
14	11	9	8	7	
16	10	9	8		
18	10	9	8		
20	10	8			
22	9				
24	9				
26	9				
28	9				
30	8				

[a] simulation used last 5000 detachment events out of 10000

4.4.3 Nucleation rates

Nucleation rates calculated in this work are listed in Table 4.4 and range from 10^{12} to 10^{21}. In Figure 4.9 we show nucleation rates found using the modified and unmodified kinetic theories, along with those found using CNT and experimental results from Wölk and Strey (2001). Our modified theory always over predicts nucleation rates compared to both CNT and the experimental data. Rates for the five temperatures tested follow the same trend of increasing with increasing supersaturation. However, our modified rates reach higher values at lower supersaturations ($S = 6$, for example) and only grow slightly as supersaturation increases. As an example, for $T = 230$ K, across the supersaturation range $S = 8$–20, our modified theory nucleation rate gains only one order of magnitude, while the unmodified theory gains twelve. The unmodified kinetic theory over predicts nucleation rates by 4 to 6 orders of magnitude. At sufficiently high supersaturations (at $S \approx 23$ at 220 K), the unmodified theory over predicts nucleation rates when compared to the modified theory.

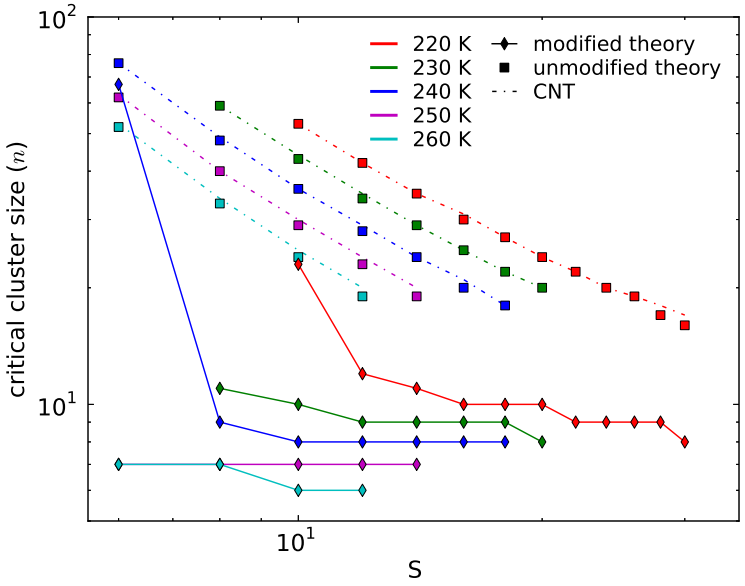

Figure 4.8: Critical cluster sizes for water droplets as a function of supersaturation S for vapor temperatures of 220 (red), 230 (green), 240 (blue), 250 (magenta), and 260 (cyan) K. Sizes are found using the modified (diamonds) and unmodified (squares) kinetic nucleation theories. The connecting lines are a guide for the eye. Critical sizes found using CNT are also shown.

4.4.4 Carrier gas pressure changes

We also ran simulations varying the pressure of the argon carrier gas. Figure 4.10 shows modified detachment rates found using seven different argon carrier gas pressures. All simulations were conducted at a vapor temperature of 240 K and supersaturation $S = 10$. The attachment rate, unmodified detachment rate, and the modified detachment rate for $p_{Ar} = 146\ p$, are the same as in Figure 4.5. The attachment and unmodified detachment rates are the same for all seven carrier gas pressures, since neither Eq. (4.2) nor Eq. (4.8) are dependent on the argon carrier gas pressure.

Higher argon carrier gas pressures results in higher cluster-carrier gas interaction rates (see Eq. (4.34)). For the smallest clusters ($n \lesssim 20$), the extreme temperature fluctuations due to these interactions cause increased detachment rates. However, the overall effect of an increased carrier gas pressure is expected to stabilize the cluster temperature and to therefore reduce the detachment rate. As seen in Figure 4.10 the modified detachment

Table 4.4: Nucleation rates for all simulations using the modified kinetic nucleation theory for cluster sizes up to $2n^*$ and 2000 detachments.

Nucleation Rate ($cm^{-3} \cdot s^{-1}$)					
	Temperature (K)				
S	220	230	240	250	260
6			1.80×10^{16}[a]	1.03×10^{19}	3.51×10^{20}[a]
8		1.20×10^{14}	6.90×10^{16}	2.28×10^{19}	6.21×10^{20}
10		6.37×10^{14}	1.37×10^{17}	4.01×10^{19}	1.27×10^{21}
12	2.06×10^{12}	1.55×10^{15}	2.68×10^{17}	5.90×10^{19}	1.85×10^{21}
14	3.12×10^{12}	2.25×10^{15}	4.46×10^{17}	1.09×10^{20}	
16	8.81×10^{12}	2.66×10^{15}	7.70×10^{17}		
18	1.20×10^{13}	3.89×10^{15}	9.96×10^{17}		
20	1.82×10^{13}	8.51×10^{15}			
22	2.78×10^{13}				
24	4.86×10^{13}				
26	6.57×10^{13}				
28	7.24×10^{13}				
30	9.42×10^{13}				

[a] simulation used last 5000 detachment events out of 10000

rates associated with higher carrier gas pressures diverges from the attachment rate more than the lower carrier gas pressure detachment rates.

The increased modified detachment rates at small cluster sizes for higher carrier gas pressures reduces the nucleation rate and results in larger critical cluster sizes as seen in Figure 4.11. Table 4.5 lists the critical cluster sizes and nucleation rates found at the different carrier gas pressures. Over nearly two orders of magnitude difference in carrier gas pressures we see more than an eight order of magnitude drop in the nucleation rate. The highest carrier pressure we tested still results in a nucleation rate approximately six orders of magnitude larger than that found by Wölk and Strey (2001).

4.4.5 Sublimation energies from available data

Figure 4.12 shows the modified detachment rate resulting from using the sublimation energies of Shank et al. (2009) (for the dimer) and Wang and Bowman (2011) (for the trimer). The attachment and unmodified detachment rates are the same as in Figure 4.5. The inclusion of these sublimation energies do not affect the modified detachment rates

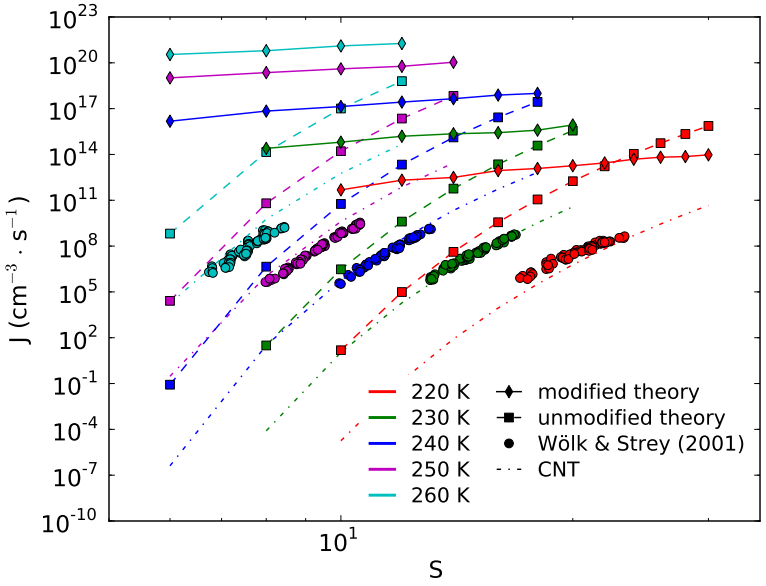

Figure 4.9: Nucleation rates as a function of supersaturation S for water droplets for vapor temperatures of 220 (red), 230 (green), 240 (blue), 250 (magenta), and 260 (cyan) K. Rates are calculated using the modified (diamonds) and unmodified (squares) kinetic nucleation theories and CNT (dash-dot curves). Also shown are experimental values of Wölk and Strey (2001).

because the detachment rates of the dimer and trimer are determined by the temperature fluctuations. A monomer detaches from the dimer and trimer because these clusters reach the temperature limit, rather than from the quanta of energy available overcoming the sublimation energy quanta.

Using sublimation energies calculated from the data of Lenz and Ojamäe (2009) for $n = 2$–60, however, drastically changes our modified detachment rate, as shown in Figure 4.13. The figure shows the same attachment and unmodified detachment rates as in the other figures for water droplets at $T = 240$ K and $S = 10$. For $n > 60$ we used sublimation energies calculated from Eq. (4.19). Large changes in the sublimation energy with cluster size (see Figure 4.2) result in large changes in the modified detachment rate with cluster size. As cluster sizes increase, the detachment rate alternates between being higher and lower than the attachment rate. The high detachment rates are associated with cluster sizes with low sublimation energies and the low rates with high sublimation energy clusters. A determination of a single critical cluster size is impossible. We could

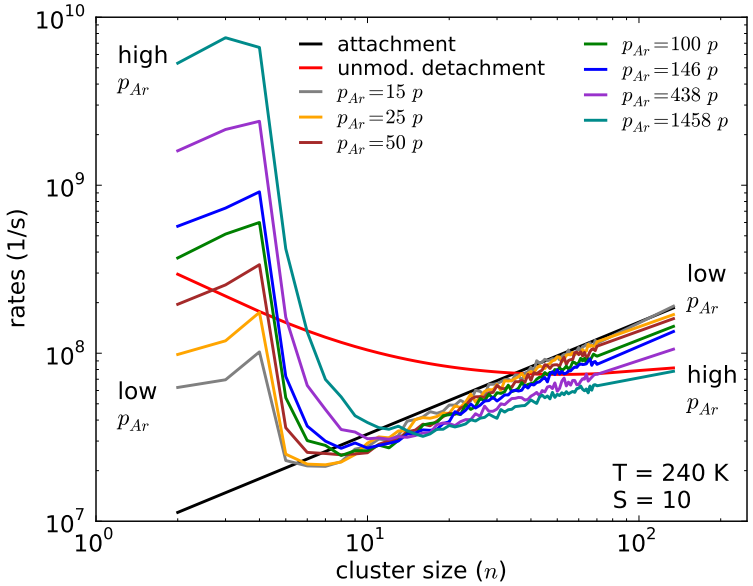

Figure 4.10: Modified detachment rates for seven different argon carrier gas pressures at a vapor temperature of 240 K and supersaturation $S = 10$. $p_{Ar} = 146\ p$ (blue data) corresponds to the carrier gas pressure used in the other simulations at the same temperature and supersaturation.

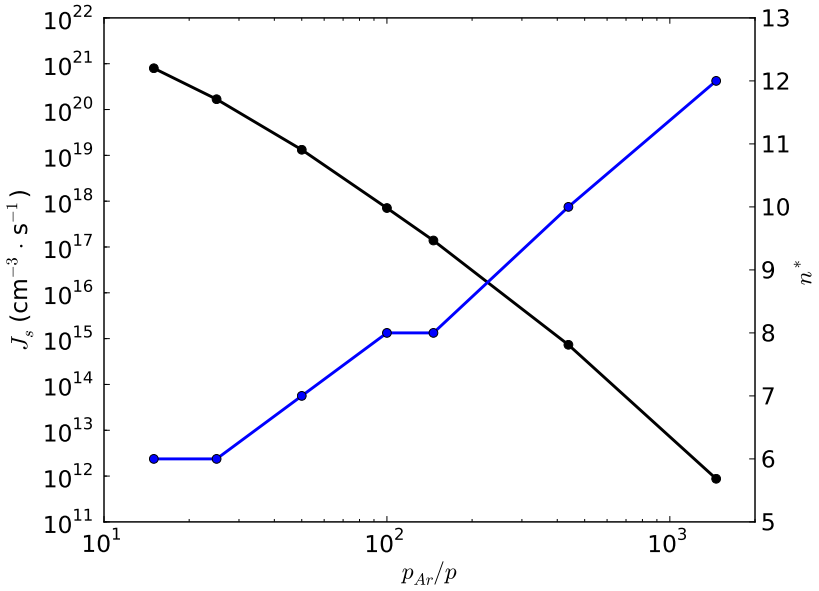

Figure 4.11: Nucleation rates (black) and critical cluster sizes (blue) for increasing carrier gas pressures p_{Ar}/p.

Table 4.5: Critical cluster sizes and nucleation rates for increasing argon carrier gas pressures.

Argon Pressure (p_{Ar}/p)	Critical Cluster Size (n)	Nulceation Rate ($\mathrm{cm}^{-3}\cdot\ \mathrm{s}^{-1}$)
15	6	7.33×10^{20}[a]
25	6	1.65×10^{20}
50	7	1.11×10^{19}
100	8	8.64×10^{17}
146	8	1.37×10^{17}
438	10	7.23×10^{14}
1458	12	1.10×10^{12}

[a] simulation used last 5000 detachment events out of 10000

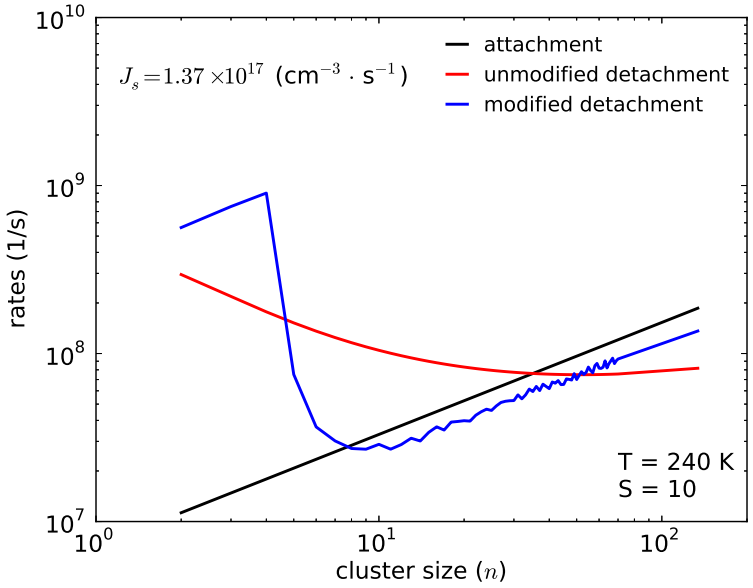

Figure 4.12: Attachment, unmodified detachment, and modified detachment rates for water droplets in a surrounding vapor at $T = 240$ K and $S = 10$ using dissociation energies of Shank et al. (2009) and Wang and Bowman (2011).

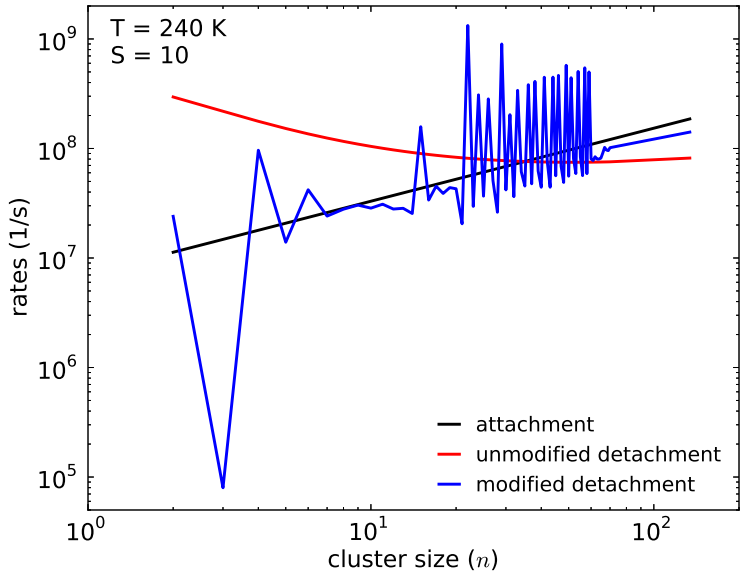

Figure 4.13: Attachment, unmodified detachment, and modified detachment rates for water droplets in surrounding vapor at $T = 240$ K and $S = 10$ using binding energy data of Lenz and Ojamäe (2009).

choose the first cluster size that has a detachment rate that is lower than its attachment rate ($n = 8$, in this case). Alternatively, we could choose $n = 60$ because there are no more larger cluster sizes that have detachment rates greater than their attachment rates, but this may be a false assumption because we have no data for the sublimation energies of clusters larger than $n = 60$. Therefore, we do not calculate a nucleation rate from this simulation.

4.5 Carbonaceous grains

Calculated in the same manner as for water, attachment and detachment rates for carbonaceous grains in a hydrogen carrier gas are shown in Figure 4.14. Sublimation energies were calculated using Eqs. (4.19) and (4.36). The relevant carbon physical properties are listed in Table 4.6. To find the internal energy of the carbon monomer we use Eq. (3.3) of Guhathakurta and Draine (1989). We assume the surrounding vapor to be at $T = 2500$ K and $S = 5$. Due to computational costs, rates are calculated using the last 500 detach-

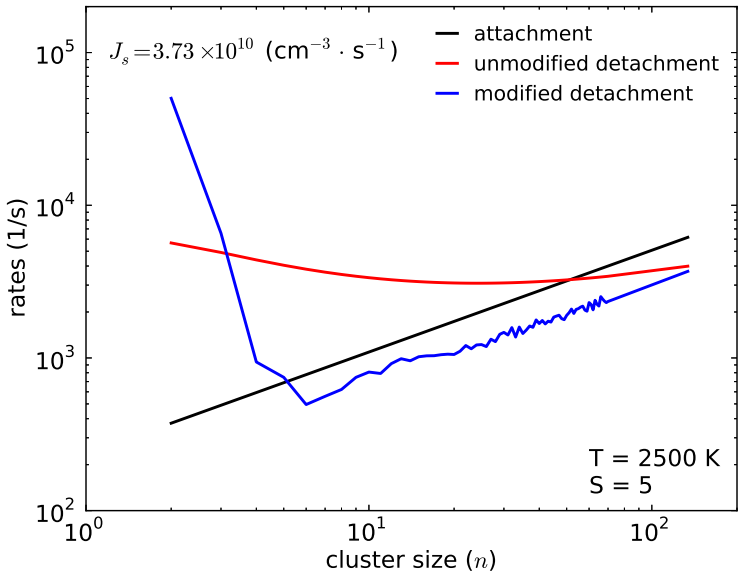

Figure 4.14: Attachment, unmodified detachment, and modified detachment rates for carbonaceous grains with a hydrogen carrier gas at $T = 2500$ K and $S = 5$.

Table 4.6: Physical properties of carbon (graphite).

Property	Value
molecule mass (g)	1.9944×10^{-23}
density (g cm^{-3})	2.23
critical temperature (K)[a]	6810
Debye temperature (K)[b]	420
Surface energy (erg cm^{-2})[c]	1500
Equilibrium gas density (cm^{-3})[d]	$\frac{6.9\times10^{13}e^{-84428.2/T_{grain}}}{kT_{grain}}$
Bulk sublimation energy (erg)[d]	$1.1831760 \times 10^{-11}$

[a] Leider et al. (1973)
[b] Guhathakurta and Draine (1989)
[c] Tabak et al. (1975)
[d] Keith and Lazzati (2011)

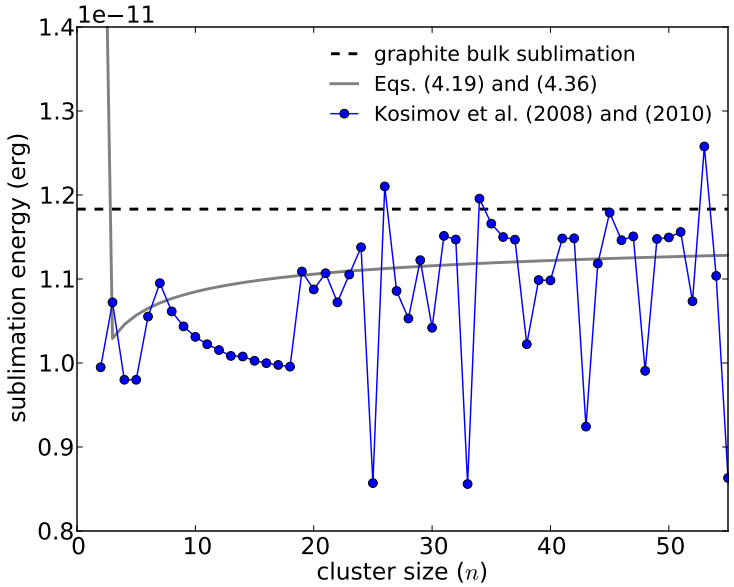

Figure 4.15: Sublimation energies for carbon clusters $n = 2$–55 calculated with Eq. (4.19) from binding energy data of Kosimov et al. (2008, 2010) (blue filled circles) and found using Eq. (4.36) (gray curve). The horizontal, dashed black line is the bulk sublimation energy for graphite.

ment events out of 1000.

The attachment and detachment rates for carbonaceous grains exhibit similar behavior to water droplets. The modified detachment rate is high for the dimer due to the temperature fluctuations, but the rates for larger clusters decline steeply and are lower than the attachment rate at $n = 6$, the critical cluster size for this simulation. The modified detachment rate does not exhibit monotonic behavior as the unmodified detachment rate does. The resulting nucleation rate is $J_s = 3.73 \times 10^{11}$ cm$^{-3}\cdot$ s^{-1}.

We use binding energy data for carbon clusters of $n = 2$ up to $n = 55$ from Kosimov et al. (2008, 2010) to calculate the cluster sublimation energies with Eq. (4.19), shown in Figure 4.15. Also shown are sublimation energies found using Eqs. (4.19) and (4.36) (gray curve) and the bulk sublimation energy for graphite (horizontal, dashed black line). There are only three cluster sizes that have sublimation energies above the bulk sublimation energy value. We expect the sublimation energy to approach the bulk limit as clusters get larger, so we ignore these high sublimation energies. Instead, we use the lower sublimation energy value for a given cluster size when finding the modified

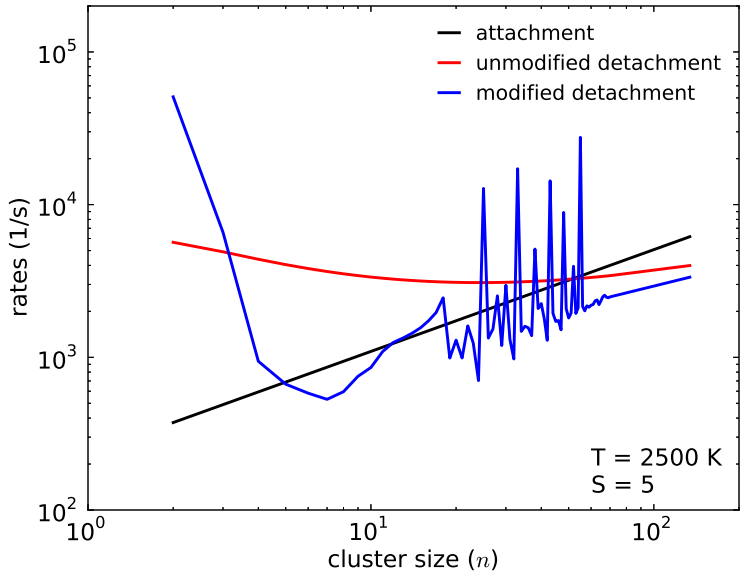

Figure 4.16: Attachment, unmodified detachment, and modified detachment rates for carbonaceous grains in a surrounding vapor at $T = 2500$ K and $S = 10$ using the binding energy data of Kosimov et al. (2008, 2010)

detachment rates.

The attachment and unmodified detachment rates in Figure 4.16 are the same as in Figure 4.14. Similar to the case for water droplets, carbon grains have multiple cluster sizes with high modified detachment rates which cause the determination of a critical cluster size to be impossible. We also do not calculate the nucleation rate for this simulation.

4.6 Discussion

The overall effect of the temperature fluctuations is to increase the rate of detachment of monomers from the cluster, while the rate correction for small grains reduces the detachment rate. Both of these effects are strongest on the smallest clusters. The rate correction for small grains dominates for $n \lesssim 40$ and results in reduced critical cluster sizes. For larger clusters the temperature fluctuations dominate and the modified detachment rate is higher than the unmodified detachment rate. The temperature fluctuation domination

continues to grain sizes larger than our current computing capabilities.

The critical clusters found with our modified theory are smaller than those found by CNT. Our smaller critical clusters result in higher nucleation rates than found in the experimental results of Wölk and Strey (2001). We find nucleation rates a factor of 10^5 to 10^{13} times larger than their experimental rates. Such large discrepancies are not completely out of the ordinary for nucleation work. Earlier attempts to improve upon classical nucleation theory have had similar discrepancies with Lothe and Pound (1962) suggesting that experimental rates for water nucleation were too low by a factor of $\sim 10^{17}$ (Lothe and Pound, 1962; Feder et al., 1966). The reduced critical clusters that we find may make comparison of our results with experiment inappropriate. To obtain nucleation rates in expansion cloud chamber experiments, droplets must grow to sufficient size in order to be counted (Wagner, 1985; Strey et al., 1994). Droplets may need to form through coagulation, in order to reach such size.

Our theory also predicts a strong dependence of the nucleation rate on the pressure of the carrier gas. For the smallest clusters ($n \lesssim 15$), increased carrier gas pressures causes increased detachment rates due to temperature gains from successive carrier gas interactions. However, for stable grains the carrier gas collisions tend to regulate the grain temperature bringing the detachment rates closer to the unmodified detachment rate values. We find that increases in carrier gas pressure increases the size of the critical cluster. More importantly, the increased detachment rates make nucleation more difficult and causes a drop in the nucleation rate. The comparison of this prediction with observations is ambiguous. McGraw and LaViolette (1995) claim that observations do not show any dependence of the nucleation rate on the carrier gas pressure. However a positive correlation was found by Anisimov and Vershinin (1990), who observed an increase in the nucleation rate of dibutylpthalate for increase carbon dioxide carrier gas pressures. On the other hand, Katz et al. (1988) found decreased nucleation rates for nonane, in agreement with our results. Again, we remind the reader that experimental nucleation rates might be affected by coagulation and the comparison should be taken with care. Whether there is an observed dependence of the nucleation rate on the carrier gas pressure and what is the nature of such dependence is still, at best, debatable.

In principle, the agreement of our theory with observations should be improved by using accurate values for the dissociation energy of small molecular clusters. However, experimental values are not readily available in the literature. An alternative is the use

of free energies computed with density functional theory techniques (DFT; e.g., Lenz and Ojamäe (2009) and Kosimov et al. (2008, 2010)). The inclusion of DFT-based dissociation energies found using B3LYP methods to find the binding energies result in erratic detachment rates as a function of cluster size for water clusters. This is due to the excessive fluctuations in the sublimation energies between clusters with similar size. As a matter of fact, DFT has been known to "fail to adequately describe dispersion effects," such as hydrogen bonding (van Mourik and Gdanitz, 2002). To correct for this limitation, Lenz and Ojamäe (2009) scale their B3LYP calculations to the dimer experimental interaction energy value. Using these binding energies, more than half the sublimation energies found through Eq. (4.19) lie above the bulk sublimation energy value for water. Clusters with these high sublimation energies are quite stable. Likewise, many clusters have sublimation energies much lower than those calculated through Eqs. (4.19) and (4.36), and these clusters are extremely unstable. The use of these sublimation energies results in the erratic modified detachment rates seen in Figure 4.13. Similar results are seen in the formation of carbonaceous grains in Figure 4.16 using the binding energy data from Kosimov et al. (2008, 2010). While it is possible to calculate the nucleation rate using the modified detachment rates, we do not have confidence in such calculations. The critical cluster size n^* is impossible to determine and J_s in Eq. (4.32) depends on finding attachment and detachment rates for cluster sizes up to $2n^*$.

The modifications we include here do not form a complete modified kinetic theory of nucleation. Cluster temperatures are also expected to be effected by radiative processes. After a rise in temperature, clusters may emit one or more photons in order to cool rather than ejecting a monomer (Lazzati, 2008; Keith and Lazzati, 2011) This process is especially important when considering dust nucleation in astrophysical environments as dust particles often absorb visible radiation and reemit it at infrared wavelengths. Therefore, radiative cooling will be included in future endeavors to improve kinetic nucleation theory.

4.7 Conclusions

We developed a modified kinetic theory of nucleation and applied it to the formation of water droplets in an argon carrier gas for temperatures between $T = 220$ K and $T = 260$ K. Our modified theory takes into account cluster temperature fluctuations due

to the attachment and detachment of monomers and collisions with carrier gas atoms, and detachment rate corrections for small clusters. In agreement with Keith and Lazzati (2011), we find that these two modification compete with each other. We find nucleation rates to be $\sim 10^5$ to 10^{13} times higher than the experimental results of Wölk and Strey (2001).

We also include sublimation energies for water clusters calculated from binding energy data of B3LYP methods of Lenz and Ojamäe (2009). However, we are limited by the available data to clusters containing only $n \leq 60$ monomers. Moreover, the sublimation energies for many of these clusters are larger than the bulk sublimation energy for water. These sublimations energies result in erratic detachment rates and make nucleation rate calculations problematic. Energy calculations which are more accurate and encompass larger cluster sizes will be of benefit for finding more accurate nucleation rates. Qualitatively similar results are found for the formation of carbonaceous grains in a hydrogen carrier gas. We cannot compare our results to any experimental results. Instead, we find that our modified kinetic theory results in nucleation rates $\approx 10^{14}$ times larger than CNT calculations under similar initial conditions.

The modifications to the kinetic theory included in this work represent only collisional and small cluster effects and do not constitute a fully modified theory. A fully developed kinetic theory also needs to include radiative processes effects. This will allow the clusters to overcool, and will be an additional source of temperature fluctuations Tielens (2005); Lazzati (2008); Keith and Lazzati (2011).

4.8 Acknowledgements

This work was partially supported by a NC State Faculty Research and Professional Development grant and by NSF grant AST-1150365.

Chapter 5

Kinetic nucleation of carbonaceous dust in type II SNe

In Section 2.4.4, modifications to nucleation theory and the motivation for using a kinetic theory approach were discussed. Chapter 3 presented a parametric study of applying two modifications, the shape factor c and the sticking coefficient γ, to CNT. Chapter 4 laid out how to include temperature fluctuations and detachment rate corrections for small clusters to the kinetic nucleation theory. The difficulty of eliminating the capillarity approximation from nucleation rate calculations due to the scarcity of accurate cluster binding energy data available for both water and carbon was also discussed. This chapter focuses on applying the kinetic nucleation theory to the formation of carbonaceous dust in the same CCSN as presented in Chapter 3.

The chapter is organized as follows. In Section 5.1 the results of carbonaceous dust formation using the unmodified kinetic nucleation theory are presented for a CCSN. Section 5.2 outlines the addition of the different modifications applied to the kinetic nucleation theory. In Section 5.2.3 we discuss the difficulties in applying temperature fluctuations and detachment rate corrections for small clusters.

5.1 Carbonaceous dust formation with kinetic nucleation theory

As in Chapter 3, we use the hydrodynamic and elemental composition results of Umeda and Nomoto (2002) for a 20 $M_\odot$, $Z = 0$ progenitor CCSN with an explosion energy of 10^{51} erg. Again, the formation of CO molecules is considered to be complete so that carbonaceous grains form only in areas where the abundance of carbon is greater than that of oxygen (see Figure 3.3).

The unmodified detachment rate is the commonly used approximation of the more general detachment rate Eq. (4.7):

$$g_n = \gamma c v_0^{2/3} \frac{p_e}{(2\pi m_0 k T_{gas})^{1/2}} (n-1)^{2/3} \exp\left\{\frac{\lambda - E_n + E_{n-1}}{kT_{gas}}\right\}.$$

With the help of the capillarity approximation, we can simplify the exponential in g_n,

$$\begin{aligned} \exp\left\{\frac{\lambda - E_n + E_{n-1}}{kT_{gas}}\right\} &= \exp\left\{\frac{c\sigma v_0^{2/3}}{kT_{gas}}\left(n^{2/3} - (n-1)^{2/3}\right)\right\}, \\ &= \exp\left\{\frac{c\sigma v_0^{2/3}}{kT_{gas}} n^{2/3}\left(1 - \left(1 - \frac{1}{n}\right)^{2/3}\right)\right\}, \end{aligned} \tag{5.1}$$

and use the binomial approximation, $(1+x)^y \approx 1 + yx$, to obtain:

$$\exp\left\{\frac{\lambda - E_n + E_{n-1}}{kT_{gas}}\right\} = \exp\left\{\frac{2c\sigma v_0^{2/3}}{3kT_{gas} n^{1/3}}\right\}. \tag{5.2}$$

Due to the binomial approximation, Eq. (5.2) is really only applicable for cases where $n \gg 1$. Since this form is the more commonly used form, we refer to it as the *unmodified* detachment rate, and the less approximated form (Eq. (5.1)) as the *basic* detachment rate. The differences in using the two detachment rates can be seen in Figure 5.1. The unmodified equation (red curve) predicts lower detachment rates than the blue dashed basic rate curve for the smallest clusters ($n \lesssim 10$). Consequently, the unmodified equation finds a higher nucleation rate: $J_s = 1.41$ ($\mathrm{cm}^{-3} \cdot s^{-1}$) as compared to $J_s = 0.182$ ($\mathrm{cm}^{-3} \cdot \mathrm{s}^{-1}$) found by the basic equation. For both of the theories we consider the critical cluster to be $n^* = 52$.

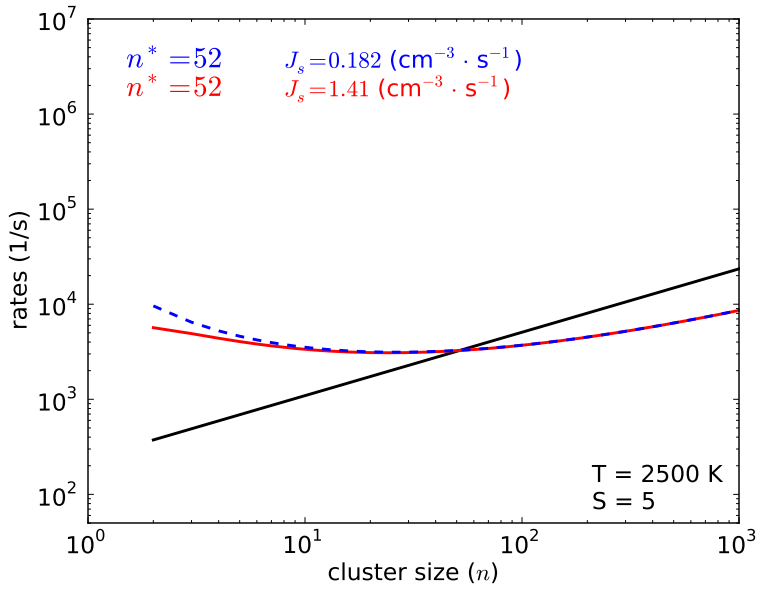

Figure 5.1: Attachment (black), basic (blue, dashed) and unmodified (red) detachment rates for carbon clusters at $T = 2500$ K and $S = 5$, with critical cluster size of $n = 52$ for the basic and unmodified detachment rates, respectively.

5.1.1 Unmodified kinetic nucleation theory

Results found using kinetic nucleation theory (KNT)

$$J_s = f_1 C_1 \left[1 + \sum_{n=2}^{M-1} \frac{g_2 g_3 \ldots g_n}{f_2 f_3 \ldots f_n} \right]^{-1},$$

with the unmodified detachment rate of Eq. (4.8):

$$g_n = \gamma c v_0^{2/3} \frac{p_e}{(2\pi m_0 k T_{gas})^{1/2}} (n-1)^{2/3} \exp\left\{ \frac{2c\sigma v_0^{2/3}}{3kT_{gas} n^{1/3}} \right\},$$

are compared to those found using the CNT nucleation rate

$$J_s = \gamma \sqrt{\frac{c^3 v_0^2 \sigma}{18\pi^2 m_0}} \left(\frac{p_v}{kT} \right)^2 \exp\left\{ \frac{-4c^3 v_0^2 \sigma^3}{27(kT)^3 (\ln S)^2} \right\}$$

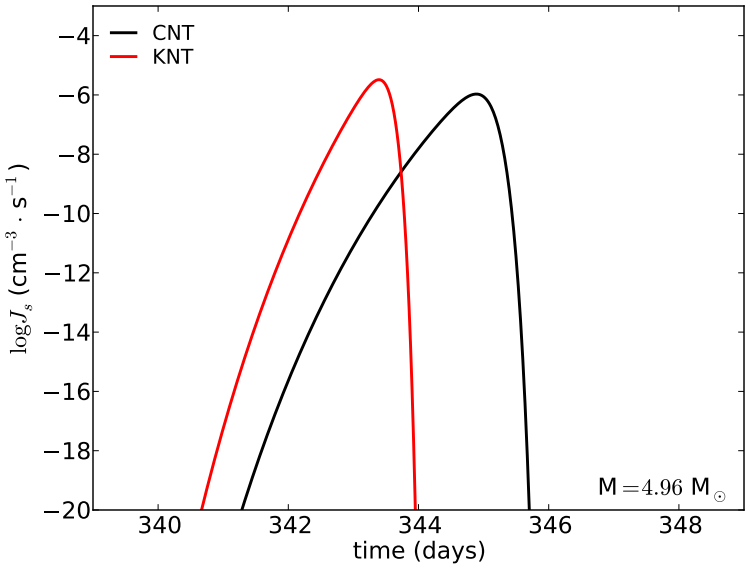

Figure 5.2: Nucleation rates for spherical grains, $c = (36\pi)^{1/3}$, with a sticking coefficient of $\gamma = 1.0$ as a function of time after explosion found using CNT (black curve) and KNT (red curve) at an enclosed mass of 4.96 $M_\odot$.

of Fallest et al. (2011). Figure 5.2 shows the nucleation rate as a function of time at an enclosed mass of 4.96 $M_\odot$ found using CNT (black curve) and KNT (red curve). The grains are considered to be spherical ($c = (36\pi)^{1/3}$) with sticking coefficient $\gamma = 1.0$. In this case, both theories rely on the same assumptions (spherical grains, sticking coefficient of unity, and the capillarity approximation), however, the results are not the same. The time at which the nucleation rate is a maximum is considered the condensation time. The maximum nucleation rates, condensation times, and total dust masses formed for both curves are listed in Table 5.1. According to the KNT curve, grains form earlier after the explosion than they do according to the CNT curve. At earlier times, temperatures and densities are higher, but supersaturation levels are lower. The lower supersaturation levels imply larger critical clusters (see Figure 4.8) and the subsequent growth should result in larger grains overall. However, due to the high nucleation rates and large initial grain sizes the available carbon material is quickly consumed, and KNT predicts a shorter nucleation period than CNT predicts. Therefore, grains have less time to grow in the KNT scenario, which should result in smaller grains. Thus, the KNT scenario predicts

Table 5.1: Maximum nucleation rates, condensation time, and total dust mass formed for carbonaceous grains at an enclosed mass of 4.96 $M_\odot$ using kinetic nucleation theory (KNT) and classical nucleation theory (CNT).

Theory	nucleation rate J_s ($cm^{-3}\cdot s^{-1}$)	condensation time (days)	total dust mass ($M_\odot$)
KNT	3.27×10^{-6}	343.39	5.138×10^{-2}
CNT	1.07×10^{-6}	344.88	5.142×10^{-2}

larger initial grain sizes, but with shorter growth times. These two effects compete with each other to decide the final grain size.

The size distribution of carbon grains is shown in Figure 5.3. Grain radii from CNT are shown in black, and from KNT in red. The two size distributions are very similar, but KNT results in a distribution that follows the distribution suggested by Mathis et al. (1977) slightly better. The deep trough in the KNT distribution occurs for grains with a radius of $\sim 6 \times 10^{-3}$ μm, which consist of $\sim 6 \times 10^4$ carbon atoms. A similar, but less pronounced, trough occurs in the CNT distribution, at a slightly smaller radius. The maximum grain radius is only marginally smaller for KNT than for CNT, suggesting that time of grain growth is more important to final grain size, than the size of the grain at nucleation. The similar size distributions, unsurprisingly, produce similar mass distributions as shown in Figure 5.4. The masses of carbonaceous dust grains found with KNT (red) are shifted towards slightly smaller grain sizes compared to those found with CNT (black), and the total masses of dust formed are nearly the same.

Despite the differences in the nucleation rates and condensation times, the two theories produce similar size and mass distributions, with almost no difference in the total masses of dust formed. Likewise, the extinction curves expected from the two theories (shown in Figure 5.5) are also very similar. The red curve from the KNT theory is consistent with the increased numbers of small grains predicted by KNT. Since processing by the reverse shock is expected to destroy small grains, KNT predicts a smaller fraction of grains would survive to be injected into the ISM.

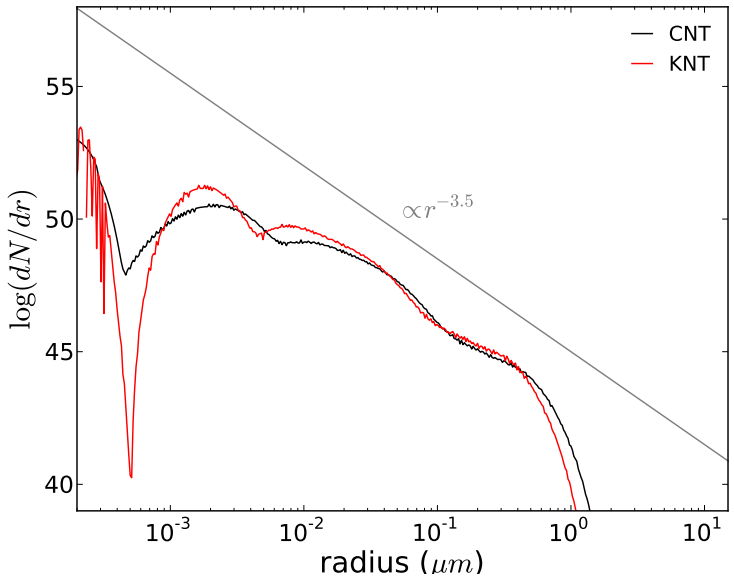

Figure 5.3: Size distributions as a function of grain radius for grains formed in the ejecta of a CCSN using CNT (black) and KNT (red). The distribution of interstellar grains suggested by Mathis et al. (1977) is shown in gray.

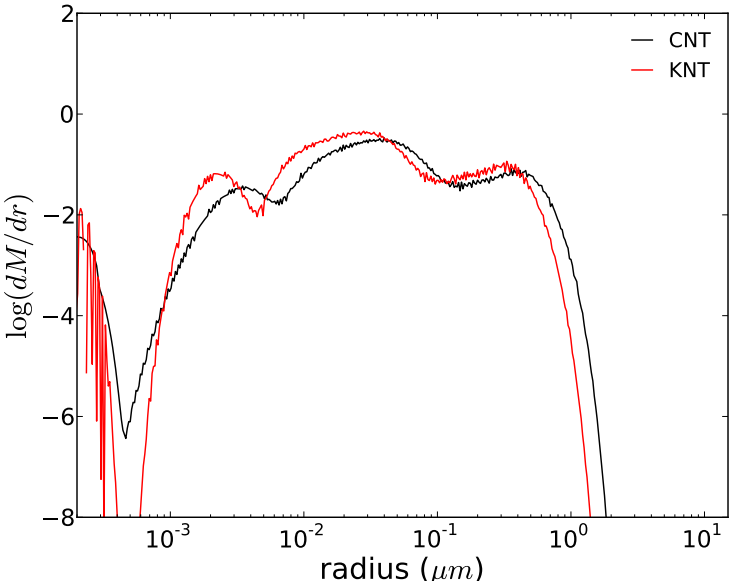

Figure 5.4: Mass distributions as a function of grains radius for grains formed in the ejecta of a CCSN using CNT (black) and KNT (red).

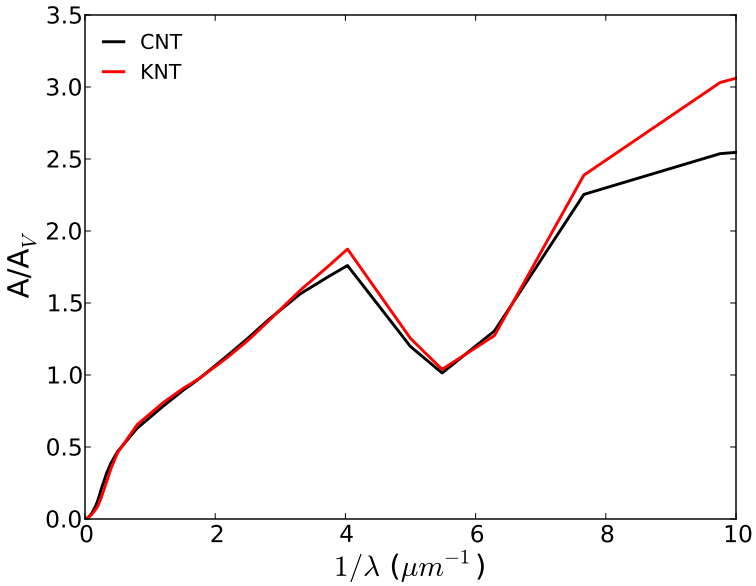

Figure 5.5: Extinction curves associated with the carbon grains predicted to form using CNT (black) and KNT (red).

5.2 Modifications to kinetic nucleation theory

Here we describe the addition of modifications to the kinetic nucleation theory based on the concerns raised in Section 2.4.4. Some of the modifications have already been discussed in Chapters 3 and 4, but will be touched on again here.

5.2.1 Shape factor and sticking coefficient

Changes to the shape factor c and sticking coefficient γ can be applied to both CNT and KNT. In Chapter 3, we discussed the application of these modifications to CNT in the formation of carbonaceous dust grains, and in Chapter 4 we considered their affects when using KNT. As shown in Chapter 4, the shape factor and and sticking coefficient are plainly seen in the attachment rate (Eq. (4.2))

$$f_n = \gamma c v_0^{2/3} \frac{S p_e}{(2\pi m_0 k T_{gas})^{1/2}} n^{2/3} \,,$$

and in the detachment rate (Eq. (4.31), expanded)

$$g_n^* = S_n(T_{cluster})\gamma c v_0^{2/3} \frac{p_e(T_{cluster})}{(2\pi m_0 k T_{cluster})^{1/2}} (n-1)^{2/3} \exp\left\{\frac{\lambda - E_n + E_{n-1}}{kT_{cluster}}\right\}.$$

Assuming constant shape factors and sticking coefficients in finding the nucleation rate (Eq. (4.32)),

$$J_s = f_1 C_1 \left[1 + \sum_{n=2}^{M-1} \frac{\bar{g_2^*}\bar{g_3^*}...\bar{g_n^*}}{f_2 f_3 ... f_n}\right]^{-1},$$

the sticking coefficient is eliminated from the bracketed portion of the nucleation rate. The shape factor, on the other hand, is eliminated only from the pre-exponential factors of the $\bar{g_n^*}/f_n$ ratios (where $\bar{g_n^*}$ is the average detachment rate for an n-sized cluster), because it is also included in the binding energies E_n. Both the shape factor and sticking coefficient remain in the f_1 factor of the nucleation rate:

$$f_1 = \gamma c v_0^{2/3} \frac{S p_e}{(2\pi m_0 k T_{gas})^{1/2}}. \tag{5.3}$$

A sticking coefficient $\gamma < 1.0$ then only serves to reduce the overall nucleation rate, just as it does for CNT (see Eq. (3.2)).

Figure 5.6 shows the nucleation rates for carbonaceous grains formed in the ejecta of the same CCSN used earlier. Rates are shown for predictions found using both CNT and KNT for two shape factors, $c = (36\pi)^{1/3}$ and 9.0, and two sticking coefficients, $\gamma = 1.0$ and 0.01. The curves shown for CNT and KNT with $c = (36\pi)^{1/3}$ and $\gamma = 1.0$ are the same as in Figure 5.2. Both sets of curves are affected in the same way by changes in the shape factor and sticking coefficient. As noted in the Chapter 3, increasing the shape factor reduces the nucleation rate and delays the condensation time of grains, but the enhanced surface-to-volume ratio allows for more efficient grain growth which maintains the reduced nucleation rates throughout the nucleation process. Reduced sticking coefficients also decrease the nucleation rates, but since both nucleation and grain growth are made more difficult, supersaturation levels continue to rise, which allows for higher nucleation rates at the delayed condensation times. The combination of an increased shape factor and reduced sticking coefficient results in greater delays in condensation, and an increased maximum nucleation rate (the dotted curves in Figure 5.6).

Figure 5.7 compares nucleation rates found using Eqs. (4.7) and (4.8) (blue and

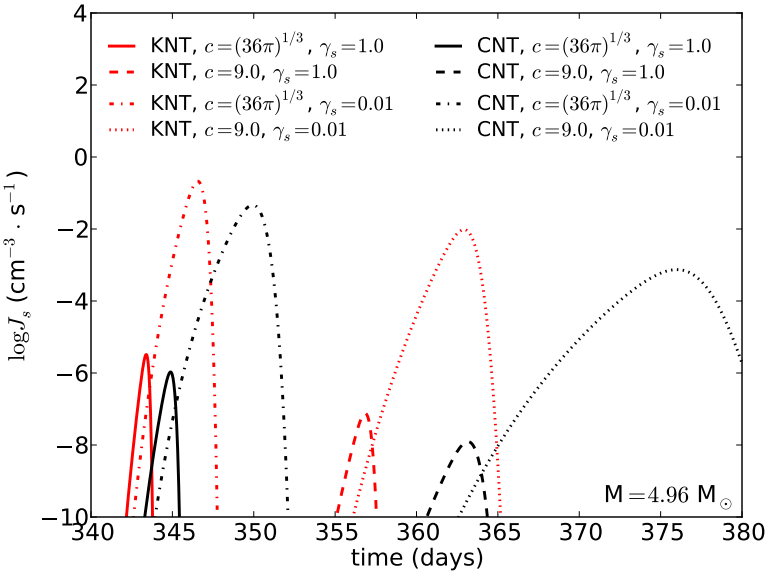

Figure 5.6: Nucleation rates for carbonaceous grains in the ejecta of a 20 $M_\odot$ progenitor CCSN. Rates shown are found using both CNT (black curves) and KNT (red curves) for shape factors, $c = (36\pi)^{1/3}$ and 9.0 (solid and dashed, respectively), and sticking coefficients $\gamma = 1.0$ and 0.01 (dash-dot and dotted, respectively).

red, respectively) for the formation of carbonaceous grains in the ejecta of our 20 $M_\odot$ CCSN. The red curves are the same as those shown in Figure 5.6. When nucleation rate calculations do not include the binomial approximation, grain condensation is delayed slightly due to the reduced nucleation rates. Changes to the shape factor and sticking coefficient have the same effects on rates calculated with Eq. (4.7) as seen previously.

5.2.2 Capillarity approximation

In the event that sublimation or binding energy data are available, both the sticking coefficient and the shape factor are eliminated from the bracketed portion of Eq. (4.32), so that $J_s \propto \gamma c$. This would be a great benefit for eliminating the reliance on the capillarity approximation.

To remove the reliance on the capillarity approximation, the goal is to remove the surface tension σ dependence from g_n (in Eq. (4.8)). The surface tension is used when

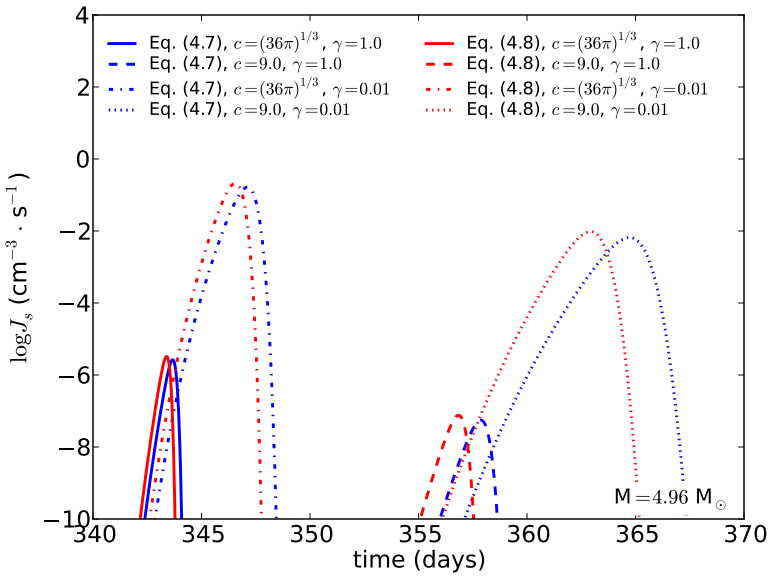

Figure 5.7: Nucleation rates for carbonaceous grains found using KNT with Eq. (4.7) (blue) and Eq. (4.8) (red) at M= 4.96 M$_\odot$ for shape factors $c = (36\pi)^{1/3}$ and 9.0 and sticking coefficient $\gamma = 1.0$ and 0.01.

calculating the binding energy of the n-sized cluster,

$$E_n = \lambda n - c v_0^{2/3} \sigma n^{2/3} \,,$$

(Eq. (4.36)) in the exponential term of g_n. Removal of the surface tension can be accomplished by finding accurate cluster binding energies E_n or sublimation energies B through quantum mechanical methods, such as *ab initio* potential energy surface with diffusion Monte Carlo calculations and DFT techniques.

In Chapter 4 we used the dissociation energies for the water dimer of Shank et al. (2009) and trimer of Wang and Bowman (2011), who both used an "accurate *ab initio* full-dimensional potential energy surface, together with a diffusion Monte Carlo (DMC) calculation" of the zero-point energy of the cluster (Wang and Bowman, 2011). The value for the dimer is reported to be in very good agreement with experimental values found by (Rocher-Casterline et al., 2011), of water dimers dissociating in a supersonic molecular beam. We also used the interaction energies for water clusters of n = 2–60 from Lenz and Ojamäe (2009) to calculate the sublimation energy of the clusters. Lenz and Ojamäe

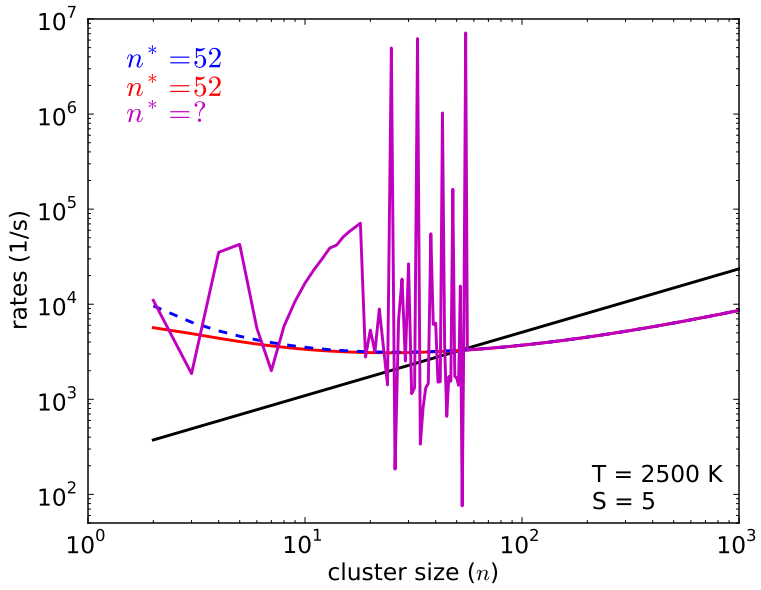

Figure 5.8: Same as Figure 5.1 except with additional detachment rates found using the carbon cluster binding energies of Kosimov et al. (2008) and (2010) (magenta). A single critical cluster size is unable to be determined.

(2009) obtain their interaction energies through DFT techniques using quantum-chemical B3LYP computations. Kosimov et al. (2008) points out that "*ab initio* quantum chemical methods are extremely time consuming". The carbon cluster binding energies used in Chapter 4 were calculated by Kosimov et al. (2008) through energy minimization methods with the classical interatomic potential approach using the reactive empirical bond-order (REBO) potential. This method has been shown to be accurate and much faster than *ab initio* methods (Kosimov et al., 2008). Energy calculations have been conducted for only small clusters ($n \lesssim 60$) (Kosimov et al., 2008). As the number of monomers in a cluster increases, so does the number of stable configurations the monomers can assume. For larger cluster sizes, calculating the binding energies becomes increasingly computationally expensive.

Modified detachment rates including the binding energy data for clusters $n \leq 55$ of Kosimov et al. (2008) and (2010) are shown in Figure 5.8. Above $n = 55$, the modified detachment rates (magenta) are calculated using the capillarity approximation, and therefore are the same as the basic detachment rates. For $n \leq 55$, the rates do not follow a smooth path as the cluster size increases, and are not approximated by either the basic

or unmodified detachment rates. Moreover, these data indicate that the smallest stable cluster is at $n = 24$, however, it is not clear that this should be considered the critical cluster because the next larger cluster is unstable. Between $n = 24$ and $n = 55$ there exist multiple stable clusters that cannot be clearly designated as the critical cluster. The $n = 56$ cluster could be considered the critical cluster because there are no more unstable clusters at larger sizes, however, this is due to limited data available. The erratic behavior of these detachment rates is a direct consequence of using the sublimation energies found through the binding energy data of Kosimov et al. (2008, 2010), as shown in Figure 4.15.

We calculate the nucleation rates of carbonaceous grains using the Kosimov et al. data. In this case, we assume the critical cluster is the first cluster size with a detachment rate lower than its attachment rate. In Figure 5.9 the nucleation rates for dust formation at an enclosed mass of 4.96 $M_\odot$ using the CNT (black) and KNT using the unmodified (red) and basic (blue) detachment rates, as well as detachment rates including the Kosimov et al. data (magenta) are shown for $c = (36\pi)^{1/3}$ and $\gamma = 1.0$. Using the binding energy data significantly reduces the nucleation rate which delays the condensation time to 349.03 days after explosion. Around the condensation time the nucleation rate spikes to similar levels as the other KNT theories. This spike is due to the high supersaturation level ($S \approx 25$) at that time and a corresponding drop in the critical cluster size of $n = 7$. There is a smaller jump in the nucleation rate at $\sim$ 346.46 days after the explosion, which is due to a similar, but smaller, drop in the critical cluster size.

The large spike in the nucleation rate indicates that the bulk of the grain formation occurs in a short period of time. Furthermore, nucleation is quickly shut down after the spike due to the depletion of the available monomers, and grains have not had much time to grow before the nucleation stage is over. Therefore, we expect more smaller grains to be produced. Figure 5.10 shows the mass distribution of these grains compared to those of CNT (black) and the unmodified KNT (red). A larger mass of grains are produced with radii between 8×10^{-4} μm and $\sim 3 \times 10^{-3}$ μm compared to both CNT and the unmodified KNT. The maximum grain size is only between 3 and 4×10^{-1} μm. Even though the total mass of grains formed is also 5.14×10^{-2} $M_\odot$, more grain mass would be expected to be destroyed through processing by the reverse shock.

The extinction curve for these grains is shown in magenta in Figure 5.11 along with the curves for the grains formed using CNT (black) and the unmodified KNT (red). The

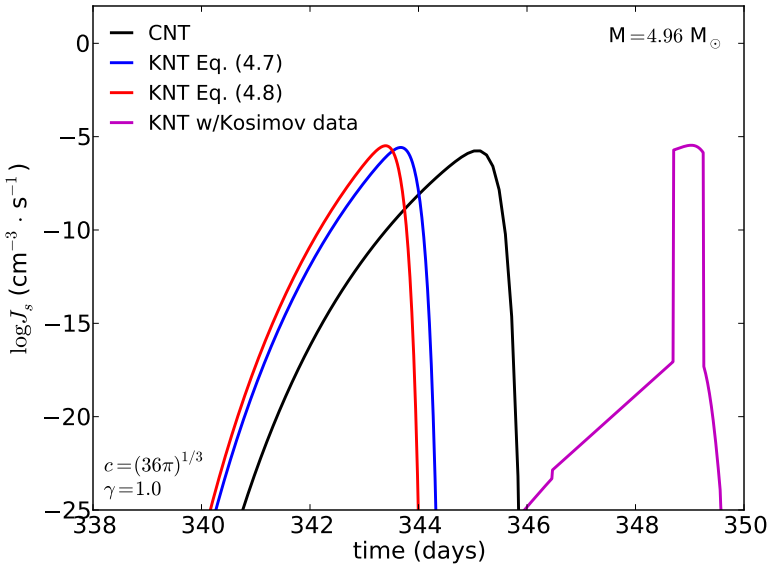

Figure 5.9: Nucleation rates of carbonaceous grain formation at an enclosed mass of 4.96 $M_\odot$. Rates shown are found using CNT (black), KNT with unmodified detachment rates (red), KNT with basic detachment rates (blue), and detachment rates including the data of Kosimov et al. (2008, 2010). All rates assume spherical grains $c = (36\pi)^{1/3}$, with sticking coefficient $\gamma = 1.0$.

grains formed using the binding energy data of Kosimov et al. (2008, 2010) produces a grey extinction curve with $R_V = 11.2$. This is more consistent with distributions that include a large average grain size (see Figures 3.17 and 3.18). This high R_V could be due to the fraction of dust contained in larger grains, e.g. $r > 0.5$ μm, which skews the average grain size toward a larger size.

These results show the importance of having accurate sublimation energy data in order to determine clear critical cluster sizes and accurate nucleation rates with KNT. Due to the limited data available for the binding energies of carbon clusters, eliminating the reliance on the capillarity approximation in KNT does not seem feasible at this time.

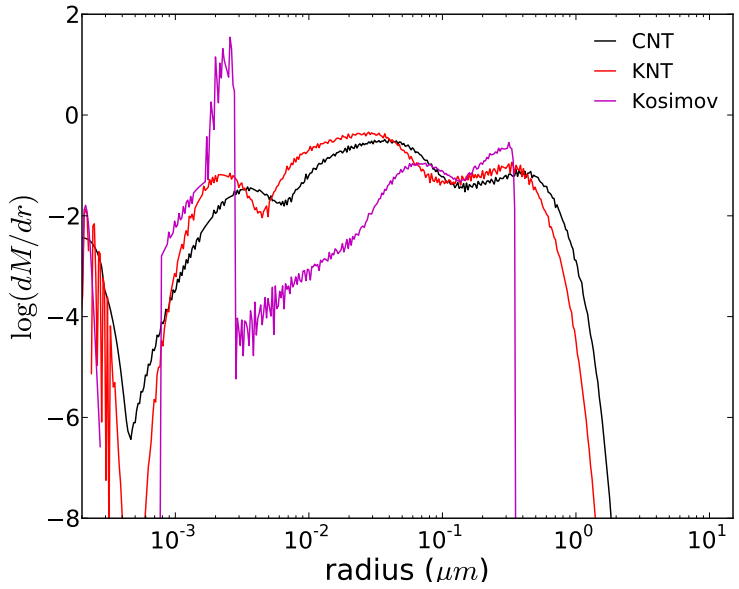

Figure 5.10: Mass distributions of carbonaceous grains formed in the ejecta of a CCSN. Distributions are shown for CNT (black), unmodified KNT (red) and KNT including the binding energy data of Kosimov et al. (2008, 2010).

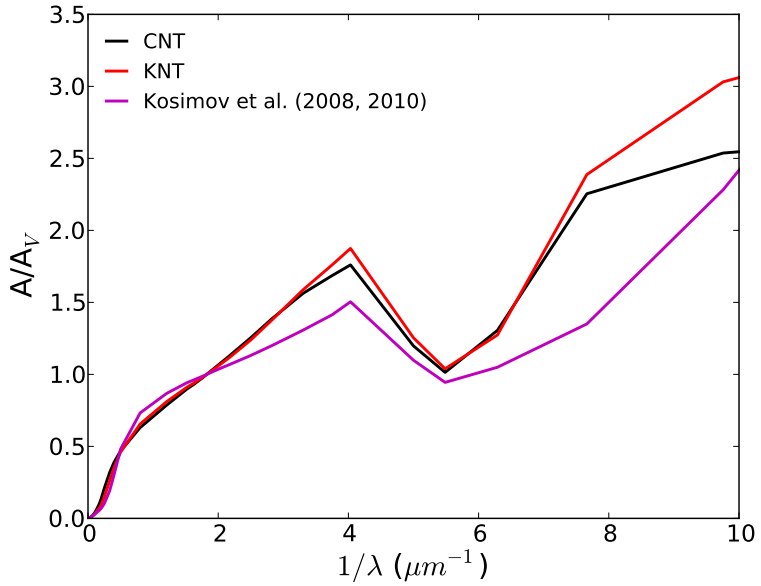

Figure 5.11: Extinction curves for carbonaceous grains formed in the ejecta of a CCSN. Curves shown are grains formed using CNT (black), unmodified (KNT), and KNT including the binding energy data of Kosimov et al. (2008, 2010) (magenta).

5.2.3 Temperature fluctuations and detachment rate corrections for small clusters

The effect of including temperature fluctuations and detachment rate corrections for small grains on the detachment rates for carbon grains were discussed in Chapter 4. To introduce these modifications to the detachment rate calculations it is necessary to introduce energy changes to each cluster. As discussed, our simulations accomplish this through Monte Carlo methods which determine the means by which the energy changes during each code cycle of a given simulation – through monomer attachment or detachment, or through an interaction with a carrier gas monomer. For carbon clusters in a supersaturated vapor with $T = 2500$ K and $S = 5$, average detachment rates were found using the last 500 out of 1000 detachment events.

We find that the temperature fluctuations and detachment rate corrections for small grains compete with each other, in agreement with Keith and Lazzati (2011). The temperature fluctuations increase the detachment rate for all grain sizes due to the high sensitively of the detachment rate on the cluster temperature. The detachment rate correction for small clusters, however, lowers the detachment rate due to its assumption that enough cluster energy needs to be concentrated into a single vibrational degree of freedom to overcome the sublimation energy (Guhathakurta and Draine, 1989). The combination of these two effects result in average detachment rates that are higher than the unmodified detachment rate for very small clusters ($n \leq 3$), but drop steeply and are smaller than the unmodified detachment rate for a range of cluster sizes ($4 \leq n \sim 134$). We refer to these average detachment rates as the *modified* detachment rates $\bar{g}_n^*$. The drop in the modified detachment rate is steep enough that a critical cluster size of $n \approx 6$ is found for the carbonaceous grain simulations in Chapter 4. The modified detachment rates do not diverge very quickly from the attachment rates like the unmodified detachment rates do. When supersaturation levels are low, the modified detachment rates can fluctuate enough to cross the attachment rates at multiple cluster sizes. This leads to the same problem in determining the critical cluster size seen when including binding energy data to the detachment rates.

When temperature fluctuations and detachment rate corrections for small clusters are applied to carbonaceous grain formation, two problems become evident. The first problem is the calculation of nucleation rates for carbonaceous grains, especially at low supersaturation levels, is computationally expensive. The second problem is the inability

to determine a single critical cluster size when the available carbon cluster binding energy data are included, or when supersaturation levels are low. "Low" supersaturation levels in these cases can be considered to be when $S \lesssim 3$.

The simulations for the nucleation of carbon grains in Chapter 4 at $T = 2500$ K and $S = 5$ take ~ 24 hours to be completed on a laptop computer with a 2.2 GHz four-core processor with 8 GB of ram to compute the nucleation rate J_s. This can be considered to be a reasonable amount time to run a simulation, especially when one considers that four simulations can be run simultaneously on the above laptop computer. The maximum cluster size for which the modified detachment rate needed to be calculated in these simulations was $n = 134$ – slightly bigger than twice the critical cluster size determined by the unmodified detachment rate. The detachment rates are independent of the supersaturation levels, however, the attachment rates are directly proportional to them. As supersaturation levels are lowered, the attachment rates are also reduced, which causes the size of the critical cluster to become larger. This in turn increases the number of cluster sizes the simulation code needs to consider, and increases the time to complete the simulation run. If supersaturation levels are low enough so that the attachment rates and modified detachment rates are equal at multiple cluster sizes, the maximum cluster size the simulation code needs to consider increases as the simulation runs. This is same problem seen when using the binding energy data of Kosimov et al. (2008, 2010), except in this case, the problem persists to higher supersaturation levels as well. To make matters worse, as cluster size increases, the time to compute the modified detachment rate also increases. In the case of dust formation in CCSN ejecta, it is desirable to calculate nucleation rates at the lowest possible supersaturation level, in order to predict when dust formation begins. Moreover, as grains nucleate and grow, they deplete available monomers, which helps to keep supersaturations levels low. The supersaturation level decrease due to monomer depletion competes with the supersaturation level increase due to the decreasing temperatures of the expanding ejecta. Eventually, the depletion of monomers triumphs and supersaturation levels decrease until nucleation is shut down. Thus, it is essential to compute nucleation rates at low supersaturation levels in a reasonable amount of time.

Assuming simulations could be completed in a reasonable amount time, we expect early condensation times, and small grains to dominate the size and mass distributions. Our modified theory predicts higher nucleation rates and smaller critical cluster sizes

than predicted by CNT or the unmodified KNT, which will cause nucleation of dust to occur earlier after the SN explosion. The formation of large amounts of small grains is expected to continue and to shut down the nucleation process quickly. This is analogous to the case of nucleation when the binding energy data of Kosimov et al. (2008, 2010) are included, but occurring sooner after the explosion.

Five modifications to nucleation theory have been considered: the shape factor and sticking coefficient of the monomer, eliminating reliance on the capillarity approximation, and the inclusion of temperature fluctuations and detachment rate corrections for small clusters. Each of these modifications can be included in the kinetic nucleation theory, however, only the first two are presently feasible to be included in nucleation rate calculations. The nucleation rate is found to be directly proportional to the sticking coefficient, so that $J_s \propto \gamma$. The nucleation rate can also be found to be directly proportional to the shape factor if binding or sublimation energy data are available for all relevant cluster sizes. This also eliminates the use of the capillarity approximation, however, such energies are available for only a relatively small range of clusters sizes (e.g., $n \leq 60$ for water (Lenz and Ojamäe, 2009) and $n \leq 55$ for carbon clusters Kosimov et al. (2008; 2010)). Additionally, detachment rates found using these energies exhibit multiple cluster sizes where the attachment and detachment rates are equal, suggesting multiple critical cluster sizes. The final two modifications can be included as long as supersaturation levels are not too low, however simulations are computationally expensive. At low supersaturations, determination of a clear critical cluster size is again impossible due to the fluctuations of the modified detachment rate.

When applying the first three modifications to the formation of carbonaceous dust in the expanding ejecta of a CCSN the general effect is to skew grain formation towards later condensation times and smaller grains. However, applying all of these modifications to carbonaceous dust formation in a core-collapse supernova becomes too computationally expensive to be feasible for this project. Future work employing a parallelized version of the code developed during this project may be more successful in including temperature fluctuations and detachment rate corrections to dust formation in CCSNe.

Chapter 6

Conclusions

This dissertation work developed a modified kinetic nucleation theory that incorporates cluster microphysical properties and temperature fluctuations into nucleation rate calculations. In this work, cluster temperature fluctuations are only caused by energy changes due to the interactions between clusters and monomers. Five modifications are applied to the kinetic nucleation theory originally developed by Becker and Döring (1935). These modifications are the use of aspherical cluster shapes, reduced cluster sticking coefficients, the reduction in the reliance on the capillarity approximation through the inclusion of cluster sublimation energies derived through DFT methods, cluster temperature fluctuations, and reduced monomer detachment rates associated with small clusters. The reliance on the capillarity approximation ultimately needed to be retained for two reasons: the scarcity of available binding and sublimation energy data for both water and carbon clusters, and the inability to determine clearly the size of the critical cluster when the available energy data is used. The modified theory is applied to the nucleation rates of water droplets and carbonaceous grains.

For water droplets, nucleation rate results are compared with those found using classical nucleation theory and observed in expansion cloud chamber experiments. The modified theory developed here finds nucleation rates a factor of 10^5 to 10^{13} larger than those found using classical nucleation theory, or the experimental rates observed by Wölk and Strey (2001). The high nucleation rates are associated with a reduced critical cluster size predicted by the modified theory. Such large discrepancies between theory and experiment have also been seen in the work of Lothe and Pound (1962), who sought to correct classical nucleation theory by correcting the work of cluster formation. They

found nucleation rates to be a factor of 10^{15} higher than observed in cloud chamber experiments (Feder et al., 1966). The nucleation rates observed in expansion cloud chamber experiments include only the number of droplets that have grown to sufficient size to be counted (Feder et al., 1966). As droplets grow and deplete the available monomers, the supersaturation level drops and the critical cluster size increases. This could cause a number of droplets to become unstable and evaporate completely, or just be too small to be counted in observation.

When applied to the formation of carbonaceous grains, similar discrepancies are found between the modified and classical nucleation theories. The modified theory predicts nucleation rates $\sim 10^{14}$ times larger than classical theory. Due to the lack of experimental results of carbon grain formation, theoretical rates could not be compared with experiment. Even with the large differences in nucleation rates, the formation of carbonaceous grains in the ejecta of a CCSN using the basic or unmodified kinetic nucleation theory does not result in large differences to the size and mass distributions, or total dust mass formed, when compared to the results using classical nucleation theory of Fallest et al. (2011). The nucleation process is predicted to begin sooner after the explosion, and thus at higher temperatures and lower supersaturation levels. Maximum nucleation rates for both kinetic and classical theories were within an order of magnitude of each other with the kinetic theories predicting an earlier condensation time. The greatest difference seen in the simulations was the due to the addition of available binding energy data for graphite clusters with $n \leq 55$ (Kosimov et al., 2008, 2010). Grains are predicted to form at lower temperatures and much higher supersaturation levels. The bulk of the grain formation occurs in a very short time and nucleation is quickly quenched afterwards due to monomer depletion. This leads to the formation of more smaller grains which are likely to be destroyed by the reverse shock before they can be injected into the ISM.

In applying the modified theory to carbonaceous grain formation in CCSN ejecta, nucleation rates are unable to be calculated within a reasonable amount of time. The nucleation process can occur at low supersaturation levels, however, the modified kinetic theory is not well-equipped to deal with such supersaturations. The fluctuations of the detachment rates above and below the attachment rate values cause finding the size of the critical cluster to be impossible, and therefore, nucleation rates calculated from these attachment and detachment rates are unreliable.

Besides the lack of reliable sublimation energy for small and intermediate cluster

sizes, other physical effects need to be taken into account before a fully modified kinetic theory of nucleation can be applied to astrophysical environments. In this work, we have neglected the role of radiation in altering the temperature of molecular clusters and grains. Dust formed in astrophysical environments absorb and reemit radiation and this process contributes to the cluster temperature fluctuations. Efficient cooling through photon emission will tend to stabilize the cluster to near ambient temperatures. The additional interactions involved with the inclusion of radiative processes will increase the number of code cycles needed in each simulation to achieve the desired number of detachment events. To address this issue, as well as the outstanding issue of the long times required to perform nucleation rate calculations for carbon clusters, the simulation code can be parallelized in order to take advantage of available large computing clusters.

References

G. W. Adams, J. L. Schmitt, and R. A. Zalabsky. The homogeneous nucleation of nonane. *The Journal of Chemical Physics*, 81(11):5074–5078, 1984. doi: 10.1063/1.447496.

M. P. Anisimov and S. N. Vershinin. Dibutylphtalate nucleation rate at carbon dioxide different pressures. *Journal of Aerosol Science*, 21, Supplement 1(0):S11 – S14, 1990. ISSN 0021-8502. doi: 10.1016/0021-8502(90)90177-Y. Proceedings of the 1990 European Aerosol Conference.

M. J. Barlow, O. Krause, B. M. Swinyard, B. Sibthorpe, M.-A. Besel, R. Wesson, R. J. Ivison, L. Dunne, W. K. Gear, H. L. Gomez, P. C. Hargrave, T. Henning, S. J. Leeks, T. L. Lim, G. Olofsson, and E. T. Polehampton. A Herschel PACS and SPIRE study of the dust content of the Cassiopeia A supernova remnant. *Astronomy and Astrophysics*, 518:L138, July 2010. doi: 10.1051/0004-6361/201014585.

J. C. Barrett, C. F. Clement, and I. J. Ford. Energy Fluctuations in Homogeneous Nucleation Theory for Aerosols. *Journal of Physics A: Mathematical and General*, 26 (3):529–548, FEB 7 1993. doi: 10.1088/0305-4470/26/3/016.

R. Becker and W. Döring. Kinetische Behandlung der Keimbildung in übersättigten Dämpfen. *Annalen der Physik*, 416:719–752, 1935. doi: 10.1002/andp.19354160806.

A. Beelen, P. Cox, D. J. Benford, C. D. Dowell, A. Kovács, F. Bertoldi, A. Omont, and C. L. Carilli. 350 μm Dust Emission from High-Redshift Quasars. *Astrophysical Journal*, 642:694–701, May 2006. doi: 10.1086/500636.

F. Bertoldi, C. L. Carilli, P. Cox, X. Fan, M. A. Strauss, A. Beelen, A. Omont, and R. Zylka. Dust emission from the most distant quasars. *Astronomy and Astrophysics*, 406:L55–L58, July 2003. doi: 10.1051/0004-6361:20030710.

S. Bianchi and R. Schneider. Dust formation and survival in supernova ejecta. *Monthly Notices of the Royal Astronomical Society*, 378:973–982, July 2007. doi: 10.1111/j.1365-2966.2007.11829.x.

R. Bowley and M. Sanchez. *Introductory Statistical Mechanics*. Oxford University Press, Oxford, 1999.

V. Bromm, P. S. Coppi, and R. B. Larson. The Formation of the First Stars. I. The Primordial Star-forming Cloud. *Astrophysical Journal*, 564:23–51, January 2002. doi: 10.1086/323947.

S. Brunier. The Milky Way at 5000 Meters, 2008. URL `http://apod.nasa.gov/apod/ap080104.html`. Date of publication: January 4, 2008. Date retrieved: June 3, 2012.

J. J. Burton. On the validity of homogeneous nucleation theory. *Acta Metallurgica*, 21 (9):1225 – 1232, 1973. ISSN 0001-6160. doi: 10.1016/0001-6160(73)90163-6.

E. Bussoletti and L. Colangeli. Cosmic dust: from space to laboratory. *Nuovo Cimento Rivista Serie*, 13:1–70, 1990. doi: 10.1007/BF02902933.

I. Cherchneff. Dust Formation in Massive Stars and Their Explosive Ends. In C. Leitherer, P. D. Bennett, P. W. Morris, and J. T. Van Loon, editors, *Hot and Cool: Bridging Gaps in Massive Star Evolution*, volume 425 of *Astronomical Society of the Pacific Conference Series*, June 2010.

I. Cherchneff and E. Dwek. The Chemistry of Population III Supernova Ejecta. I. Formation of Molecules in the Early Universe. *The Astrophysical Journal*, 703:642–661, September 2009. doi: 10.1088/0004-637X/703/1/642.

I. Cherchneff and E. Dwek. The Chemistry of Population III Supernova Ejecta. II. The Nucleation of Molecular Clusters as a Diagnostic for Dust in the Early Universe. *The Astrophysical Journal*, 713:1–24, April 2010. doi: 10.1088/0004-637X/713/1/1.

D. D. Clayton, W. Liu, and A. Dalgarno. Condensation of Carbon in Radioactive Supernova Gas. *Science*, 283:1290, February 1999. doi: 10.1126/science.283.5406.1290.

D. D. Clayton, E. A.-N. Deneault, and B. S. Meyer. Condensation of Carbon in Radioactive Supernova Gas. *The Astrophysical Journal*, 562:480–493, November 2001. doi: 10.1086/323467.

C. F. Clement and I. J. Ford. The Homogeneous Nucleation of Aerosols. *Journal of Aerosol Science*, 20(8):1015–1018, 1989. doi: 10.1016/0021-8502(89)90750-7.

I. J. Danziger. Dust and Supernovae. In G. Giobbi, A. Tornambe, G. Raimondo, M. Limongi, L. A. Antonelli, N. Menci, and E. Brocato, editors, *American Institute of Physics Conference Series*, volume 1111 of *American Institute of Physics Conference Series*, pages 351–361, May 2009. doi: 10.1063/1.3141572.

D. B. Dawson, E. J. Willson, P. G. Hill, and K. C. Russell. Nucleation of supersaturated vapors in nozzles. II. C_6H_6, $CHCl_3$, CCl_3F, and C_2H_5OH. *The Journal of Chemical Physics*, 51(12):5389–5397, 1969. doi: 10.1063/1.1671960.

E. A.-N. Deneault, D. D. Clayton, and B. S. Meyer. Growth of Carbon Grains in Supernova Ejecta. *The Astropysical Journal*, 638:234–240, February 2006. doi: 10.1086/498741.

A. Dillmann and G. E. A. Meier. A refined droplet approach to the problem of homogeneous nucleation from the vapor phase. *The Journal of Chemical Physics*, 94(5): 3872–3884, 1991. doi: 10.1063/1.460663.

B. Donn and J. A. Nuth. Does nucleation theory apply to the formation of refractory circumstellar grains? *Astrophysical Journal*, 288:187–190, January 1985. doi: 10.1086/162779.

J. Dorschner and T. Henning. Dust metamorphosis in the galaxy. *Astronomy and Astrophysics Reviews*, 6:271–333, 1995. doi: 10.1007/BF00873686.

T. Douvion, P. O. Lagage, and C. J. Cesarsky. Element mixing in the Cassiopeia A supernova. *Astronomy and Astrophysics*, 352:L111–L115, December 1999.

B. T. Draine. Interstellar Dust Grains. *Annual Review of Astronomy and Astrophysics*, 41:241–289, 2003. doi: 10.1146/annurev.astro.41.011802.094840.

B. T. Draine and E. E. Salpeter. Destruction mechanisms for interstellar dust. *The Astrophysical Journal*, 231:438–455, July 1979. doi: 10.1086/157206.

L. Dunne, S. Eales, R. Ivison, H. Morgan, and M. Edmunds. Type II supernovae as a significant source of interstellar dust. *Nature*, 424:285–287, July 2003. doi: 10.1038/nature01792.

L. Dunne, S. J. Maddox, R. J. Ivison, L. Rudnick, T. A. Delaney, B. C. Matthews, C. M. Crowe, H. L. Gomez, S. A. Eales, and S. Dye. Cassiopeia A: dust factory revealed via submillimetre polarimetry. *Monthly Notices of the Royal Astronomical Society*, 394: 1307–1316, April 2009. doi: 10.1111/j.1365-2966.2009.14453.x.

E. Dwek. The Evolution of the Elemental Abundances in the Gas and Dust Phases of the Galaxy. *Astrophysical Journal*, 501:643, July 1998. doi: 10.1086/305829.

E. Dwek and I. Cherchneff. The Origin of Dust in the Early Universe: Probing the Star Formation History of Galaxies by Their Dust Content. *Astrophysical Journal*, 727:63, February 2011. doi: 10.1088/0004-637X/727/2/63.

E. Dwek, F. Galliano, and A. P. Jones. The Evolution of Dust in the Early Universe with Applications to the Galaxy SDSS J1148+5251. *The Astrophysical Journal*, 662: 927–939, June 2007. doi: 10.1086/518430.

D. S. Eisenberg and W. Kauzmann. *The structure and properties of water*. Clarendon P., Oxford, 1969.

A. Elmhamdi, I. J. Danziger, N. Chugai, A. Pastorello, M. Turatto, E. Cappellaro, G. Altavilla, S. Benetti, F. Patat, and M. Salvo. Photometry and spectroscopy of the Type IIP SN 1999em from outburst to dust formation. *Monthly Notices of the Royal Astronomical Society*, 338:939–956, February 2003. doi: 10.1046/j.1365-8711.2003.06150.x.

M. Elvis, M. Marengo, and M. Karovska. Smoking Quasars: A New Source for Cosmic Dust. *The Astrophysical Journal*, 567:L107–L110, March 2002. doi: 10.1086/340006.

D. W. Fallest, T. Nozawa, K. Nomoto, H. Umeda, K. Maeda, T. Kozasa, and D. Lazzati. On the effects of microphysical grain properties on the yields of carbonaceous dust from Type II supernovae. *Monthly Notices of the Royal Astronomical Society*, 418: 571–582, November 2011. doi: 10.1111/j.1365-2966.2011.19506.x.

L. Farkas. Keimbildungsgeschwindigkeit in übersättigten Dämpfen. *Zeitschrift für Physikalische Chemie*, 125:236, 1927.

J. Feder, K. C. Russell, J. Lothe, and G. M. Pound. Homogeneous Nucleation and Growth of Droplets in Vapours. *Advances in Physics*, 15(57):111–178, 1966. ISSN 0001-8732. doi: 10.1080/00018736600101264.

J. Frenkel. A General Theory of Heterophase Fluctuations and Pretransition Phenomena. *The Journal of Chemical Physics*, 7(7):538–547, 1939. doi: 10.1063/1.1750484.

S. Fukusako. Thermophysical properties of ice, snow, and sea ice. *International Journal of Thermophysics*, 11:353–372, 1990. ISSN 0195-928X. 10.1007/BF01133567.

C. Gall, J. Hjorth, and A. C. Andersen. Production of dust by massive stars at high redshift. *Astronomy and Astropysics Review*, 19:43, September 2011. doi: 10.1007/s00159-011-0043-7.

S. L. Girshick and C. P. Chiu. Kinetic nucleation theory: A new expression for the rate of homogeneous nucleation from an ideal supersaturated vapor. *The Journal of Chemical Physics*, 93(2):1273–1277, 1990. doi: 10.1063/1.459191.

H. L. Gomez, C. J. R. Clark, T. Nozawa, O. Krause, E. L. Gomez, M. Matsuura, M. J. Barlow, M.-A. Besel, L. Dunne, W. K. Gear, P. Hargrave, T. Henning, R. J. Ivison, B. Sibthorpe, B. M. Swinyard, and R. Wesson. Dust in historical Galactic Type Ia supernova remnants with Herschel. *Monthly Notices of the Royal Astronomical Society*, 420:3557–3573, March 2012. doi: 10.1111/j.1365-2966.2011.20272.x.

P. Guhathakurta and B. T. Draine. Temperature fluctuations in interstellar grains. I - Computational method and sublimation of small grains. *The Astrophyiscal Jounral*, 345:230–244, October 1989. doi: 10.1086/167899.

J. Hartmann. Investigations on the spectrum and orbit of delta Orionis. *Astrophysical Journal*, 19:268–286, May 1904. doi: 10.1086/141112.

W. Herschel. O the Construction of the Heavens. *Royal Society of London Philosophical Transactions Series I*, 75:213–266, 1785.

F. Hoyle and N. C. Wickramasinghe. Dust in Supernova Explosions. *Nature*, 226:62–63, April 1970. doi: 10.1038/226062a0.

K Huang. *Statistical Mechanics*. Wiley, New York, second edition, 1987.

C. H. Hung, M. J. Krasnopoler, and J. L. Katz. Condensation of a supersaturated vapor. viii. the homogeneous nucleation of n-nonane. *The Journal of Chemical Physics*, 90 (3):1856–1865, 1989. doi: 10.1063/1.456027.

K. Iland, J. Wölk, R. Strey, and D. Kashchiev. Argon nucleation in a cryogenic nucleation pulse chamber. *The Journal of Chemical Physics*, 127(15):154506, 2007. doi: 10.1063/1.2764486.

R. O. Jones. Density functional study of carbon clusters C_{2n} ($2 \leq n \leq 16$). I. Structure and bonding in the neutral clusters. *Journal Of Chemical Physics*, 110(11):5189–5200, MAR 15 1999. ISSN 0021-9606. doi: 10.1063/1.478414.

V. I. Kalikmanov. Mean-field kinetic nucleation theory. *The Journal of Chemical Physics*, 124(12):124505, 2006. doi: 10.1063/1.2178812.

D. Kashchiev. *Nucleation: Basic Theory with Applications*. Butterworth-Heinemann, Oxford, 2000.

J. L. Katz, C. H. Hung, and M. Krasnopoler. The homogeneous nucleation of nonane. In P. E. Wagner and G. Vali, editors, *Atmospheric Aerosols and Nucleation*, 12th International Conference on Atmospheric Aerosols and Nucleation, pages 356–359, Aug 22-27, 1988.

A. C. Keith and D. Lazzati. Thermal fluctuations and nanoscale effects in the nucleation of carbonaceous dust grains. *Monthly Notices of the Royal Astronomical Society*, 410: 685–693, January 2011. doi: 10.1111/j.1365-2966.2010.17478.x.

D. P. Kosimov, A. A. Dzhurakhalov, and F. M. Peeters. Theoretical study of the stable states of small carbon clusters C_n ($n = 2 - 10$). *Phys. Rev. B*, 78:235433, Dec 2008. doi: 10.1103/PhysRevB.78.235433.

D. P. Kosimov, A. A. Dzhurakhalov, and F. M. Peeters. Carbon clusters: From ring structures to nanographene. *Phys. Rev. B*, 81:195414, May 2010. doi: 10.1103/PhysRevB.81.195414.

R. Kotak, W. P. S. Meikle, D. Farrah, C. L. Gerardy, R. J. Foley, S. D. Van Dyk, C. Fransson, P. Lundqvist, J. Sollerman, R. Fesen, A. V. Filippenko, S. Mattila, J. M. Silverman, A. C. Andersen, P. A. Höflich, M. Pozzo, and J. C. Wheeler. Dust and The Type II-Plateau Supernova 2004et. *The Astrophysical Journal*, 704:306–323, October 2009. doi: 10.1088/0004-637X/704/1/306.

T. Kozasa and H. Hasegawa. Grain Formation through Nucleation Process in Astrophysical Environments. II —Nucleation and Grain Growth Accompanied by Chemical Reaction—. *Progress of Theoretical Physics*, 77:1402–1410, June 1987. doi: 10.1143/PTP.77.1402.

T. Kozasa, H. Hasegawa, and K. Nomoto. Formation of dust grains in the ejecta of SN 1987A. *Astrophysical Journal*, 344:325–331, September 1989. doi: 10.1086/167801.

T. Kozasa, H. Hasegawa, and K. Nomoto. Formation of dust grains in the ejecta of SN 1987A. II. *Astronomy and Astrophysics*, 249:474–482, September 1991.

T. Kozasa, T. Nozawa, N. Tominaga, H. Umeda, K. Maeda, and K. Nomoto. Dust in Supernovae: Formation and Evolution. In T. Henning, E. Grün, and J. Steinacker, editors, *Cosmic Dust - Near and Far*, volume 414 of *Astronomical Society of the Pacific Conference Series*, page 43, December 2009.

O. Krause, S. M. Birkmann, G. H. Rieke, D. Lemke, U. Klaas, D. C. Hines, and K. D. Gordon. No cold dust within the supernova remnant Cassiopeia A. *Nature*, 432: 596–598, December 2004. doi: 10.1038/nature03110.

M. Kulmala. How particles nucleate and grow. *Science*, 302(5647):1000–1001, 2003. doi: 10.1126/science.1090848.

V. H. S. Kwong, D. Chen, and Z. Fang. Dissociative Charge Transfer between Ground-State HE^+ and CO at Electron-Volt Energies. *The Astrophysical Journal*, 536:954–958, June 2000. doi: 10.1086/308971.

D. G. Labetski, V. Holten, and M. E. H. van Dongen. Comment on "The nucleation behavior of supercooled water vapor in helium" [J. Chem. Phys. **117**, 5647 (2002)]. *The Journal of Chemical Physics*, 120(13):6314–6314, 2004. doi: 10.1063/1.1645770.

D. Lazzati. Non-local thermodynamic equilibrium dust nucleation in subsaturated vapours. *Monthly Notices of the Royal Astronomical Society*, 384:165–172, February 2008. doi: 10.1111/j.1365-2966.2007.12678.x.

H. R. Leider, O. H. Krikorian, and D. A. Young. Thermodynamic properties of carbon up to the critical point. *Carbon*, 11(5):555 – 563, 1973. ISSN 0008-6223. doi: 10.1016/0008-6223(73)90316-3.

E. W. Lemmon, M. O. McLinden, and D. G. Friend. Thermophysical properties of fluid systems. In P. J. Linstrom and W. G. Mallard, editors, *NIST Chemistry WebBook, NIST Standard Reference Database Number 69*, Gaithersburg MD, 20899, 2005. National Institute of Standards and Technology. URL `http://webbook.nist.gov`. Date retrieved: April 12, 2012.

L. Lenz and L. Ojamäe. A theoretical study of water equilibria: The cluster distribution versus temperature and pressure for $(H_2O)_n$, n = 1–60, and ice. *The Journal of Chemical Physics*, 131(13):134302, 2009. doi: 10.1063/1.3239474.

S. Lepp, A. Dalgarno, and R. McCray. Molecules in the ejecta of SN 1987A. *The Astrophysical Journal*, 358:262–265, July 1990. doi: 10.1086/168981.

A. Li and J. M. Greenberg. In dust we trust: an overview of observations and theories of interstellar dust. In V. Pirronello, J. Krelowski, and G. Manicò, editors, *Solid State Astrochemistry*, pages 37–84, 2003.

W. Liu, A. Dalgarno, and S. Lepp. Carbon monoxide in SN 1987A. *The Astrophysical Journal*, 396:679–685, September 1992. doi: 10.1086/171749.

J. Lothe and G. M. Pound. Reconsiderations of nucleation theory. *The Journal of Chemical Physics*, 36(8):2080–2085, 1962. doi: 10.1063/1.1732832.

L. B. Lucy, I. J. Danziger, C. Gouiffes, and P. Bouchet. Dust Condensation in the Ejecta of SN 1987 A. In G. Tenorio-Tagle, M. Moles, and J. Melnick, editors, *IAU Colloq. 120: Structure and Dynamics of the Interstellar Medium*, volume 350 of *Lecture Notes in Physics, Berlin Springer Verlag*, page 164, 1989. doi: 10.1007/BFb0114861.

R. Maiolino, R. Schneider, E. Oliva, S. Bianchi, A. Ferrara, F. Mannucci, M. Pedani, and M. Roca Sogorb. A supernova origin for dust in a high-redshift quasar. *Nature*, 431:533–535, September 2004. doi: 10.1038/nature02930.

A. Manka, D. Bergmann, D. Ghosh, J. Wölk, and R Strey. Preliminary results on homogeneous nucleation of water: a novel measurement technique using the two-valve expansion chamber. In C. D. O'Dowd and P. E. Wagner, editors, *Nucleation and Atmospheric Aerosols*, 17th International Conference on Nucleation and Atmospheric Aerosols, pages 260–264, Aug 13-17, 2007.

J. S. Mathis, W. Rumpl, and K. H. Nordsieck. The size distribution of interstellar grains. *The Astrophysical Journal*, 217:425–433, October 1977. doi: 10.1086/155591.

H. Matsubara, T. Koishi, T. Ebisuzaki, and K. Yasuoka. Extended study of molecular dynamics simulation of homogeneous vapor-liquid nucleation of water. *The Journal of Chemical Physics*, 127(21):214507, 2007. doi: 10.1063/1.2803899.

M. Matsuura, E. Dwek, M. Meixner, M. Otsuka, B. Babler, M. J. Barlow, J. Roman-Duval, C. Engelbracht, K. Sandstrom, M. Lakićević, J. T. van Loon, G. Sonneborn, G. C. Clayton, K. S. Long, P. Lundqvist, T. Nozawa, K. D. Gordon, S. Hony, P. Panuzzo, K. Okumura, K. A. Misselt, E. Montiel, and M. Sauvage. Herschel Detects a Massive Dust Reservoir in Supernova 1987A. *Science*, 333:1258–, September 2011. doi: 10.1126/science.1205983.

R. McGraw and R. A. LaViolette. Fluctuations, temperature, and detailed balance in classical nucleation theory. *The Journal of Chemical Physics*, 102(22):8983–8994, 1995. doi: 10.1063/1.468952.

W. P. S. Meikle, S. Mattila, A. Pastorello, C. L. Gerardy, R. Kotak, J. Sollerman, S. D. Van Dyk, D. Farrah, A. V. Filippenko, P. Höflich, P. Lundqvist, M. Pozzo, and J. C.

Wheeler. A Spitzer Space Telescope Study of SN 2003gd: Still No Direct Evidence that Core-Collapse Supernovae are Major Dust Factories. *The Astrophysical Journal*, 665:608–617, August 2007. doi: 10.1086/519733.

J. Merikanto, H. Vehkamäki, and E. Zapadinsky. Monte carlo simulations of critical cluster sizes and nucleation rates of water. *The Journal of Chemical Physics*, 121(2): 914–924, 2004. doi: 10.1063/1.1740754.

J. Merikanto, E. Zapadinsky, A. Lauri, and H. Vehkamäki. Origin of the failure of classical nucleation theory: Incorrect description of the smallest clusters. *Phys. Rev. Lett.*, 98:145702, Apr 2007. doi: 10.1103/PhysRevLett.98.145702.

R. C. Miller, R. J. Anderson, J. L. Kassner, and D. E. Hagen. Homogeneous nucleation rate measurements for water over a wide range of temperature and nucleation rate. *The Journal of Chemical Physics*, 78(6):3204–3211, 1983. doi: 10.1063/1.445236.

M. P. Moody and P. Attard. Curvature-dependent surface tension of a growing droplet. *Phys. Rev. Lett.*, 91:056104, Aug 2003. doi: 10.1103/PhysRevLett.91.056104.

H. L. Morgan and M. G. Edmunds. Dust formation in early galaxies. *Monthly Notices of the Royal Astronomical Society*, 343:427–442, August 2003. doi: 10.1046/j.1365-8711.2003.06681.x.

H. L. Morgan, L. Dunne, S. A. Eales, R. J. Ivison, and M. G. Edmunds. Cold Dust in Kepler's Supernova Remnant. *The Astrophysical Journal Letters*, 597:L33–L36, November 2003. doi: 10.1086/379639.

NASA, ESA, P. Challis, and R. Kirshner. A String of 'Cosmic Pearls' Surrounds an Exploding Star, 2007. URL `http://hubblesite.org/newscenter/archive/releases/2007/10/image/a/`. Date of publication: February 22, 2007. Date retrieved: June 3, 2012. Date last modified: November 3, 2009.

B. B. Nath, T. Laskar, and J. M. Shull. Dust Sputtering by Reverse Shocks in Supernova Remnants. *The Astrophysical Journal*, 682:1055–1064, August 2008. doi: 10.1086/589224.

K. Nomoto, N. Tominaga, H. Umeda, C. Kobayashi, and K. Maeda. Nucleosynthesis yields of core-collapse supernovae and hypernovae, and galactic chemical evolution. *Nuclear Physics A*, 777:424–458, October 2006. doi: 10.1016/j.nuclphysa.2006.05.008.

T. Nozawa, T. Kozasa, H. Umeda, K. Maeda, and K. Nomoto. Dust in the Early Universe: Dust Formation in the Ejecta of Population III Supernovae. *Astrophysical Journal*, 598: 785–803, December 2003. doi: 10.1086/379011.

T. Nozawa, T. Kozasa, A. Habe, E. Dwek, H. Umeda, N. Tominaga, K. Maeda, and K. Nomoto. Evolution of Dust in Primordial Supernova Remnants: Can Dust Grains Formed in the Ejecta Survive and Be Injected into the Early Interstellar Medium? *The Astrophysical Journal*, 666:955–966, September 2007. doi: 10.1086/520621.

T. Nozawa, T. Kozasa, N. Tominaga, I. Sakon, M. Tanaka, T. Suzuki, K. Nomoto, K. Maeda, H. Umeda, M. Limongi, and T. Onaka. Early Formation of Dust in the Ejecta of Type Ib SN 2006jc and Temperature and Mass of the Dust. *The Astrophysical Journal*, 684:1343–1350, September 2008. doi: 10.1086/589961.

T. Nozawa, T. Kozasa, N. Tominaga, K. Maeda, H. Umeda, K. Nomoto, and O. Krause. Formation and Evolution of Dust in Type IIb Supernovae with Application to the Cassiopeia A Supernova Remnant. *The Astrophysical Journal*, 713:356–373, April 2010. doi: 10.1088/0004-637X/713/1/356.

T. Nozawa, K. Maeda, T. Kozasa, M. Tanaka, K. Nomoto, and H. Umeda. Formation of Dust in the Ejecta of Type Ia Supernovae. *Astrophysical Journal*, 736:45, July 2011. doi: 10.1088/0004-637X/736/1/45.

D. W. Oxtoby. Nucleation of first-order phase transitions. *Accounts of Chemical Research*, 31(2):91–97, 1998. doi: 10.1021/ar9702278.

D. W. Oxtoby and R. Evans. Nonclassical nucleation theory for the gas–liquid transition. *The Journal of Chemical Physics*, 89(12):7521–7530, 1988. doi: 10.1063/1.455285.

S. J. Petuchowski, E. Dwek, J. E. Allen, Jr., and J. A. Nuth, III. CO formation in the metal-rich ejecta of SN 1987A. *The Astrophysical Journal*, 342:406–415, July 1989. doi: 10.1086/167601.

R. S. Priddey, K. G. Isaak, R. G. McMahon, E. I. Robson, and C. P. Pearson. Quasars as probes of the submillimetre cosmos at $z \geq 5$ - I. Preliminary SCUBA photometry. *Monthly Notices of the Royal Astronomical Society*, 344:L74–L78, October 2003. doi: 10.1046/j.1365-8711.2003.07076.x.

J. Rho, T. Kozasa, W. T. Reach, J. D. Smith, L. Rudnick, T. DeLaney, J. A. Ennis, H. Gomez, and A. Tappe. Freshly Formed Dust in the Cassiopeia A Supernova Remnant as Revealed by the Spitzer Space Telescope. *Astrophysical Journal*, 673:271–282, January 2008. doi: 10.1086/523835.

P. J. Robinson and K. A. Holbrook. *Unimolecular Reactions*. Wiley-Interscience, New York, 1972.

B. E. Rocher-Casterline, L. C. Ch'ng, A. K. Mollner, and H. Reisler. Communication: Determination of the bond dissociation energy (D_0) of the water dimer, $(H_2O)_2$, by velocity map imaging. *The Journal of Chemical Physics*, 134(21):211101, 2011. doi: 10.1063/1.3598339.

G. K. Schenter, S. M. Kathmann, and B. C. Garrett. Dynamical nucleation theory: A new molecular approach to vapor-liquid nucleation. *Phys. Rev. Lett.*, 82:3484–3487, Apr 1999a. doi: 10.1103/PhysRevLett.82.3484.

G. K. Schenter, S. M. Kathmann, and B. C. Garrett. Variational transition state theory of vapor phase nucleation. *The Journal of Chemical Physics*, 110(16):7951–7959, 1999b. doi: 10.1063/1.478727.

R. Schneider, K. Omukai, A. K. Inoue, and A. Ferrara. Fragmentation of star-forming clouds enriched with the first dust. *Monthly Notices of the Royal Astronomical Society*, 369:1437–1444, July 2006. doi: 10.1111/j.1365-2966.2006.10391.x.

B. Senger, P. Schaaf, D. S. Corti, R. Bowles, J. C. Voegel, and H. Reiss. A molecular theory of the homogeneous nucleation rate. i. formulation and fundamental issues. *The Journal of Chemical Physics*, 110(13):6421–6437, 1999. doi: 10.1063/1.478545.

A. Shank, Y. Wang, A. Kaledin, B. J. Braams, and J. M. Bowman. Accurate *ab initio* and "hybrid" potential energy surfaces, intramolecular vibrational energies, and classical ir spectrum of the water dimer. *The Journal of Chemical Physics*, 130(14):144314, 2009. doi: 10.1063/1.3112403.

M. A. Sharaf and R. A. Dobbins. A comparison of measured nucleation rates with the predictions of several theories of homogeneous nucleation. *The Journal of Chemical Physics*, 77(3):1517–1526, 1982. doi: 10.1063/1.443932.

B. Sibthorpe, P. A. R. Ade, J. J. Bock, E. L. Chapin, M. J. Devlin, S. Dicker, M. Griffin, J. O. Gundersen, M. Halpern, P. C. Hargrave, D. H. Hughes, W.-S. Jeong, H. Kaneda, J. Klein, B.-C. Koo, H.-G. Lee, G. Marsden, P. G. Martin, P. Mauskopf, D.-S. Moon, C. B. Netterfield, L. Olmi, E. Pascale, G. Patanchon, M. Rex, A. Roy, D. Scott, C. Semisch, M. D. P. Truch, C. Tucker, G. S. Tucker, M. P. Viero, and D. V. Wiebe. AKARI and BLAST Observations of the Cassiopeia A Supernova Remnant and Surrounding Interstellar Medium. *Astrophysical Journal*, 719:1553–1564, August 2010. doi: 10.1088/0004-637X/719/2/1553.

D. W. Silvia, B. D. Smith, and J. M. Shull. Numerical Simulations of Supernova Dust Destruction. I. Cloud-crushing and Post-processed Grain Sputtering. *The Astrophsyical Journal*, 715:1575–1590, June 2010. doi: 10.1088/0004-637X/715/2/1575.

S. Sinha, A. Bhabhe, H. Laksmono, J. Wölk, R. Strey, and B. Wyslouzil. Argon nucleation in a cryogenic supersonic nozzle. *The Journal of Chemical Physics*, 132(6): 064304, 2010. doi: 10.1063/1.3299273.

Z. Slanina, F. Uhlák, and J. F. Jean-Franois Crifo. A computational evaluation of the water-dimer populations in saturated steam recommended for applications to the

earth's, planetary and cometary atmospheres. *Journal of Molecular Structure*, 270(0): 1 – 9, 1992. ISSN 0022-2860. doi: 10.1016/0022-2860(92)85016-A.

M. D. Stage, et al., and NASA/CXC/MIT/UMass Amherst. Cassiopeia A, 2006. URL `http://chandra.harvard.edu/photo/2006/casa/`. Date of publication: November 15, 2006. Date retrieved: June 3, 2012. Date last modified: November 3, 2009.

K. Stowe. *Introduction to Statistical Mechanics and Thermodynamics*. Wiley, New York, 1984.

G. Stratta, R. Maiolino, F. Fiore, and V. D'Elia. Dust Properties at z = 6.3 in the Host Galaxy of GRB 050904. *The Astrophysical Journal*, 661:L9–L12, May 2007. doi: 10.1086/518502.

R. Strey, P. E. Wagner, and Y. Viisanen. The problem of measuring homogeneous nucleation rates and the molecular contents of nuclei: Progress in the form of nucleation pulse measurements. *The Journal of Physical Chemistry*, 98(32):7748–7758, 1994. doi: 10.1021/j100083a003.

B. E. K. Sugerman, B. Ercolano, M. J. Barlow, A. G. G. M. Tielens, G. C. Clayton, A. A. Zijlstra, M. Meixner, A. Speck, T. M. Gledhill, N. Panagia, M. Cohen, K. D. Gordon, M. Meyer, J. Fabbri, J. E. Bowey, D. L. Welch, M. W. Regan, and R. C. Kennicutt. Massive-Star Supernovae as Major Dust Factories. *Science*, 313:196–200, July 2006. doi: 10.1126/science.1128131.

R. G. Tabak, J. P. Hirth, G. Meyrick, and T. P. Roark. The nucleation and expulsion of carbon particles formed in stellar atmospheres. *The Atrophysical Journal*, 196:457–463, mar 1975. doi: 10.1086/153425.

T. Temim, P. Slane, S. P. Reynolds, J. C. Raymond, and K. J. Borkowski. Deep Chandra Observations of the Crab-like Pulsar Wind Nebula G54.1+0.3 and Spitzer Spectroscopy of the Associated Infrared Shell. *The Astrophysical Journal*, 710:309–324, February 2010. doi: 10.1088/0004-637X/710/1/309.

Thorlabs.com. Thorlabs.com – HeNe lasers: Green and Yellow. URL `http://www.thorlabs.com/NewGroupPage9.cfm?ObjectGroup_ID=1306`. Date retrieved: July 10, 2012. Date last modified: June 29, 2012.

A. G. G. M. Tielens. *The Physics and Chemistry of the Interstellar Medium*. Cambridge University Press, 2005.

P. Todini and A. Ferrara. Dust formation in primordial Type II supernovae. *Monthly Notices of the Royal Astronomical Society*, 325:726–736, August 2001. doi: 10.1046/j.1365-8711.2001.04486.x.

R. J. Trumpler. Absorption of Light in the Galactic System. *Publications of the ASP*, 42:214, August 1930. doi: 10.1086/124039.

H. Umeda and K. Nomoto. Nucleosynthesis of Zinc and Iron Peak Elements in Population III Type II Supernovae: Comparison with Abundances of Very Metal Poor Halo Stars. *The Astrophysical Journal*, 565:385–404, January 2002. doi: 10.1086/323946.

R. Valiante, R. Schneider, S. Bianchi, and A. C. Andersen. Stellar sources of dust in the high-redshift Universe. *Monthly Notices of the Royal Astronomical Society*, 397: 1661–1671, August 2009. doi: 10.1111/j.1365-2966.2009.15076.x.

E. F. van Dishoeck, G. A. Blake, B. T. Draine, and J. I. Lunine. The chemical evolution of protostellar and protoplanetary matter. In E. H. Levy and J. I. Lunine, editors, *Protostars and Planets III*, pages 163–241, 1993.

T. van Mourik and R. J. Gdanitz. A critical note on density functional theory studies on rare-gas dimers. *The Journal of Chemical Physics*, 116(22):9620–9623, 2002. doi: 10.1063/1.1476010.

H. Vehkamäki. *Classical Nucleation Theory in Multicomponent Systems*. Springer-Verlag, Berlin Heidelburg, 2006.

M. Volmer and A. Weber. Keimbildung in übersättigten Gebilden. *Zeitschrift für Physikalische Chemie*, 119:277, 1926.

P. E. Wagner. A constant-angle mie scattering method (CAMS) for investigation of particle formation processes. *Journal of Colloid and Interface Science*, 105(2):456 – 467, 1985. ISSN 0021-9797. doi: 10.1016/0021-9797(85)90319-4.

P. E. Wagner and R. R. Strey. Measurements of homogeneous nucleation rates for n-nonane vapor using a two-piston expansion chamber. *The Journal of Chemical Physics*, 80(10):5266–5275, 1984. doi: 10.1063/1.446554.

P. E. Wagner and R. Strey. Homogeneous nucleation rates of water vapor measured in a two-piston expansion chamber. *The Journal of Physical Chemistry*, 85(18):2694–2698, 1981. doi: 10.1021/j150618a026.

R. Wang, J. Wagg, C. L. Carilli, D. J. Benford, C. D. Dowell, F. Bertoldi, F. Walter, K. M. Menten, A. Omont, P. Cox, M. A. Strauss, X. Fan, and L. Jiang. SHARC-II 350 μm Observations of Thermal Emission from Warm Dust in $z \geq 5$ Quasars. *The Astronomical Journal*, 135:1201–1206, April 2008. doi: 10.1088/0004-6256/135/4/1201.

Y. Wang and J. M. Bowman. Communication: Rigorous calculation of dissociation energies (D_0) of the water trimer, $(H_2O)_3$ and $(D_2O)_3$. *The Journal of Chemical Physics*, 135(13):131101, 2011. doi: 10.1063/1.3647584.

J. Wölk and R. Strey. Homogeneous Nucleation of H_2O and D_2O in Comparison: The Isotope Effect. *The Journal of Physical Chemistry B*, 105(47):11683–11701, 2001. doi: 10.1021/jp0115805.

D. H. Wooden. Observational evidence for mixing and dust condensation in core-collapse supernovae. In T. J. Bernatowicz and E. Zinner, editors, *American Institute of Physics Conference Series*, volume 402 of *American Institute of Physics Conference Series*, pages 317–376, March 1997. doi: 10.1063/1.53315.

D. H. Wooden, D. M. Rank, J. D. Bregman, F. C. Witteborn, A. G. G. M. Tielens, M. Cohen, P. A. Pinto, and T. S. Axelrod. Airborne spectrophotometry of SN 1987A from 1.7 to 12.6 microns - Time history of the dust continuum and line emission. *Astrophysical Journal Supplement Series*, 88:477–507, October 1993. doi: 10.1086/191830.

P. A. Young, C. L. Fryer, A. Hungerford, D. Arnett, G. Rockefeller, F. X. Timmes, B. Voit, C. Meakin, and K. A. Eriksen. Constraints on the Progenitor of Cassiopeia A. *Astrophysical Journal*, 640:891–900, April 2006. doi: 10.1086/500108.

J. B. Zeldovich. On the theory of new phase formation, cavitation. *Acta Physicochimica URSS*, 18(1):1–22, 1943.

X. C. Zeng and D. W. Oxtoby. Gas–liquid nucleation in Lennard-Jones fluids. *The Journal of Chemical Physics*, 94(6):4472–4478, 1991. doi: 10.1063/1.460603.

D. I. Zhukhovitskii. The energy characteristics of the surface of small clusters. *Russian Journal of Phyiscal Chemistry*, 75(7):1043–1051, 2001. *Translated from Zhurnal Fizicheskoi Khimii, Vol. 75, No. 7, 2001, pp. 1159–1168. Translation by MAIK "Nauka/Interperiodica" (Russia).*

S. Zhukovska, H.-P. Gail, and M. Trieloff. Evolution of interstellar dust and stardust in the solar neighbourhood. *Astronomy and Astrophysics*, 479:453–480, February 2008. doi: 10.1051/0004-6361:20077789.